

APPROCHE MULTI-ÉCHELLE DE LA
FORMATION ET L'ÉVOLUTION DES AMAS
D'ÉTOILE

Julien Dorval

A thesis submitted for the degree of Doctor of
Philosophy

May 2014

Contents

Historical foreword: from Aristotle to GPU computing	1
1 Introduction	11
1.1 Introduction to star clusters	12
1.1.1 Why study them ?	12
1.1.2 Types of star clusters	13
1.2 Some important dynamical concepts	15
1.2.1 Virial theorem	15
1.2.2 Dynamical timescales	15
1.2.3 Static models	17
1.3 The origin of star clusters	18
1.3.1 From gas to stars	18
1.3.2 Substructure and early dynamical evolution	20
1.3.3 Star formation efficiency and infant mortality	20
1.4 Simulating star clusters evolution	22
1.4.1 Hydrodynamical simulations	22
1.4.2 Artificial substructure	23
1.5 Binary stars	25
1.5.1 What is a binary star ?	25
1.5.2 Why binaries ?	26
1.5.3 Multiplicity fraction	26
1.5.4 Observed population	27
1.5.5 Simulate binary populations in clusters	28
1.6 NBODY6	30
1.6.1 Hénon units	30
1.6.2 Block time-step	31
1.6.3 KS-regularization	32
1.6.4 Hermite integration scheme	32
1.6.5 Ahmad-Cohen neighbour scheme	35
2 The Hubble-Lemaître fragmented model: analytical approach	37
2.1 How to build a Hubble-Lemaître model	37
2.1.1 Initial state	37
2.1.2 Fragmentation	38
2.2 The growth of overdensities: analytical study	40
2.2.1 Working equations	40
2.2.2 Linear density perturbation	41
2.2.3 Consistent initial conditions	43
2.2.4 Segregation time-scale	44
2.2.5 Example with $N = 15000$	46

3 Nbody application	49
3.1 Approaching the N-body simulations	49
3.1.1 Presentation of the runs	49
3.1.2 Clump finding algorithm	49
3.2 Clump mass function	51
3.2.1 Influence of stellar mass function	51
3.2.2 Influence of H and N	53
3.3 Clump contents	54
3.3.1 The velocity field	54
3.3.2 The stellar mass function in clumps	56
3.3.3 Mass segregation	57
3.4 Concluding remarks	57
4 Collapse and dynamical evolution	63
4.1 The simulations	63
4.1.1 Description of the models	63
4.1.2 Scaling to physical units	64
4.1.3 Removal of the ejected stars	65
4.2 Collapse and virialisation	66
4.3 Global mass segregation	68
5 Detecting and injecting binaries	71
5.1 A new binary detection algorithm	71
5.1.1 Density comparison	71
5.1.2 Choosing a density ratio	72

Historical foreword: from Aristotle to GPU computing

Physics was not built in a day. In this foreword, I attempted a summary of the intellectual development that led us to our current state of knowledge. I did my best to honour the brilliant minds that made all of this possible. However, as everything in life, it should be taken with caution and a critical mind. I learned a lot researching for this, I'm sure you will too if you decide to dig further.

Motion

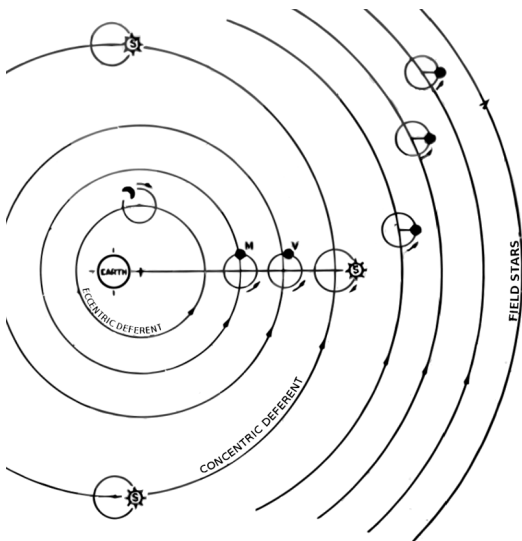
For two thousand years, Aristote physics dominated European philosophy. Rocks fell to the ground because they wanted to join their element, objects in the sky were attached to eternal rotating crystal spheres, and motion was either natural or violent, the latter needing a continuous force to exist. As the importance of projectiles grew in middle-age warfare, some improvement were made to explain trajectories, such as the impetus, a "contained source of motion" imprinted to a projectile by the thrower. Introduced by Philopon in the 6th century and relayed by Avicenne in the 11th century, it was properly formalized by Jean Buridan in the 14th century in his "Questions on Aristotle's Metaphysics". Buridan's impetus had a lot in common with momentum, in that it was proportionnal to mass and velocity. However, it could be circular, as shown by this description of celestial motion from Buridan ([Clagett, 1959](#)):

God, when He created the world, moved each of the celestial orbs as He pleased, and in moving them he impressed in them impetuses which moved them without his having to move them any more...And those impetuses which he impressed in the celestial bodies were not decreased or corrupted afterwards, because there was no inclination of the celestial bodies for other movements. Nor was there resistance which would be corruptive or repressive of that impetus.

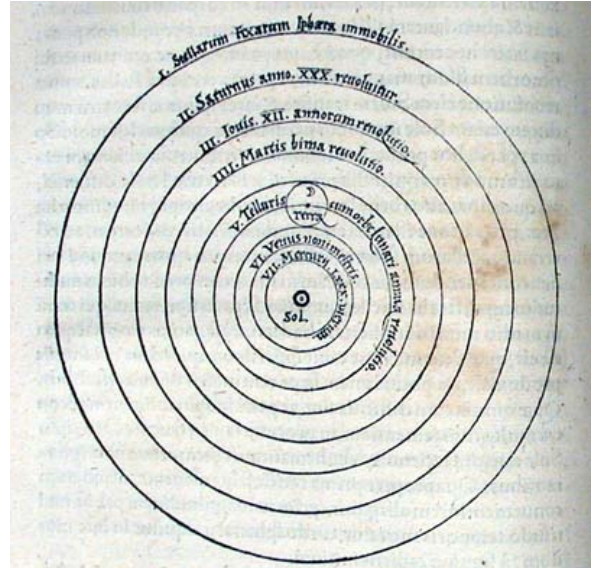
Despite the conceptual mistake of a circular momentum, Buridan, with this text, is the first to include the motion of celestial bodies in the same framework used for everyday, terrestrial motion. The impetus is not a good model, but it is a model for everything in the universe. No more eternal crystal spheres, everything in the universe must obey the same laws. Scientific revolutions do not happen in a vacuum: Buridan and others paved the way for the intellectual landslide of the 16th and 17th century.

Geocentrism and heliocentrism

While the concept of motion was slowly being refined, our vision of the universe was undergoing some faster changes. The dominant system in Europe since 150AD was the Ptolemaic geocentric model: the Sun and planets went around the Earth, following convoluted trajectories made of circles within circles called epicycles. Though complex, this system was consistent with Aristotle principles of celestial spheres and was accurate to a reasonable extent. Some alternate geocentric



(a) Ptolemy geocentric system



(b) Copernic heliocentric system

Figure 1: (a): depiction of the Ptolemaic geocentric system, the equant is not shown. (b): Copernicus illustration of his own heliocentric system, from *De revolutionibus*.

models were proposed by arab astronomers, such as Nasir ad-Din at-Tusi and Ibn al-Shatir, as well as rejected attempts to heliocentric models.

Nicolaus Copernicus studied astronomy in Cracow and Bologna, under the influence of harsh critics of the ptolemaic system. Strangely, this criticism was not fuelled by observations, but by astrology. Astronomy and astrology were closely intertwined, and the chaotic structure of the ptolemaic system made astrological considerations complicated (Barker et al., 2014). In a quest for consistency and simplicity, Copernicus proposed his heliocentric system, published in *De revolutionibus orbium coelestium* in 1543, the year of his death, in which all planets went around the sun, in the correct order. However, clinging to circular orbits, Copernicus had to preserve ptolemaic workarounds such as epicycles (not shown on Fig 1b).

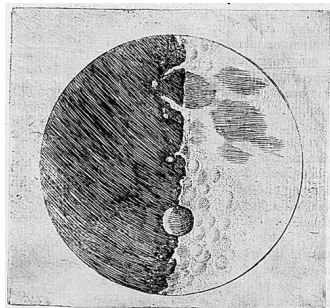
The astronomical evidence was, at the time, paradoxically against him. The apparent size changes of planets could not be measured yet, as well as stellar parallaxes, contradicting heliocentrism. The idea of a moving Earth implied some effect on falling bodies (known today as Coriolis effect) which were also not measurable at the time. Building on this apparent counter-evidence and on the work of indian astronomer Nilakantha Somayaji, Tycho Brahe, the most renowned astronomer of his time, proposed an alternative model known as the Tychonic system in the late 16th century (Ramasubramanian, 1998). Brahe maintained the Earth as the center of the universe, circled by the sun, itself orbited by all other planets. The system was very efficient and was quickly adopted by the Church and considered in compliance with the Holy Scriptures.

However, the seed of heliocentrism was planted in European scientific minds. The idea exalted the impetuous and visionary Giordano Bruno, who pushed the decentralization of Earth to the extreme, claiming stars were other suns, harbouring other planets, which themselves could sustain intelligent life. For this, his rejection of catholic dogma and his vehement refusal of retraction, Bruno was burned at the stake on the Campo de Fiori in 1600. Bruno, the fiery dialectist, despised geometry and believed the mind alone could unravel any mystery.

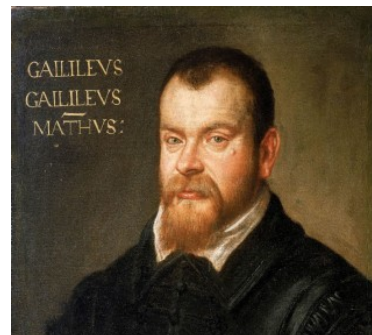
Johanes Kepler believed in geometry, in consistency and in observations. Ardent supporter of copernicism, he convinced Tycho Brahe to grant him access to his astronomical data, unsurpassed at the time. Focusing on the motion of Mars, Kepler, through trial and error, found out the planet was moving around the Sun following an ellipse. He formulated his first two laws of planetary motions. Further exploration led him to the third law. The three laws of Kepler of

20. Febr.	1610
marth. 12	O **
30. mone	** O *
2. xbn:	O *** *
3. mone	O * *
3. Ho. r.	* O *
4. mone	* O **

(a) Jupiter satellites



(b) Half-moon



(c) Galileo (1605)

Figure 2: (a) and (b): drawings by the hand of Galileo of his astronomical observations.

planetary motion were formulated, initiating the mathematisation of astronomy. They are:

Law I : All planets orbits are ellipses, with the Sun at one focus.

Law II: The line connecting a planet and the Sun sweeps out equal areas in equal amounts of times as the planet follow its orbit.

Law III: The squared orbital period of a planet is proportional to the cubed semi-major axis of its orbit.

The Starry Messenger

The father of modern astronomy, and precursor of modern science, Galileo Galilei was born in Pisa in 1564. For the first part of his scientific career, Galileo got famous for his lectures on mechanics and motion. Building on Buridan and Oresme's ideas, he expressed the mathematical form of free fall motion $d = \frac{gt^2}{2}$. Galileo also formulated what was essentially the future first law of motion from Newton.

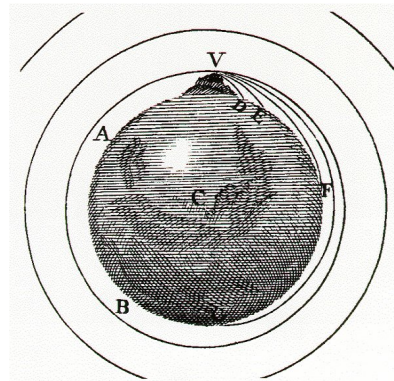
In 1609, his passion for scientific instruments led Galileo to build his own "dutch perspective glass", or telescope, a pioneering optical device from the Netherlands. Once pointed at the sky, the device triggered an avalanche of observations which would forever bury the aristotelian view of perfect and unchanged heavens. Moving Jupiter satellites, Moon craters and mountains, millions of stars in the Milky Way, these were consigned into *Sidereus Nuncius* (Starry messenger), the first scientific publication of astronomical observations ([Galileo, 1610](#)).

Strong advocate of copernicism, but lacking proper evidence, Galileo caused a large controversy with his *Dialogue Concerning the Two Chief World Systems* published in 1632, a pamphlet against the ptolemaic system, presenting (arguably unintentionally) one of its advocates as a simpleton. Despite his friendship with the pope, he had to retract his work and reject copernicism. Galileo spent the rest of his life under house arrest. Observational evidence at the time was still on the side of geocentrism. However, the extent of the backslash against Galileo showed the agitation of a Church having absorbed Ptolemy and Aristotle principles into its doctrine, in a time seeing the debate shift from theology to physics and observations.

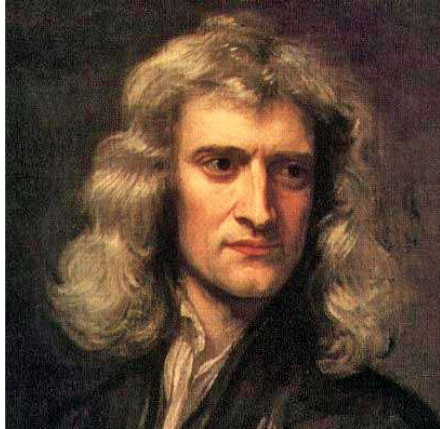
The relativity of motion is often attributed to Galileo, as he includes it in his controversial pamphlet, stating that a traveller inside a ship sailing smoothly would not be able to tell he's moving. Thus, people could be standing on a moving Earth without feeling it. However, this thought experiment was nothing new at the time and had been a recurring theme of mechanical philosophy since Buridan. Oresme, Copernicus and Bruno had been building on the idea, expanding and improving it, developing over the centuries an implicit understanding of inertia, until Bruno actually gives it a name: *virtù*. Galileo may have met Bruno himself, and had surely been influenced by his writings ([De Angelis & Santo, 2015](#)). Galileo's formulation was clearer,



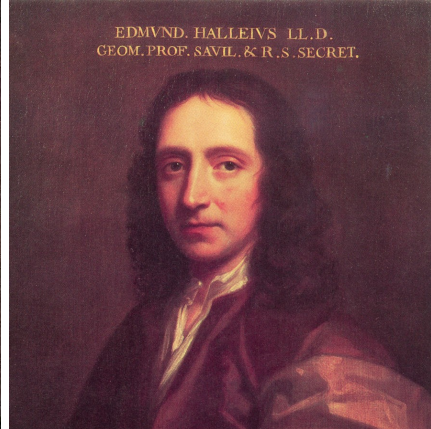
(a) "Not quite Newton's tree"



(b) Drawing from the *Principia*



(c) Isaac Newton (1689)



(d) Edmund Halley (1686)

Figure 3: (a) a supposedly descendant from Newton's apple tree in Cambridge. The drawing in (b) illustrates the common mechanics of cannonballs and satellites.

and part of a larger understanding of motion, introducing the concept of reference frame. After Copernicus decentralized the Earth, Galileo decentralized human subjectivity itself, setting the scene for the revolution to come.

On the shoulders of giants

Isaac Newton is without a doubt the father of modern mathematical science. Admitted in Cambridge in 1661, Newton supplemented the -still- official aristotelian teaching with more modern authors: Copernicus, Galileo, Kepler, and most of all, Descartes. The french philosopher had a profound impact on the young student, rooting his love for mathematics and deductive reasoning. However, while Descartes showed disdain for experimentation, Newton was an acute observer of the natural world.

In 1666, while in his mother's farm, having been forced out of Cambridge by the Plague, Newton began his reflection on the motion of celestial bodies. He derived from Kepler's law that the Sun had to exert an inverse squared distance attraction on the planets. Extending the concept to the Earth, moon, and a famous apple, Newton found a way to verify his hypothesis, using data from Galileo mechanical studies on the strength of Earth attraction. The wrong estimate of Earth radius he used at the time introduced a discrepancy which put the young man off his *gravitas* studies for 18 years.

Edmund Halley, astronomer and friend of Newton, having heard of Newton inverse squared law, urged him in 1684 to communicate his work to the Royal Society. With a new accurate measure of Earth radius and confronted to a concurrent claim to his law from Robert Hooke

(Kramer, 1982), Newton capitulated to Halley's eager enthusiasm and communicated his work in the famous *Philosophi Naturalis Principia Mathematica* (Newton, 1687). Published at Halley's own expense, the Principia shook all of Europe. Newton had invented Calculus (in parallel of Leibniz) and applied it to derive the universal law of Gravitation.

$$F = G \frac{m_1 \cdot m_2}{r^2} \quad (1)$$

Where:

- F Gravitational attraction between object 1 and object 2
- G Gravitational constant, $6.67408 \cdot 10^{-11} m^3 kg^{-1} s^{-2}$ (Pavese, 2015)
- m_i Masses of object 1 and 2
- r Distance between object 1 and 2

Though Newton was part of continuous line of geniuses and innovative minds building from each others, as he puts it "If I have seen further it is by standing on the shoulders of giants" (Maury, 1992), his input was truly revolutionary. He made large advances in optics and mathematics, and created a consistent mathematical framework to compute motions, essentially founding modern science and sowing the seeds of the industrial revolution. This framework is summed up by Newton's three laws of motion (from recent translation Cohen I. B. 1999):

Law I : Every body persists in its state of being at rest or of moving uniformly straight forward, except insofar as it is compelled to change its state by force impressed.

Law II: The alteration of motion is ever proportional to the motive force impress'd; and is made in the direction of the right line in which that force is impress'd.

Law III: To every action there is always opposed an equal reaction: or the mutual actions of two bodies upon each other are always equal, and directed to contrary parts.

The second law can be mathematically formulated in more modern terms:

$$\sum \mathbf{F} = \frac{d\mathbf{p}}{dt} \quad (2)$$

Meaning the sum of all forces \mathbf{F} applied to an object is equal to the time derivative of its momentum $\mathbf{p} = m \cdot \mathbf{v}$.

The N=3 body problem

As the Enlightenment brought a scientific revolution in many fields, I will now limit the discussion to the development of celestial mechanics, while acknowledging input from other fields.

While the two-body problem had been solved by Newton and expanded by Bernoulli in 1710 (Barrow-Green, 1997), in the 18th century the three-body problem remained the object of much investigation and development. A general solution for the Earth-Moon-Sun system would have had applications on nautical astronomy and trans-continental navigation. Extended analytical work by d'Alembert, Clairaut, Euler and Lagrange led to the development of early families of approximate solutions or exact solutions to special cases.

From 1773 to 1793, Joseph-Louis Lagrange, helped by his invention of Lagrangian mechanics, would make a lot of advances on the three-body problem. He introduced the concept of potential and discovered libration points (later known as Lagrange points). In the same time, Pierre-Simon de Laplace proved the stability of the solar system using a newly developed perturbation theory. The solar system dynamics were being unraveled, with finely tuned perturbation computation, but the general three-body problem remained unsolved.



(a) Charles Messier (1770)



(b) Henri Poincaré (1887)

Figure 4: The observer and the theorist, a century apart.

In 1888, Henri Poincaré, a renowned mathematician, submitted an entry to a contest sponsored by the King of Sweden Oskar II. The goal was to determine a usable solution to the N-body problem, for any given N. While Poincaré does not submit a complete solution, he wins the contest by presenting an in-depth exploration of the phase-space of the restricted three-body problem, which would later give rise to Chaos theory, see [Yoccoz \(2010\)](#). Poincaré managed to prove that the three-body problem had no solution involving simple functions.

Contrary to popular belief, the three-body problem *has* a solution, it was derived by Karl F. Sundman in 1912 ([Sundman, 1912](#)). However, any attempt to obtain accurate trajectory predictions would face an enormous convergence time, making the solution unusable in practice ([Belorizky, 1930](#)).

It is interesting to note that Elis Strömgren performed by-hand calculation of a three-body system, see [Aarseth \(2003\)](#); [Strömgren \(1909\)](#), prefiguring the advent of numerical orbit computation.

The $N > 3$ body problem

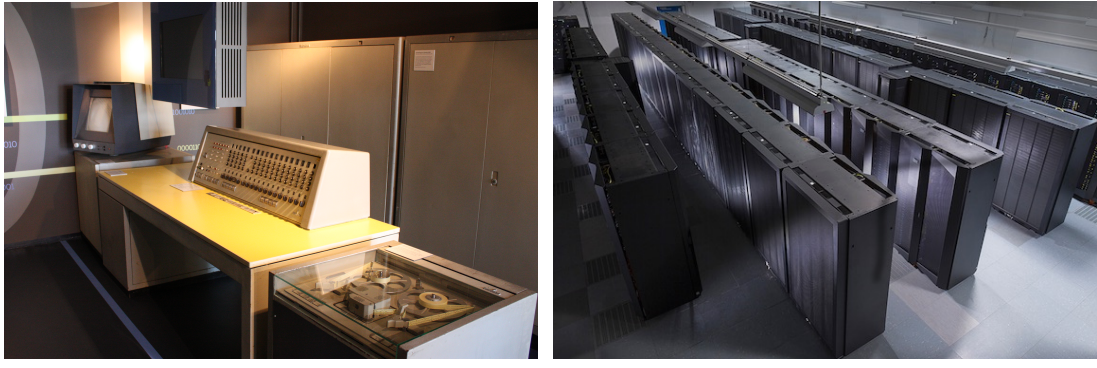
”The Sun attracts Jupiter and the other planets, Jupiter attracts its satellites and similarly the satellites act on one another.”

By this sentence from the *Principia*, Newton formulates the N-body gravitational problem, an arbitrary number of massive bodies all interacting gravitationally, for the solar system. The “ $N > 3$ -body” problem didn’t receive a lot of attention at first, as the unruly three-body problem was on everyone’s mind, and a higher-N problem seemed abstract, the solar system example being appropriately dealt in approximations.

In 1764, Charles Messier resolved individual stars in Messier 4, a globular cluster, hundreds of thousands of stars grouped together. Many new clusters were to be found afterwards, extending the catalog of real-life N-body systems. However, nothing was known of their kinematics, the stars were, in a sense, suspended motionless in the sky. This was the case until the advent of Doppler spectroscopy, which allowed astronomer to measure stars velocities ([Doppler, 1842](#)). Stellar dynamics had begun.

The $N > 3$ -body problem was still inaccessible, so scientists like James Jeans and Arthur Eddington decided to take the problem from the other hand, and took advantage of the large number of stars. Inspired by [Poincaré \(1906\)](#), both astronomers applied the statistical theory of gas to stellar systems, founding the field of stellar dynamics ([Jeans, 1916](#); [Eddington, 1916](#)).

An interesting experiment was conducted by [Holmberg \(1941\)](#) to understand the collision of two stellar systems (galaxies). With too few points to warrant a statistical approach, and before



(a) Siemens 2002

(b) Hydra supercomputer

Figure 5: The Siemens 2002, seen here on (a) at the computer museum in Kiel, could perform 2000 operations a second. The Hydra cluster, on (b), at the Max Planck Computing & Data Facility in Garching is made of 83,000 cores and 676 GPUs for a total of 10^{15} operations per seconds, a billion millions.

the rise of numerical integration, Holmberg modelled two galaxies with dozens of lightbulbs and photocells, measuring the attractive force with the amount of light received in each direction, taking advantage of the inverse squared fall of luminosity with distance, akin to gravity.

The numerical age

The first numerical N-body computations were performed by Sebastian Von Hoerner in 1959 when visiting the University of Tübingen, on a Siemens 2002, a cutting edge calculator at the time (Fig 5a). The very first had $N=4$. Then, Von Hoerner, back in Heidelberg, worked his way up to 16 stars, then 25, programming and debugging on punch cards. This story was told by Von Hoerner himself in [von Hoerner \(2001\)](#). He very quickly realized the importance of binary stars and their impact on computations. He was also able to confirm some theoretical prediction on cluster dynamics, and found a cuspy radial density profile([von Hoerner, 1960, 1963](#)).

There were two ways to increase the number of stars in simulations: buy a better computer or improve the algorithm. Sverre Johannes Aarseth got invested in the second path, which would take over his scientific life. Aarseth pioneered the use of individual time-step, changing the rate of particle positions update, gravitational softening (allowing convergence for close approaches), and polynomial predictions for force calculations ([Aarseth & Hoyle, 1964](#)). As power and optimization grew, investigations expanded, such as the interaction star-gas ([van Albada, 1968b](#)) and binary formation ([van Albada, 1968a](#)).

The 1970s brought two new important optimisation methods: KS regularization of close pairs ([Aarseth, 1972](#)) or 3-body systems ([Aarseth & Zare, 1974](#)) and Ahmad-Cohen neighbour scheme ([Ahmad & Cohen, 1973](#)). The number of stars in simulations kept growing, reaching 1000 with [Terlevich \(1980\)](#) and materializing into the *NBODY5* integrator. At this point various methods departing from a pure collisional calculation began to emerge, such as the simplified distant interaction with the [Barnes & Hut \(1986\)](#) tree algorithm.

To go beyond the regular improvement of computing power with time, a group of Japanese researchers, among whom Junichiro Makino, designed and built special purpose hardware for many-body problems: GRAPE ([Ebisuzaki et al., 1990; Ito et al., 1991](#)). These cards vastly improved the speed of N-body simulations and were a milestone on the road to the parallelization of computing. With the force calculation directly implemented in the hardware, GRAPE dominated the field for 15 years.

The latest technological leap in N-body simulations came from graphic cards, see [Bédorf & Portegies Zwart \(2012\)](#) for a more detailed historical perspective. Graphical Processing Units, or

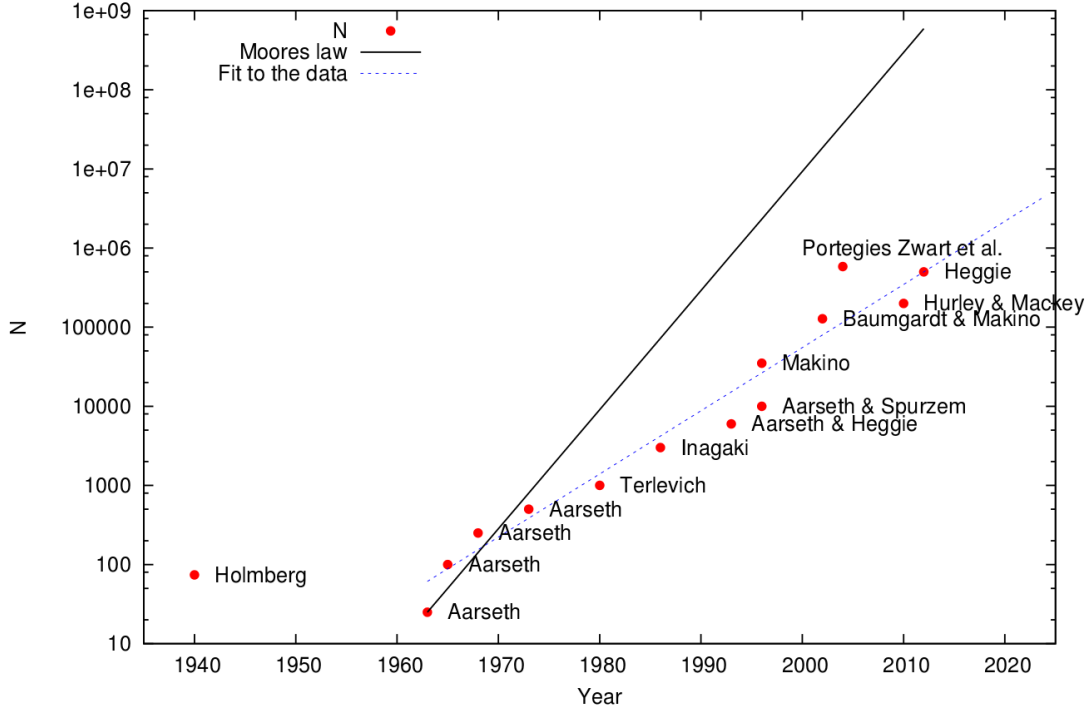


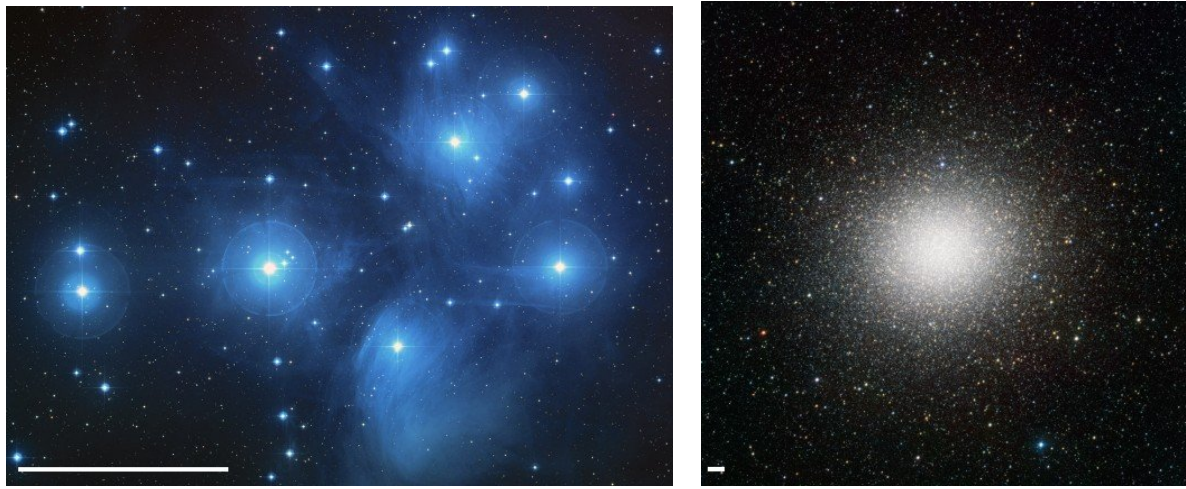
Figure 6: The evolution of the number of particles in N-body simulations. Solid line shows the Moore law. The figure was taken from [Bédorf & Portegies Zwart \(2012\)](#).

GPU, were originally designed for computer games visual rendering, applying the same transformations to a lot of pixels at the same time. These made them very efficient parallel computing machines for physics. Interest in GPU computing started to grow in the 2000s ([Nyland, Harris & Prins, 2004](#); [Elsen et al., 2006](#); [Portegies Zwart, Belleman & Geldof, 2007](#)) until the advent of usable GPU programming languages, like CUDA, in the late 2000s. At this point GPU were more efficient than GRAPE hardware for force calculation. Keigo Nitadori and Sverre Aarseth developed a GPU-accelerated version of NBODY6 in 2012 ([Nitadori & Aarseth, 2012](#)). A new iteration of the NBODY family, NBODY7, was also developed to include post-newtonian effects from General Relativity ([Aarseth, 2012](#)).

This year, 330 years after the publication of the *Principia*, [Wang et al. \(2016\)](#) performed several collisional nbody simulations of one million stars with a modified version of NBODY6 running on GPUs, on the Hydra supercomputer (Fig 5b). Computers have made it possible for humans to study systems of incredible scales in space and time, only using the universal law of gravitation. N-body numerical integrators are the culmination of centuries of scientific development on the motion of massive bodies.

CHAPTER 1

Introduction



(a) The Pleiades, open cluster

(b) ω Centauri, globular cluster

Figure 1.1: Examples of various types of cluster. White bars at the lower left of each pictures show 1 parsec length scale. The dust present in the young Pleiades open cluster scatters starlight, producing this blue haze. The globular cluster ω Centauri contains one million stars and is the largest known star cluster in the Milky Way.

Credits: NASA, ESA, AURA/Caltech; ESO/INAF-VST/OmegaCAM

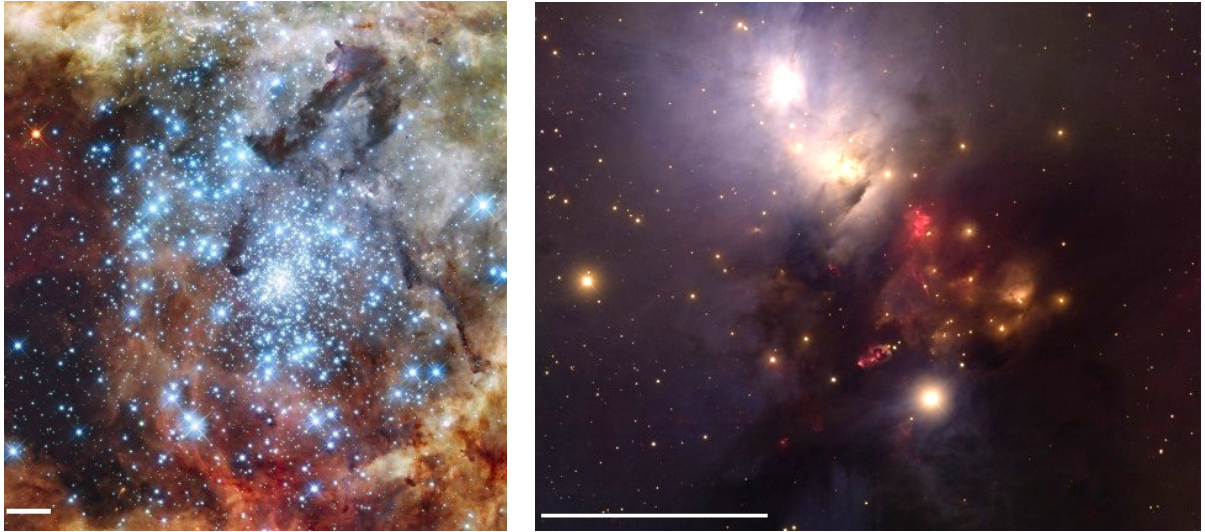
1.1 Introduction to star clusters

What is a star cluster ? A direct, almost tautological, definition is "a group of stars". However, this includes galaxies and random line-of-sight groups. We are interested in physical objects, smaller than galaxies, in which stars are, if not bound together, at least under direct mutual gravitational influence. Such objects include open clusters, globular clusters or associations. [Lada & Lada \(2003\)](#) adopted the following definition: a cluster is a stellar system with $N > 35$ and a density $\rho > 1 \text{ M}_\odot/\text{pc}^3$. These objects can either dissolve in less than a million year or remain bound for billions of years. In the last century, thanks to the improvement of observational technology, many clusters have been discovered and their origins are progressively being unravelled.

1.1.1 Why study them ?

Clusters are the result of bursts of star formation in giant molecular clouds, or GMCs. All stars within a cluster were born approximately at the same time, which explains the sustained interest of the scientific community for star clusters: they are the best available stellar physics laboratories, a large population of stars sharing the same age and distance to Earth. The age of the cluster can be derived from the most massive surviving stars in the population, as stars have lifetimes inversely correlated with their mass. Overall, integrated spectral features from all members of a star cluster can provide a wealth of information.

As we will see, clusters are also crucial to understand stellar formation. They harbour the most massive and young stars, which cause large-scale ionisation, winds and shockwaves from their explosive death in supernovae. Massive stars caused the re-ionization of the entire observable Universe 400 Myr after the Big Bang. To understand massive stars is to understand star formation, and to understand star formation is to understand star clusters.



(a) R136, Young Massive Cluster

(b) NGC 1333, embedded cluster

Figure 1.2: Examples of various types of cluster. White bars show 1pc. The young massive cluster R136 is surrounded by its primordial nebula while the embedded cluster NGC 1333 is still inside it. (b) is a composite of visible and infra-red light. *Credits: NASA, ESA, F. Paresce; T. Rector(U.Alaska Anchorage), H. Schweiker*

1.1.2 Types of star clusters

Star clusters are historically divided into two main categories: globular clusters and open clusters. As observational technology improved, categories tended to blend into a spectrum of size, age, and dynamical state, with Young Massive Clusters, embedded clusters and OB associations. Several of these categories have significant overlap, but each one emphasizes a particular characteristic of star cluster, thus these are useful for a comprehensive discussion.

Globular clusters are old and massive stellar systems. Most of them are older than 10 Gyr and more massive than $10^4 M_{\odot}$. The most massive known Globular cluster in the Milky Way is ω Centauri, with $4 \cdot 10^6 M_{\odot}$ ([D'Souza & Rix, 2013](#)), see Fig 1.1b. They only contain stars, without any dust or gas. The 150 known globular clusters in the Milky way are scattered in the disk and the halo, with a higher concentration near the bulge ([Harris, 1996](#)).

Open Clusters are lighter objects, rarely more massive than $10^3 M_{\odot}$. They are also younger, with ages ranging from a few Myr to a few Gyr ([Dias et al., 2002](#)). In fact, open clusters do not have a clear definition other than the implicit and historical property of "not being a globular cluster". Overall, they are faint, sometimes irregular and volatile objects. Their small mass and lower density make them vulnerable to tidal disruption from passing massive clouds on nearby orbits. The pleiades are a famous example, see Fig 1.1a

OB associations contain even less stars than open clusters, a few dozens in average. They get their name from the very massive luminous O and B type stars they contain, sometimes more massive than $50 M_{\odot}$. Such stars do not survive more than a few million years, OB association are thus young objects located in active star forming regions. They are often found near other associations, in a hierarchical structure. Their density is much lower than a typical cluster, about $0.1 M_{\odot} pc^{-3}$ ([Wright et al., 2014](#); [Garcia et al., 2010](#)), in fact most are unbound and dissolving objects.

Embedded clusters are the youngest star clusters in the sky. Most of the stars, protostars and cores are still inside their primordial cloud, dust obscuring their optical light. The

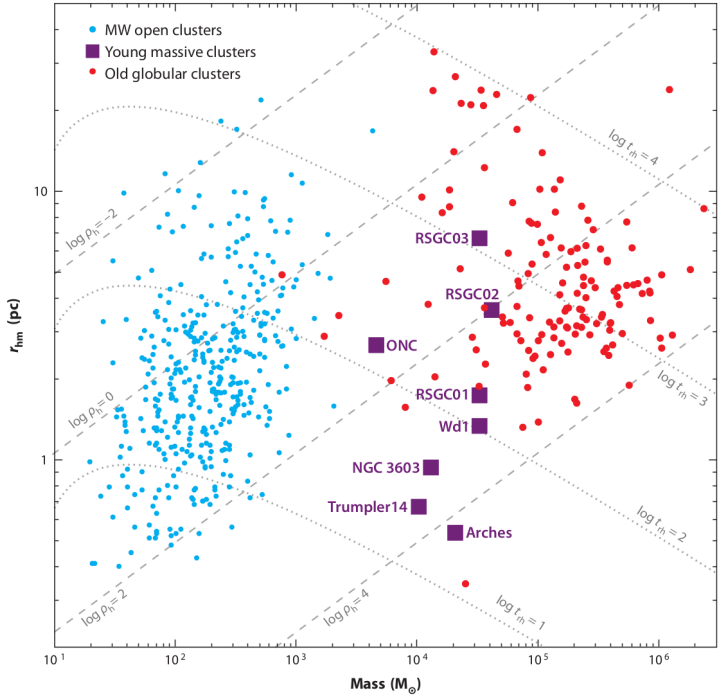


Figure 1.3: Radius-Mass Diagram for Milky Way clusters. Blue dots are open clusters, red dots Globular clusters and purple squares show Young Massive Clusters. Dashed lines show constant density within half-mass radius $\rho_h = 3M/8\pi r_{hm}^3$ and dotted lines show constant half-mass relaxation time. The plot was taken from the review [Portegies Zwart, McMillan & Gieles \(2010\)](#).

development of infrared astronomy unveiled the internal structure of these objects. As the gas is fully evacuated by 10 Myr ([Lada & Lada, 2003](#)), embedded clusters are younger and observed to be substructured ([Kuhn, Getman & Feigelson, 2015](#)). Some have ongoing star formation, like NGC 1333, a very young embedded cluster with both proto-stars and stars, see [Foster et al. \(2015\)](#) and Fig 1.2b.

Young Massive Clusters, or YMCs, are considered to be globular cluster progenitors. The review by [Portegies Zwart, McMillan & Gieles \(2010\)](#) provides a definition of YMCs: bound systems more massive than $10^4 M_\odot$ and younger than 100 Myr. Only a handful of such systems are known in the milky way (see Fig 1.3). The most studied YMC of the galactic neighborhood is R136, with a mass $\sim 10^5 M_\odot$ ([Andersen et al., 2009](#)), see Fig 1.2b. It is located in the Tarantula nebula, the most active known star forming region in the local group, inside in the Large Magellanic Cloud ¹. YMCs are found in large number in intense star forming environment such as starburst galaxies and galaxy mergers like the Antenna galaxies ([Whitmore et al., 2010](#)).

”All stars form in clusters” is a recurring statement in the field of stellar and cluster formation. Near Infra-Red (NIR) studies of star forming region yielded an star formation rate from embedded clusters of $\sim 3 \cdot 10^3 M_\odot \text{ Myr}^{-1} \text{ kpc}^2$ ([Lada & Lada, 2003](#)) while the same estimation for field stars in the milky way gives $\sim 3 - 7 \cdot 10^3 M_\odot \text{ Myr}^{-1} \text{ kpc}^2$ ([Miller & Scalo, 1979](#)). Another clue at the clustered nature of star formation is that high-mass O stars are for the vast majority, clustered, see [de Wit et al. \(2005\)](#). Due to their short life, O stars are often observed at the very location of their birth, or not very far. However, some work by, e.g, [Gutermuth et al. \(2011\)](#) shows a spatially hierarchical star formation. So stars do form in clusters, but these clusters

¹A dwarf irregular galaxy orbiting the milky way.

and subclusters are diverse and their dynamical evolution is complex. Properties of clusters are expected to vary depending on what we decide to call a cluster.

1.2 Some important dynamical concepts

1.2.1 Virial theorem

A self-gravitating system is a system bound by its own gravity. This applies to a star, a molecular cloud, a star cluster or a galaxy. In all cases, gravity is set against a counteracting source of energy that prevents the total collapse of matter into a single point. This source can be pressure for stars and clouds, but for stellar systems such as clusters and galaxies, it is the agitation of its components, the kinetic energy of the stars. Other energy sources include magnetic pressure or tidal fields.

The exchange between the gravitational potential energy and the internal energy follows the virial theorem, written in the general form (McKee & Ostriker, 2007; Binney & Tremaine, 2008):

$$\frac{1}{2} \frac{d^2 I}{dt^2} = 2(E_k - E_{k,s}) + E_p + E_{tides} + E_m \quad (1.1)$$

with I the moment of inertia, E_k the kinetic energy, E_p the potential energy. $E_{k,s}$ a thermal pressure surface term, E_{tides} the energy injected by a tidal field and E_m the magnetic pressure. For a stationary system, $\frac{1}{2} \frac{d^2 I}{dt^2} = 0$, and in a purely gravitational system with N particles, there is no thermal or magnetic pressure. Finally, if we consider an isolated system, $E_{tides} = 0$ and the virial theorem can be written in its more common form:

$$2E_k + E_p = 0 \quad (1.2)$$

with :

$$E_k = \sum_{i=1}^N m_i v_i^2 \quad \text{and} \quad E_p = - \sum_{i=1}^N \sum_{j>i}^N \frac{Gm_i m_j}{\|\mathbf{r}_i - \mathbf{r}_j\|}. \quad (1.3)$$

We define the virial parameter Q as:

$$Q = -\frac{E_k}{E_p}, \quad (1.4)$$

$Q = 0.5$ is a system in virial equilibrium. If the amplitude of the velocities is not sufficient to counteract the current value of potential energy, $Q < 0.5$, the system is said to be dynamically cold, or *subvirial*. While if the stars are too close together compared to their velocities, $Q > 0.5$, the system is hot and *survirial*. If $Q > 1$, the total energy is positive and the system is unbound.

1.2.2 Dynamical timescales

Dynamical systems tend to virial equilibrium. In such self-gravitating systems, it is useful to define a few dynamical time scales. The most simple one is the **crossing time**, defined as the time for a typical particle to cross the system. Following standard definitions (Meylan & Heggie, 1997; Fleck et al., 2006), it is expressed as

$$t_{cr} = \frac{2R_h}{\sigma} = \frac{2R_h}{\sqrt{GM/R_g}}, \quad (1.5)$$

where R_h is the half-mass radius, σ the three-dimensional velocity dispersion, M the mass of the system of gravitational radius R_g given by $GM/R_g = \sigma^2$.

Another crucial timescale in stellar dynamics is the **relaxation time**, which can be defined as (Heggie & Hut, 2003):

$$\frac{t_{rel}}{t_{cr}} = \frac{0.138}{2} \left(\frac{R_h}{R_g} \right)^{1/2} \frac{N}{\ln 0.4N} \quad (1.6)$$

In a self-gravitating system, stars have orbits. If N is large enough, the potential inside the system is smooth and stars have stationary orbits. The relaxation time is the timescale at which the impact of numerous encounters a star endures is comparable to the motion of its initial orbit. In other words, the initial conditions of a system are dynamically erased by collisional evolution after a relaxation time.

In a relaxed cluster, the core is dense with a high velocity dispersion, whereas the outskirts, the halo, is less dense and stars are slower. The definition from equation (1.5) and (1.6) imply the relaxation time changes with distance to the center. It is therefore useful to define a global timescale for the whole system, the **half-mass relaxation time** defined by Heggie & Hut (2003):

$$t_{rh} \simeq \frac{0.138}{\ln(0.4N)} \sqrt{\frac{N}{Gm}} R_h^{3/2} \quad (1.7)$$

with m the mass of a star and R_h the half-mass radius. Let us compute two examples, taking G in appropriate units:

$$G \simeq 4.48 \times 10^{-3} \text{ pc}^3 \text{ Myr}^{-2} \text{ M}_\odot^{-1}. \quad (1.8)$$

A cluster with 1000 stars of $0.5M_\odot$ and $R_h = 1$ pc has $t_{rh} = 13$ Myr, while a cluster with 10^6 stars of the same mass and a $R_h = 6$ pc has $t_{rh} = 3.1$ Gyr.

Equations (1.6) and (1.7) assume identical stellar masses in the system. In a real cluster, stars have different masses, differently affected by collisional evolution. The most massive stars cause gravitational focusing and exchange energy with other stars at a higher rate. They lose their energy to lighter stars, progressively sinking at the center. Heggie & Hut (2003) give an estimation of the segregation timescale $t_{ms}(m_1)$ of a mass m_1 :

$$t_{ms}(m_1) = \frac{m_1}{\langle m \rangle} t_{rh} \quad (1.9)$$

so a $30 M_\odot$ star in the previous 1000 star cluster will have a relaxation time of $\frac{0.5}{30} 13 = 0.21$ Myr = 210,000 years, much faster. A mass spread in a system speeds up considerably its collisional evolution.

A more general expression than (1.9) can be obtained to quantify the global segregation timescale. From Fleck et al. (2006), the mass-segregation timescale writes:

$$\frac{t_{ms}}{t_{rel}} \equiv \frac{\pi}{3} \frac{\langle m_\star \rangle}{\max\{m_\star\}} \frac{\bar{\rho}_h}{\rho_g} \left(\frac{R_h}{R_g} \right)^{3/2}, \quad (1.10)$$

where $\bar{\rho}_h = M/(4\pi/3)R_h^3$ is the mean density within radius R_h , and ρ_g the mean density inside a sphere of radius R_g .

1.2.3 Static models

It is useful to have a static reference model for a self-gravitating system at equilibrium. Considering a relaxed system with enough particles, one can use a statistical description to model its evolution, namely the "collisionless Boltzmann equation":

$$\frac{\partial f}{\partial t} + \mathbf{v} \cdot \nabla_r f - \nabla \Phi \cdot \nabla_v f = 0 \quad (1.11)$$

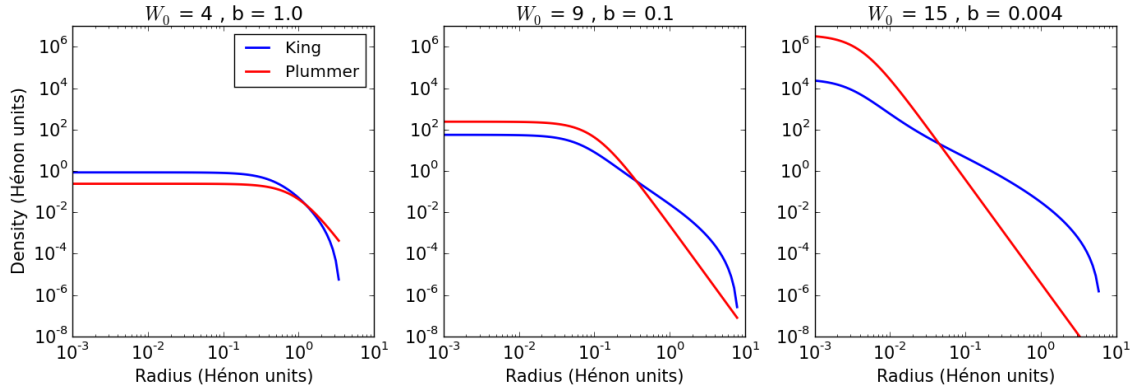


Figure 1.4: Comparison of King and Plummer models density as a function of radius, for similar core radii.

with $f(\mathbf{r}, \mathbf{v}, t)$ the phase space distribution and Φ the gravitational potential. There are several solutions to this equations, these are "static" models for star clusters as they are considered in equilibrium. Of course, the collisional equation can never be fully neglected and these models are approximations. We present here two models: Plummer and King. Both have a constant density in the center, the core, but they differ by their general behaviours.

The **Plummer model** is a simple model with a null potential at infinity. It is defined by its potential as a function of radius (Binney & Tremaine, 2008):

$$\Phi(r) = -\frac{GM}{\sqrt{r^2 + b^2}} \quad (1.12)$$

with b the Plummer parameter, setting the depth of the central potential and the core radius. From this expression, one can derive the radial density distribution:

$$\rho(r) = \frac{3M}{4\pi b^3} \left(1 + \frac{r^2}{b^2}\right)^{-\frac{5}{2}} \quad (1.13)$$

Equation (1.13) makes the computational generation of a cluster straightforward, which is why the Plummer model has been widely used in numerical simulations of star clusters. However, a Plummer model theoretically extends to infinity, and is not consistent with many globular cluster observations. Another, more complex, model has the observers on his side. The **King model** has been sucessfully used to fit light-profiles of globular clusters (King, 1981). It is defined as a distribution in energy:

$$f_k(E) = \begin{cases} f_0 \left(e^{-2j^2 E} - e^{-2j^2 E_0} \right), & \text{if } E < E_0. \\ 0, & \text{otherwise.} \end{cases} \quad (1.14)$$

with j a free parameter. The core radius can be tuned through a parameter $W_0 = 2j^2(E_0 - E_c)$ with E_c the rest energy at the center.

The main difference with the Plummer model can be seen in Fig 1.4: for a given core radius, King's density decreases slower than Plummer, but does falls to zero at a given radius contrary to Plummer that continues to infinity.

1.3 The origin of star clusters

1.3.1 From gas to stars

The interstellar medium, or ISM, is made of dust and gas in various phases, densities and temperatures, ranging from a hot ionized medium ($T > 10^5$ K and $n < 0.01$ cm $^{-3}$) to a cold neutral medium ($T < 100$ K and $n > 10$ cm $^{-3}$), see [Field, Goldsmith & Habing \(1969\)](#). Finally, in colder denser regions, $T \sim 10$ K and $n > 30$ cm $^{-3}$, the hydrogen takes molecular form H₂ in what is called molecular clouds. The dust contained in these regions makes them optically thick, obscuring background stars. These "holes in the sky", as William Herschel exclaimed upon the Dark Ophiucus Nebula([Houghton, 1942](#)), come in different sizes, from the Bok globules to Giant Molecular Clouds (GMCs). The interstellar dust absorbs the light in the visible and re-emits it in the infrared, thus the advent of infrared astronomy unveiled the interior of molecular clouds. In particular, recent observations with the Herschel Space Observatory showed a prevalence of filaments in clouds, see [André et al. \(2010\)](#) and Fig 1.5.

Star formation occurs in the higher density clumps or filaments inside the clouds. The origin of these overdensities has been the object of extensive theoretical development for 60 years. Turbulent motion was very early on designated as the main cause of overdensity. Turbulence is the transfer of energy from large scales to small scales, creating motions on small scales from a large energy driver. The well known Kolmogorov incompressible turbulence is hardly applicable to the ISM, as it is highly compressible ([Scalo et al., 1998](#)), instead, molecular clouds are subject to supersonic turbulence, or Burgers turbulence ([Frisch, Bec & Villone, 2001](#)). Nearby supernovas or tidal perturbation feed energy into the cloud, which is transferred through turbulence to smaller scales as supersonic internal motions, shocks forming overdense sheets. [McKee & Ostriker \(2007\)](#) argue that filaments originate both from the intersection of such sheets and the primordial morphology of the cloud, as self-gravitating pressureless matter condense as filaments ([Springel et al., 2005](#)).

Individual condensates of matter called cores form in clumps and filaments, these are stellar seeds (Fig 1.6a). To collapse, they have to overcome their magnetic and thermal pressure and their internal turbulence. The idealized picture of an hydrodynamical collapse relies on an estimation of the Jeans length λ_J , the maximum wavelength of a density perturbation in a uniform gas above which pressure cannot respond fast enough to avoid gravitational collapse. The corresponding Jeans mass M_J , of diameter λ_J is the minimum mass of a cloud to collapse. These quantities are derived in [Binney & Tremaine \(2008\)](#) and are expressed

$$\lambda_J = \sqrt{\frac{\pi}{G\rho}} c_s \quad (1.15)$$

$$\simeq 0.2 \text{pc} \left(\frac{c_s}{0.2 \text{ km.s}^{-1}} \right) \left(\frac{n}{10^3 \text{ cm}^3} \right)^{-\frac{1}{2}} \quad (1.16)$$

$$M_J = \frac{4\pi}{3} \rho \lambda_J^3 = \frac{\pi}{6} \frac{c_s^3}{G^{\frac{3}{2}} \rho^{\frac{1}{2}}} \quad (1.17)$$

$$\simeq 2.7 M_{\odot} \left(\frac{c_s}{0.2 \text{ km.s}^{-1}} \right)^3 \left(\frac{n}{10^3 \text{ cm}^{-3}} \right)^{-\frac{1}{2}} \quad (1.18)$$

with c_s , ρ and n the local sound speed, density and number density. These are the typical values expected for a prestellar core with such sound speeds and number densities. It is reasonable to assume the gas remain isothermal for the first part of the collapse, as the center radiates away the thermal energy from the increased density. When density reaches 10¹⁰ cm⁻³, the dust mixed in the protostellar material turns the core of the cloud optically thick, energy

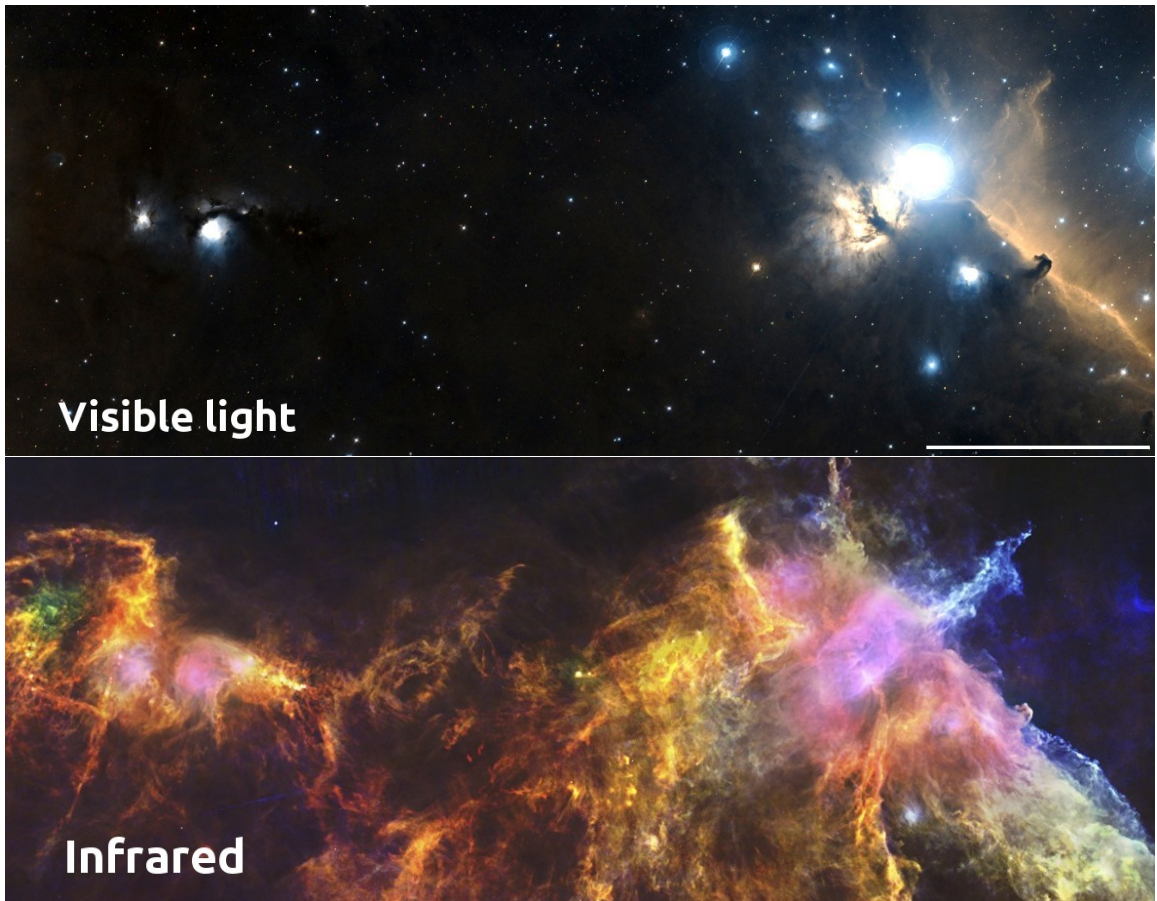


Figure 1.5: Visible light and infrared view of a part of the Orion star forming complex. Horshead nebula is visible on the right, as well as the very bright star Alnitak, part of the Orion belt. NGC 2071 and 2068 are visible on the left. Pink infrared coloring shows radiation from very bright young massive stars forming in the cloud. Colder filaments are visible all around. White bar on lower right of visible shows 1 parsec. *Credits: Digitized Sky Survey; ESA/Herschel/PACS.*

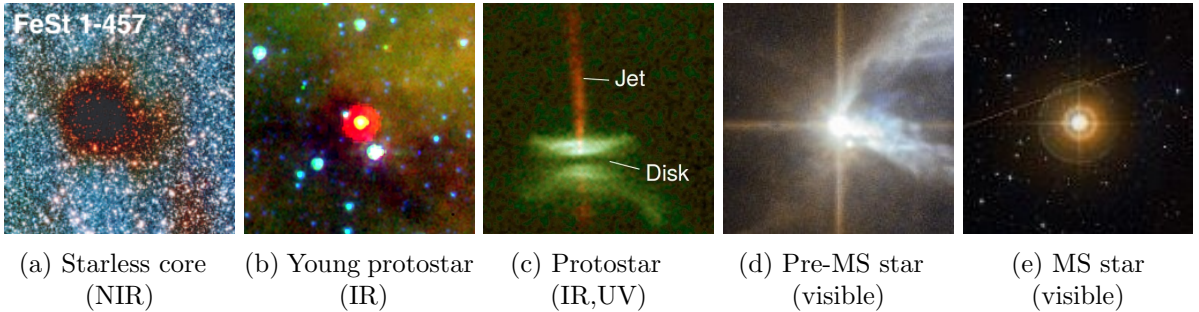


Figure 1.6: Stages of stellar birth. (a) is just cold molecular gas and contains no central source yet. (b) is more advanced, though hidden in visible light, its central protostar shines in infrared. The protostar in (c) is actively accreting its disk and produces jets. (d) is a pre main-sequence star, free from its envelope and surrounded by primordial gas. (e) is the mature stellar stage: the main sequence. *Credits: Kandori et al. (2005); NASA/JPL-Caltech/Evans,N; Burrows,C/HST-NASA; ESA/Hubble & NASA; DSS*

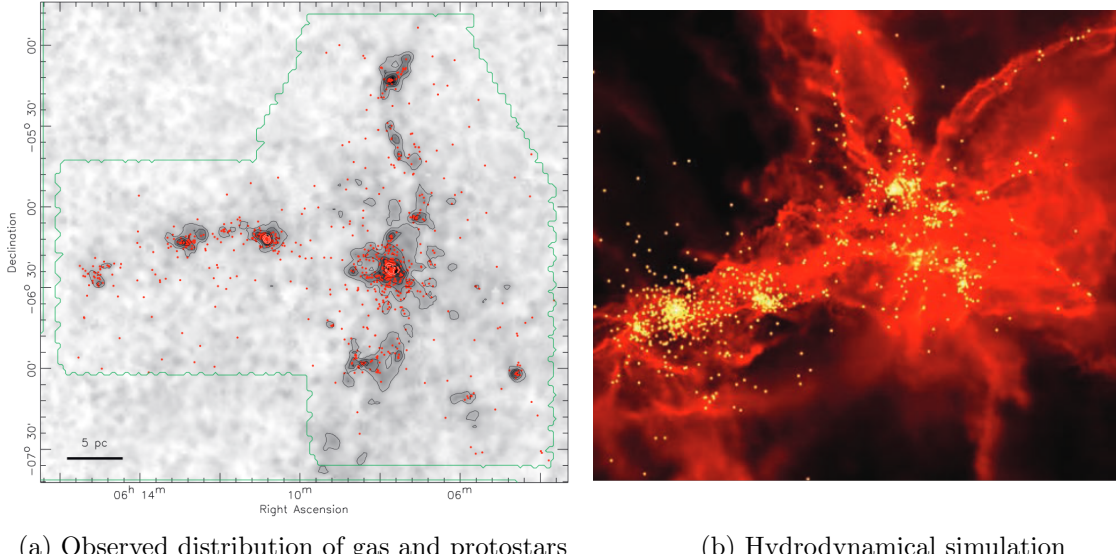
cannot be radiated away any more, temperature rises and collapse stops. Material continues to accumulate in the center, increasing the central density and temperature. When T reaches 2000K, molecular hydrogen starts to dissociate, absorbing energy. This allows a second collapse, stopped when all initial molecular hydrogen has been dissociated. The resulting core is called a protostar (Fig 1.6b), its density profile is peaked in the center and reaches about 10^{21} cm^{-3} and a temperature of 20,000K. The protostar has a mass of \sim a thousandth of its future stellar mass, as most of it is acquired through accretion of the envelope. Angular momentum from the original cloud shapes the gaseous envelope into a disk around the protostar, and magnetic activity starts creating jets (Fig 1.6c). This stage has been divided into several classes, based on the Spectral Energy Distributions (SED) emitted by the objects, as the emission shifts from far infrared to mid, then near-infrared as the envelope is accreted. See Evans et al. (2009) for an historical description of the SED classes and Larson (1969) for a theoretical overview of the principles of collapse and protostellar formation.

After about a Myr, accretion stops and the object becomes a Pre-Main Sequence (PMS) star (Fig 1.6d). It slowly contracts, following the Hayashi (1961) track. The source of energy of the star is still gravitational contraction, until central temperature reaches 10⁶K and hydrogen starts fusing into Helium. The object enters the Main Sequence and begin its life as a "proper" star (Fig 1.6e).

1.3.2 Substructure and early dynamical evolution

Observations show molecular clouds are substructured (see e.g. Cambrésy 1999). This substructure can be seen as a fractal distribution (Elmegreen & Falgarone, 1996) or a network of filaments (André et al., 2010), both consistent with compressible turbulence (McKee & Ostriker, 2007) . This hierarchical structure is inherited by the cores and protostars that emerges from the overdensities, as many observational studies of star forming regions shows (Schneider & Elmegreen, 1979; Hartmann, 2002; Bressert et al., 2010). Examples of substructured young clusters include the Taurus Ariga region, ρ -Ophiucus and Aquila, details and other examples can be found in both volumes of *The handbook of star forming region* Reipurth (2008).

However, other young clusters do not display such fractal, clumpy or filamentary structure. Instead, they are smooth, centrally condensed systems. The most known example is the Orion Nebula Cluster, or ONC. Located in the heart of the Orion complex, the largest and most active star forming region in the solar neighborhood, the age of the ONC is estimated to a few Myr. Hillenbrand & Hartmann (1998) found no clumps or filaments in the stellar distribution of the cluster, but a smooth distribution with a high density core formed by the Trapezium, a dense



(a) Observed distribution of gas and protostars

(b) Hydrodynamical simulation

Figure 1.7: (a): observational data from the Monoceros R2 star forming region. Protostars are shown as red points and gas density (traced through extinction) is shown in greyscale. The figure was extracted from [Gutermuth et al. \(2011\)](#). (b): hydrodynamical simulation of a star forming region yellow points are star-like sink particles and red levels show gas density. The figure was extracted from [Bonnell et al. \(2011\)](#).

system of massive stars. This mass segregation, if not fully primordial, implies that some amount of dynamical evolution took place in the ONC since the formation of the stars. This dynamical evolution could have erased the initial substructures.

These observations point at a rough picture of substructured stellar formation and early evolution: when the newly born stars emerges in clumps, if the background tidal field is weak and the star forming region sits well inside its Roche radius, the clumps then progressively merge and converge to the system barycentre to form a unique, relaxed self-bound association over a course of a few crossing time. This picture is backed up to some extent by hydrodynamical simulations of fragmentation modes in the turbulent ISM ([Klessen & Burkert, 2000](#); [Bate, Bonnell & Bromm, 2003](#); [Mac Low & Klessen, 2004](#); [Offner, Hansen & Krumholz, 2009](#); [Maschberger et al., 2010](#)) and by recent observational clues that subclusters show dynamical traces of mergers ([Kuhn et al., 2015](#)).

Figure 1.8 shows the similarity of stellar distribution obtained by observations and simulations of star forming regions.

1.3.3 Star formation efficiency and infant mortality

In their seminal paper on embedded clusters, [Lada & Lada \(2003\)](#) coined the term "infant mortality" for young star clusters. Comparing the populations of embedded clusters and older open clusters, the authors concluded clusters had a 90% mortality rate before 10 Myr. This is explained by the traditional picture of gas expulsion in clusters: a portion of the gas in a molecular clouds form a group of protostars, which quickly accrete their envelope, then start nuclear burning. This portion is expressed as the star formation efficiency:

$$\epsilon = \frac{M_*}{M_* + M_{gas}} \quad (1.19)$$

with M_{gas} the remaining gas after star formation. This gas is thought to be ejected from the young cluster through photo-ionization (the UV radiation from massive stars ionize the neutral

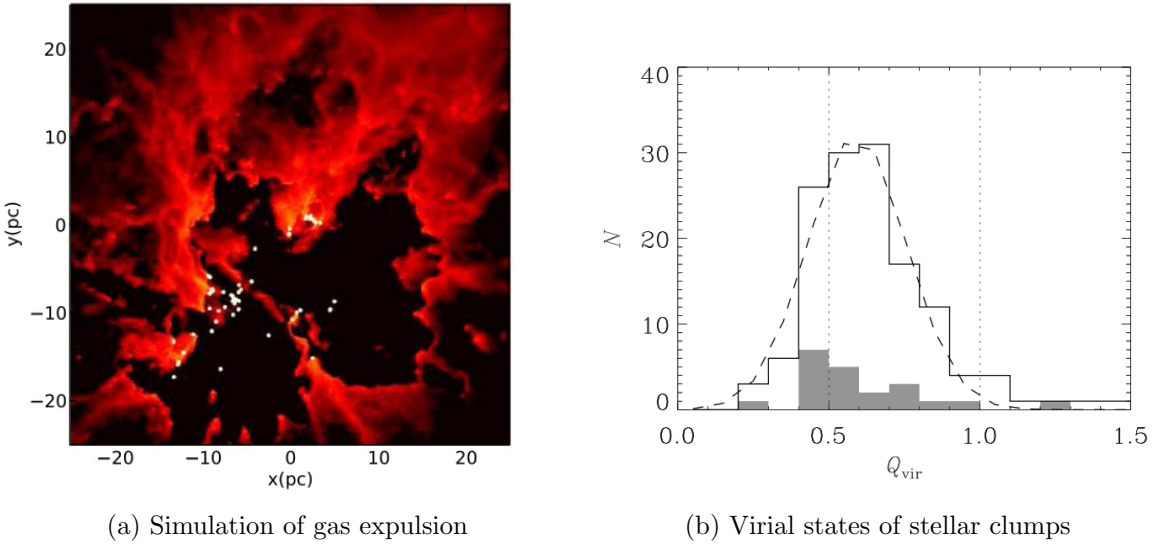


Figure 1.8: (a): hydrodynamical simulation of wind-induced gas expulsion around a small cluster, the figure was extracted from [Dale et al. \(2013\)](#). (b) virial parameter of stellar clumps in a star forming hydrodynamical simulation, ignoring the potential of the gas to predict their post-expulsion fate. The solid line is the cumulated distribution of clumps over all snapshots; the shaded histogram shows the final distribution. The figure was extracted from [Kruijssen et al. \(2012\)](#).

gas which heats up and expands), jets and outflows (young stars ejecting matter during accretion), winds (ejection of matter from stars surfaces at high speeds), and supernovae (shockwave from the explosive death of a massive star). The gas expulsion occurs on a crossing timescale, see [Krause et al. \(2016\)](#). Considering a young cluster in dynamical equilibrium, the loss of the mass of the gas on such a short timescale can unbound the system, as the stars velocities are now too high for the new potential well. The young cluster then dissolves following the gas expulsion. This picture is backed up by observations of young dissolving clusters ([Bastian & Goodwin, 2006](#)) consistent with corresponding numerical models ([Goodwin & Bastian, 2006](#)). Extensive analytical and numerical work have explored this process, e.g. [Tutukov \(1978\)](#); [Hills \(1980\)](#); [Lada, Margulis & Dearborn \(1984\)](#); [Adams \(2000\)](#); [Boily & Kroupa \(2003a,b\)](#), with an estimated minimum star formation efficiency of 30% to remain bound after gas expulsion.

However, the picture is more complicated than it seems. First, the efficiency of stellar feedback is a complex problem, winds, photonisation and supernovae have various impacts depending on the size and morphology of the clouds; they also seem to influence each other, for an overview of the problem see the serie of papers from [Dale & Bonnell \(2011\)](#); [Dale et al. \(2013\)](#) and references therein. Furthermore, recent hydrodynamical simulations such as [Pelupessy & Portegies Zwart \(2012\)](#) show the exact timescale of gas removal has a crucial importance on the fate of the cluster, with a slow removal allowing survival with ϵ as low as 5%.

Finally, most of the previously mentionned simulations assumed a relaxed embedded stellar system. However, as mentionned in previous section, star formation is substructured. Dynamical evolution between clumps and subclusters occurs on timescales comparable to gas expulsion, making the stellar spatial distribution of huge importance for survival, as shown by [Farias et al. \(2015\)](#). Hydrodynamical simulations (e.g [Kruijssen et al. 2012](#)) even point at subclusters being primordially bound and resistant to gas expulsion: Fig 1.8b show the distribution of virial parameter Q of stellar clumps in the simulation, ignoring the gas potential. The vast majority have $Q < 1$ and are expected to stay bound after expulsion. This is likely due to localized high ϵ . Though such observations are difficult, [Kuhn et al. \(2015\)](#) found many stellar subclusters to be bound after gas expulsion.

1.4 Simulating star clusters evolution

1.4.1 Hydrodynamical simulations

I invoked hydrodynamical simulations multiple times in the previous section. Let us look at them in more details. To model the formation of a star cluster from a core-less molecular cloud is no easy task. The model has to reproduce turbulence, core condensation, gravitational collapse, accretion, and for the most realistic ones, stellar feedback, magnetic effect and dust chemistry. Two numerical paths has been explored in the past: AMR and SPH.

Adaptative Mesh Refinement, AMR, is an Eulerian approach. The hydrodynamical equations (conservation of mass, momentum, the equation of state) are discretized and solved on a grid of cells following the finite volumes methods (see the RAMSES code, [Teyssier 2002](#)). Smoothed Particle Hydrodynamics, SPH, is a Lagrangian approach: instead of looking at inputs and outputs of matter in a cell, the gas is subdivided in particles free to move in the system. They are attributed a density, temperature and pressure. This method is akin the N-body integrator, and many SPH codes can work as purely gravitational integrators. SPH is popular in star formation simulations, as the problem is itself Lagrangian: grains of highly dense matter condensates and move around. Even if these codes can handle high density contrast, the collapse and formation of a protostar can still bring the numerical computation to a standstill. The usual workaround is the use of sink-particles: passed a given density threshold, several gas particles are merged into a single point-like object able to accrete any infalling matter. This works well though it suppresses any physical process below this accretion limit, usually a few to a hundred AU. ([Bate & Burkert, 1997](#)).

The precision, size and complexity of large scale cluster formation simulations have been steadily improving for 20 years (see [Turner et al. 1995](#); [Klessen & Burkert 2000](#); [Bate, Bonnell & Bromm 2003](#); [Offner, Hansen & Krumholz 2009](#); [Myers et al. 2014](#) and references). Nevertheless, no simulation to date include realistic cooling processes, radiative and wind feedback, magnetic fields and dust chemistry, all at the same time. All these are crucial to achieve precise and realistic simulation of the star formation process. Moreover, one of the most detailed star formation simulations to date, e.g [Bate \(2012\)](#), only form a few hundred stars and evolved them for less than 0.2 Myr with a simulation run time of several months.

However, good results are already being achieved, see the short review by [Clarke \(2012\)](#). Stellar properties and general structure agree with observations and interesting results are being obtained. [Maschberger & Clarke \(2011\)](#) and [Moeckel & Clarke \(2011\)](#) have noted that massive stars tend to sit at the heart of gas clumps in hydrodynamical simulations, some as the result of merger events with low-mass proto-stars.

In a nutshell, hydrodynamical simulations are not yet fully realistic, but they provide a good approximation of reality for small clusters and allow exploration or early dynamical processes.

1.4.2 Artificial substructure

There is a persistent difficulty to bridge over self-consistently from the star formation phase, to the equilibrium configuration of bound clusters. Hydrodynamical calculations of star forming regions evolve for up to a few 10^5 years, when a stable configuration would require several 10^6 years at typical cluster densities of 10^4 to 10^5 stars per cubic parsec. A way to overcome this issue is to switch to purely gravitational N-body simulations once the stars formed and most of the gas has been either accreted or expulsed. It is computationally less expensive and allows for longer integration of larger systems.

It is then essential to obtain a good model of the stars phase-space distribution at the end of a hydrodynamical simulation. While King and Plummer model have a known distribution one can sample from, no such thing exist for the clumps and filamentary structure of the newborn stellar objects in star-forming regions. Several methods have been explored to solve this.

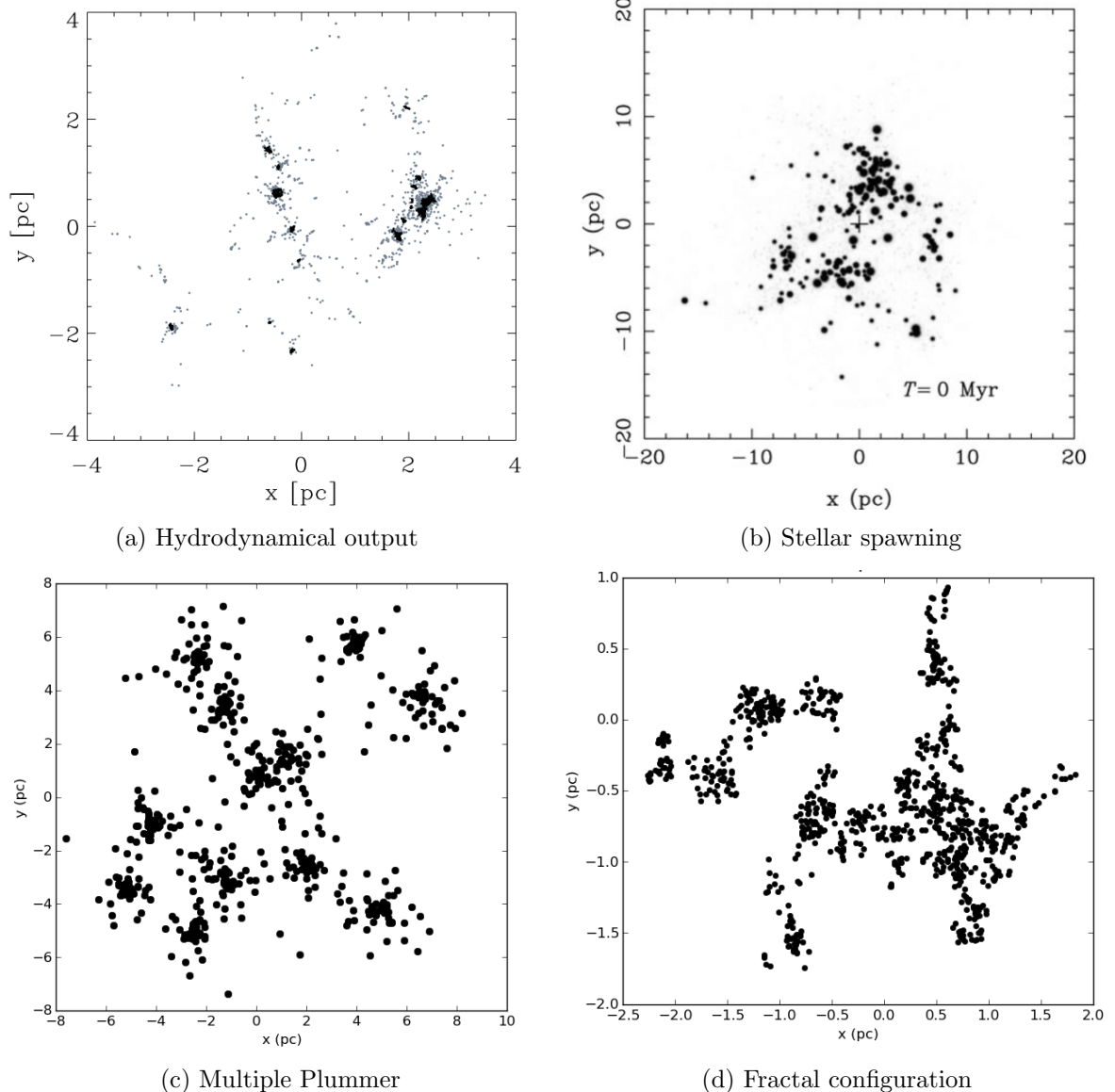


Figure 1.9: Representation of four methods to generate substructures. (a) is extracted from Kruijssen et al. (2012), constructed with data from Bonnell, Bate & Vine (2003), (b) is extracted from Fujii (2015). (c) and (d) were generated for this work.

Sink particle distribution is the most straightforward solution. [Moeckel & Bate \(2010\)](#) took the distribution of sink particles formed in the hydrodynamical simulation by [Bate \(2009\)](#) and directly converted it as a stellar distribution, preserving the masses, positions and velocities of the "stellar seeds". This is probably the best initial conditions for nbody simulations of young clusters that can be achieved, at the cost of speed, sampling and size. The initial hydrodynamical simulation took months to complete, making it hard to run it again and impossible to run it multiple times to obtain a good statistical sampling of the model. The size of the cluster achieved cannot exceed 1000 stars given the current state of hydrodynamical simulations.

Stellar spawning from hydrodynamics is a variant of the previous method. [Fujii & Portegies Zwart \(2016\)](#) started from hydrodynamical simulations of massive molecular clouds and stopped the integration once the main structures had formed but before local gravitational collapse had set in. Stars were then spawned in space following the distribution of gas. This enables larger clusters and quicker initial conditions of structures. However, the velocity distribution of these new stars is artificial, as it can at best inherit the gas velocity, without including the impact of the early collisional evolution that occurs between protostars in the clumps.

Scattered Plummer spheres is an analytic answer to the substructure problem. [McMillan, Vesperini & Portegies Zwart \(2007\)](#) created a clumpy model for a young star cluster by spawning several Plummer spheres randomly in space. This is almost immediate and is a good approximation. The authors obtained interesting results on the inheritance of mass segregation during mergers. However, clumps within a young star clusters have no reason to follow a Plummer profile, this places a constraint on the clumps internal dynamics which bias the dynamical evolution.

Fractal models were introduced by [Goodwin & Whitworth \(2004\)](#) and has been used in numerous studies ever since, e.g. [Allison et al. \(2009b\)](#); [Kouwenhoven et al. \(2010\)](#); [Parker & Wright \(2016\)](#). The idea is to grow a 3D pseudo-fractal tree with probabilistic branching, up to a given level, turning the final leaves into stars. The method is fast and the result is spatially realistic, fitting the observation that finds a fractal structure in the molecular clouds and star forming regions. However, the velocity distribution is artificial, drawn from successive gaussians at each levels. The clumps will relax when integration starts, shaking the whole system right off the bat.

It seems the generation of substructure has to balance realism and computational cost. The most realistic method is too costly, and most of the quicker alternatives are disconnected from the dynamical effect arising from the collisional effects young stars undergo inside a clumpy configuration.

1.5 Binary stars

1.5.1 What is a binary star ?

When two massive bodies of mass m_1 and m_2 interact gravitationally, they can have different types of trajectory depending on their total energy:

$$E = E_k + E_p = \frac{1}{2}m_1v_1^2 + \frac{1}{2}m_2v_2^2 - \frac{Gm_1m_2}{\|\mathbf{r}_1 - \mathbf{r}_2\|}. \quad (1.20)$$

If $E < 0$, they are bound and locked in a binary system. Such systems are characterised by their semi-major axis a , their eccentricity e , their period p , their total mass $m_t = m_1 + m_2$,

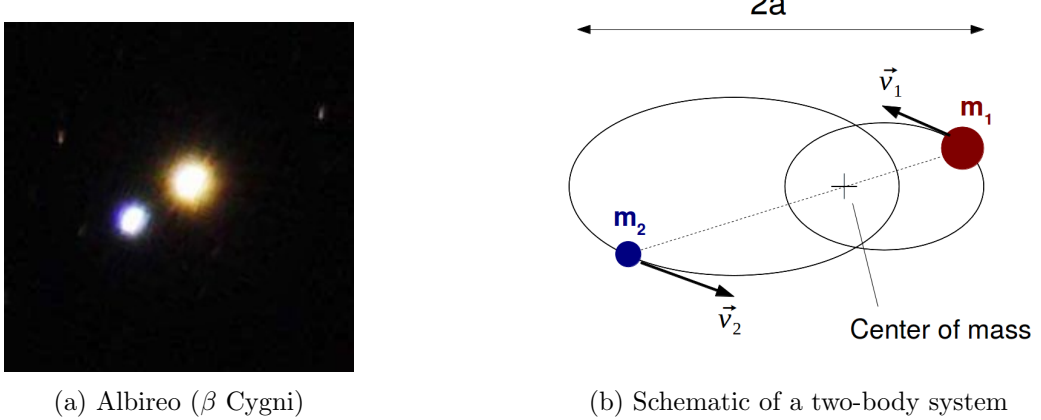


Figure 1.10: (a) Hubble observation of the binary star Albireo, fifth brightest star in the Cygnus constellation. Albireo A, the red star, is a close binary system itself (not represented on (b) for simplicity). The pair has a period of 213 years and a semi-major axis $a \simeq 66$ AU.

mass ratio $q = m_2/m_1$ with m_1 being the primary, more massive than m_2 . Mass, period and semi-major axis are related by Kepler's third law:

$$\frac{Gm_t}{4\pi^2} = \frac{a^3}{p^2}. \quad (1.21)$$

Interestingly, expressed in AU, M_\odot and years, $G \simeq 4\pi^2$, thus the law can be written:

$$\left(\frac{m_t}{1M_\odot} \right) = \left(\frac{p}{1\text{yr}} \right) \left(\frac{a}{1\text{AU}} \right)^3. \quad (1.22)$$

The total energy of the binary can be expressed as a function of a and m_t :

$$E = -\frac{Gm_1m_2}{2a} \quad (1.23)$$

1.5.2 Why binaries ?

Binary stars are extremely important for a variety of reasons. They can be a reservoir of energy, supporting the core of a cluster against collapse by giving away their internal energy to perturbers, effectively ejecting stars and heating the system, affecting its global evolution and stopping core collapse (e.g [Heggie & Aarseth 1992](#)).

The statistical properties of binary star populations in dense stellar associations in particular may shed light on the discovery of multiple star-formation episodes in rich stellar clusters ([Anderson et al., 2009](#)). For instance, binary stars enhance strong dynamical interactions which in turn may speed-up evolution off the main sequence and so boost enrichment of the ISM through winds (e.g., [Tailo et al. 2015](#)). Tight binaries of short-lived massive stars may evolve to produce exotic stellar remnants including black hole progenitors ([Bacon, Sigurdsson & Davies, 1996](#); [Davies et al., 2009](#)). Blue stragglers, abnormally hot stars for the age of their host clusters, are thought to form in binary mergers, making them a dynamical record of the past binary population and dynamical state of the cluster ([Knigge, Leigh & Sills, 2009](#)).

Finally, accurate knowledge of binary populations in stellar clusters enable good estimation of their dynamical mass, as the integrated velocity dispersion is largely biased by the binaries internal motions, see [Rubenstein & Bailyn \(1997\)](#).

1.5.3 Multiplicity fraction

In a stellar population, some fraction of stars will be found in multiple systems: some in binaries and some in higher order hierarchies. A hierarchical triple is a stable 3-body bound system, a binary of which one of the component is a binary itself. The same principle applies to quadruple, quintuple, etc. One of the brightest stars in the night sky, Castor, is a sextuple hierarchical system, with 6 stars in a stable system.

Counting binaries and multiples is not straightforward: do you count triples as two binaries or three stars in a multiple system ? In their SPH simulation paper, [Goodwin, Whitworth & Ward-Thompson \(2004\)](#) discuss several ways to measure the degree of multiplicity among stars in a system, each of them quantifying different properties, such as companion probability, companion frequency or pairing factor.

Let S be the number of single stars, and B, T , and Q the number of binary-, triple-, and quadruple systems, respectively. The fraction of multiple stars bound in binaries, triples, .. to the total number of multiple plus single stars, is

$$f_m = \frac{B + T + Q}{S + B + T + Q}. \quad (1.24)$$

This last measure is used in seminal observational papers ([Duquennoy & Mayor, 1991](#); [Raghavan et al., 2010](#)) and is our adopted choice. As pointed out by [Hubber & Whitworth \(2005\)](#), f_m in Eq. (1.24) has several advantages: 1) it may be restricted to a given mass m , setting S_m the number of single stars, and B_m, T_m, Q_m the multiple stars with a primary of that mass ; 2) the multiplicity fraction is observationally robust: when a binary is being reclassified as a triple, or an even higher order multiple system, the fraction does not change. These definitions may be extended to cover a mass range in a coherent way, by substituting $m \rightarrow \langle m \rangle$, the mean value over the range. This is useful mostly when comparing systems with different stellar mass functions.

1.5.4 Observed population

A seminal survey of binary solar-type stars in the field was performed by [Duquennoy & Mayor \(1991\)](#). This seminal paper was updated and completed by [Raghavan et al. \(2010\)](#), who essentially confirmed the main results from the first study. They observed hundreds of F and G main-sequence stars in pairs and derived their binary parameters. The total binary fraction for these stars was found to be $\sim 53\%$ as binaries are quite common in any stellar population. The authors also derived a period distribution, extending from less than a day to more than a Myr. The distribution was consistently well fitted by a log-normal distribution. The period distribution for F and G stars (as well as K and M stars, see [Fischer & Marcy 1992](#)) is:

$$f(\log P) \propto \exp \left[\frac{-(\log P - \mu_{\log P})}{2\sigma_{\log P}^2} \right] \quad (1.25)$$

with the peak value $\mu_{\log P} = 5.03$, about 300 years, and the dispersion $\sigma_{\log P} = 2.28$, the distribution is shown on Fig 1.11a.

[Raghavan et al. \(2010\)](#) also compiled several observational studies of binaries with primaries of various spectral types. High mass stars, types O,B,A, (from 30+ down to $2M_\odot$) have a high multiplicity fraction, about 75% while lower mass stars such as M-dwarfs only have 10-30% multiplicity, see Fig 1.11b. This trend of increasing multiplicity with increasing primary mass is found in many surveys. Binary surveys are easier in the field due to the very large sample and low stellar density. To perform similar studies in young star clusters is much harder due to source crowding and embedded stars. [Kouwenhoven et al. \(2007\)](#) attempted to characterize the birth binary population in the OB association Scorpius OB2. They found a very high multiplicity fraction, consistent with 100%, and a period distribution more consistent with a powerlaw than

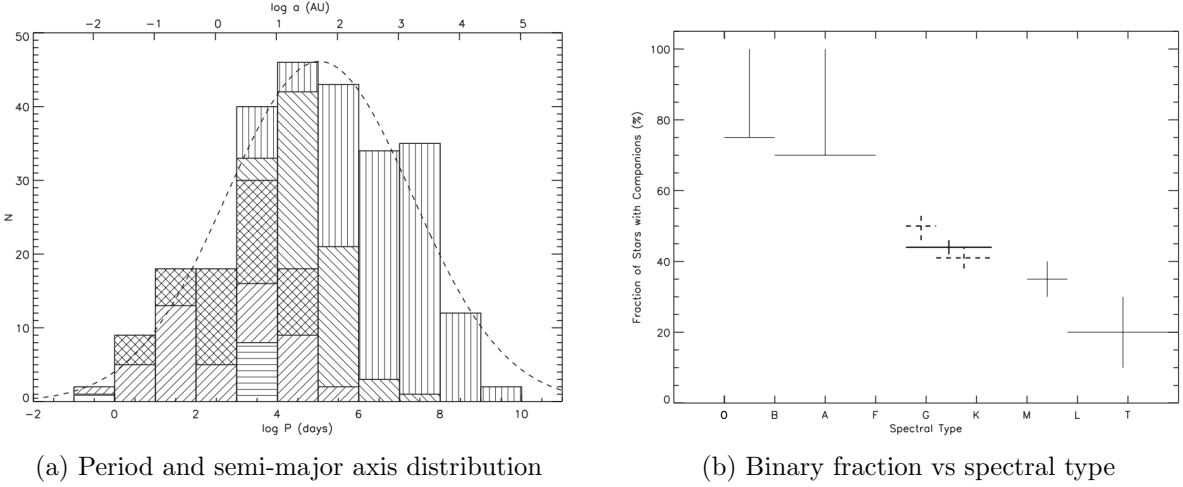


Figure 1.11: (a) shows the observed distribution of period and semi-major axis observed in the field. Different hatchings show different observation techniques: horizontal lines show unobserved companions detected by the proper-motion acceleration of components, positively sloped lines show spectroscopic binaries, negatively sloped lines visual binaries, cross hatching show objects found with both, and vertical lines are objects with common proper motions. (b) was compiled from several surveys, detailed in Fig 4.? (to come later). Both figures were extracted from [Raghavan et al. \(2010\)](#).

a log-normal distribution. From this survey and others, it is likely that the binary population in clusters undergoes an erosion through dynamical processing, with the field distribution as an end-result.

1.5.5 Simulate binary populations in clusters

As noted earlier, young clusters are born substructured, then undergo dynamical evolution. The rapid, global merging of sub-structures would bring together stars at a different stage of their formation (as in NGC1333, see [Foster et al. 2015](#)) while at the same time induce a shift from a clumpy Taurus-like profile to a more regular one. A simple but important question is how the internal dynamics of such complex configurations may affect the characteristics of a population of binary stars.

Many authors have explored this question through optimised initial conditions ([Kroupa & Burkert, 2001](#); [Marks & Kroupa, 2012](#)) or fractal configurations evolved with N-body integrators ([Parker, Goodwin & Allison, 2011](#); [Geller et al., 2013](#); [Parker & Meyer, 2014](#)). A common feature to all these studies is that the binary fraction drops over time regardless of their components (masses), due e.g. to close star-star encounters or heating from the external galactic tidal field, see Fig 1.12a. It was also shown that wide binaries are, as expected, more prone to destruction than more compact systems, as is illustrated by the evolution of the population seen in Fig 1.12b.

[Parker & Meyer \(2014\)](#) pointed out that the distribution of semi-major axes a of the field population is a strong function of the primary's mass: at fixed a , low-mass binaries carry less binding energy so the distribution cuts off at shorter separation (~ 20 AU) compared to that for binaries with a more massive primary (~ 300 AU). Their study of fractal initial conditions show that gravitational dynamics enhances the dissolution of low-mass systems. This then provides a clue to account for the larger relative fraction of heavy stars in binaries, such as seen in a compilation by [Raghavan et al. \(2010\)](#).

We note that hydrodynamical calculations of star formation have found young heavy stars to be preferentially found in dense clumps ([Maschberger et al., 2010](#)). Furthermore, it is not clear yet whether binary populations should be tailored according to the total system mass because

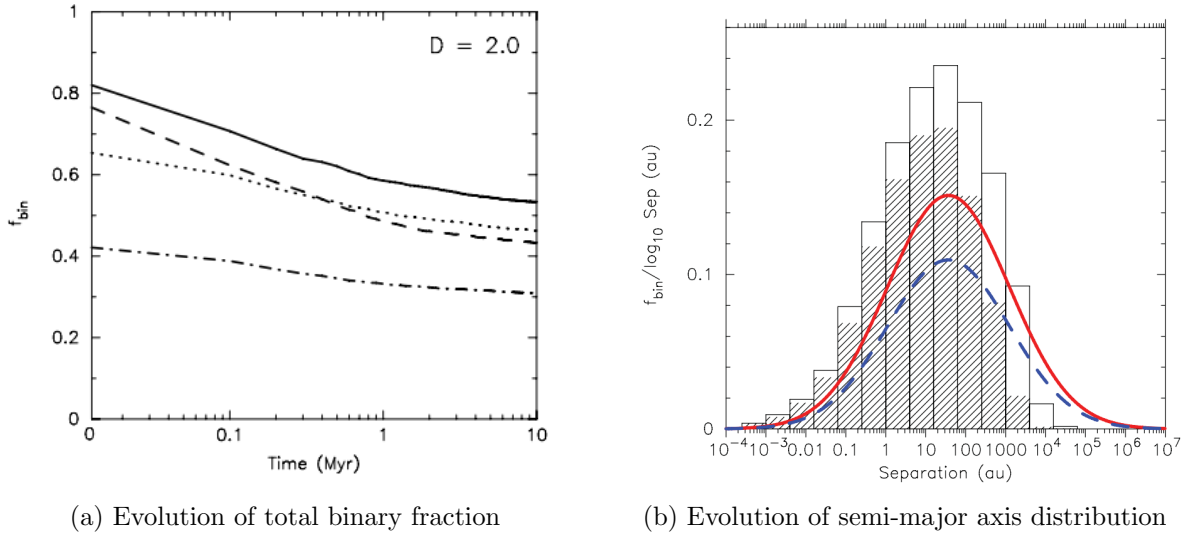


Figure 1.12: (a): total binary fraction over time in a subvirial fractal system. Corresponding models for the solid, dashed, dot-dashed and dotted are respectively 100% initial binary fraction with log-normal distribution, 100% fraction with Kroupa distribution, field-like fraction with log-normal distribution and field and 75% fraction with log-normal distribution. (b): 100% initial binary fraction with an initial log-normal distribution (open histogram) and the evolved distribution after 1Myr (hashed histogram). Solid red and dashed blue lines are fits for, respectively, the G-dwarf and M-dwarf populations. Both figures were extracted from [Parker, Goodwin & Allison \(2011\)](#).

of the limited range of $M \sim 10^2$ to $\sim 10^3 M_\odot$ of these studies ([Kroupa & Burkert, 2001](#); [Parker, Goodwin & Allison, 2011](#); [Parker & Meyer, 2014](#)). Recall that the intensity of the tidal field is a prime agent of binary heating. A trend with mass may be expected on the ground that the drive to equilibrium of more massive systems leads to deeper potential wells (e.g. [Aarseth, Lin & Papaloizou 1988](#); [Boily, Athanassoula & Kroupa 2002](#)). A steep potential will give rise to strong tidal fields which may disrupt bound sub-systems ([Boily et al., 2004](#); [Renaud, Gieles & Boily, 2011](#)). A definitive assessment of this effect is difficult to reach because the results are a strong function of the system initial mass distribution and kinetic energy content ([Boily, Athanassoula & Kroupa, 2002](#); [Caputo, de Vries & Portegies Zwart, 2014](#)).

1.6 NBODY6

NBODY6 is the second youngest iteration of the NBODY family, a suite of n-body integrators created by Sverre Aarseth. It can compute the gravitational interaction between up to 128,000 stars in a collisional fashion, meaning there is no softening of the potential, at any scale. This allows for very close binaries to form and remain in the system. To achieve its impressive performances, NBODY6 relies on several optimization techniques which have been first developed in the 1960s and 1970s, and improved ever since. Here will be developed five major features of NBODY6, in chronological order of their implementation: Hénon units, block time-step, KS-regularization, Hermite scheme and Ahmad-Cohen neighbour scheme. A full description can be found in Sverre Aarseth's book ([Aarseth, 2003](#)). Inspiration for this section should be credited to the user manual of NBODY6++, written by Emil Khalisi and Rainer Spurzem.

1.6.1 Hénon units

NBODY6 uses a set of units specifically invented for the Nbody gravitational problem, the Nbody units, or Hénon units (as prescribed by Douglas Heggie during the MODEST 2014 meeting). These units are based on three relations:

$$G = 1 \quad (1.26)$$

$$M_t = 1 \quad (1.27)$$

$$E = -\frac{1}{4} \quad (1.28)$$

With G the gravitational constant, M_t the total mass of the system and E total energy of the system. For a virialized system, that is a relaxed system in which the virial ratio

$$Q = -\frac{E_k}{E_p} = 0.5 \quad (1.29)$$

it comes that $E_k = 0.25$ and $E_p = -0.5$ and, considering the definition of the virial radius

$$R_v = -\frac{GM_t^2}{2E_p} = 1. \quad (1.30)$$

This unit system was designed for virialized systems, but can be used for out of equilibrium systems, as long as they are bound ($Q < 1$), with energy expressions functions of Q

$$E_p = -\frac{1}{4(1-Q)} \quad (1.31)$$

$$E_k = \frac{Q}{4(1-Q)} \quad (1.32)$$

which still fulfills the $E = -\frac{1}{4}$ condition. In practice, the Hénon mass, radius and velocities are obtained through

$$m_h = \frac{m}{M_t} \quad (1.33)$$

$$r_h = 4(1-Q)|E_p| \cdot r \quad (1.34)$$

$$v_h = \sqrt{\frac{Q}{4(1-Q)E_k}} \cdot v \quad (1.35)$$

with E_p and E_k being computed before rescaling with Hénon masses and $G = 1$. Such a system can be used as an input for NBODY6 without the need for the software to rescale anything.

1.6.2 Block time-step

In the first Nbody simulations, the system was integrated with an universal time-step, determined by the most accelerated star. A star in the outer regions of the cluster with a small velocity did not need to be updated that often. One of the first improvement was the introduction of individual time-step: each star is attributed its own time-step, depending on the force that is applied to it and its derivatives:

$$\Delta t_i = \eta \sqrt{\frac{|\mathbf{F}_i||\mathbf{F}_i^{(2)}| + |\mathbf{F}_i^{(1)}|^2}{|\mathbf{F}_i^{(1)}||\mathbf{F}_i^{(3)}| + |\mathbf{F}_i^{(2)}|^2}} \quad (1.36)$$

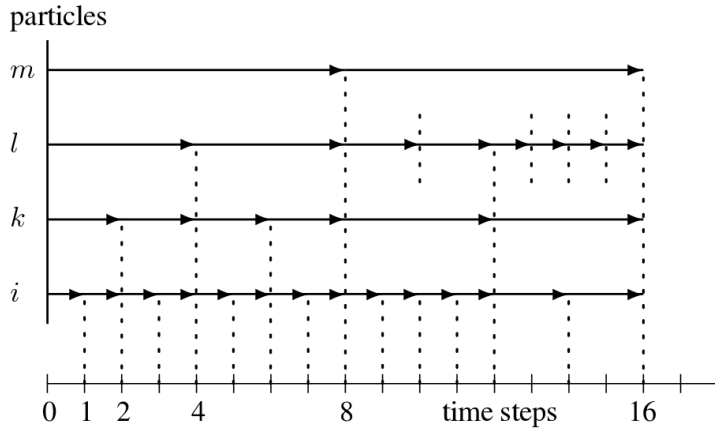


Figure 1.13: Illustration of block time steps on 4 particles. Particles get their positions updated for each arrow symbol, common time steps are shown as vertical dotted lines. Figure from NB6++ User Manual.

With $\mathbf{F}_i^{(j)}$ begin the j -th derivative of the force applied to particle i and η a user-defined accuracy parameter. Such a complex formulation is the result of extensive tests and is quite robust for many special cases. Individual time-steps leads to desynchronized particles, hence the need to interpolate the positions of other particles to compute \mathbf{F}_i , which was achieved through fourth-order polynomials.

To limit the amount of desynchronization, block-time steps were introduced. Instead of having as many time steps as particles, one only allows quantized power of 2 of an initial time step. $\Delta t_0, \frac{\Delta t_0}{2}, \frac{\Delta t_0}{4}, \frac{\Delta t_0}{2^2}$. All time steps are then commensurate and regularly fall back on the same time steps, minimizing the amount of interpolation during the force calculations. The concept is illustrated on Fig 1.13.

1.6.3 KS-regularization

Close binaries are extremely problematic in N-body simulations. They require a small time step as both binary components are much more accelerated than any other stars in the system, while the rest of the system is unaffected. Block time-step mitigate this problem, but the binary system still requires a lot of integration for an orbit that is essentially already known. Regularization is an answer to this problem. The essence of regularization is to decouple the integration of a sufficiently isolated sub-system, changing its coordinates to make integration easier, and including perturbations from external bodies. Several regularization scheme exist, NBODY6 implemented the Kustaanheimo-Stiefel method, or KS ([Kustaanheimo & Stiefel, 1965](#)).

Two bodies are candidates for regularization when their impact parameter is lower than the one needed for an orthogonal deviation, wherein their trajectory are deviated of 90° :

$$b_\perp = 2G \frac{m_1 + m_2}{v_\infty^2} \quad (1.37)$$

with m_i components masses and v_∞ relative velocity before encounter. This impact parameter can be converted to a time step computed through equation 1.36:

$$dt_{min} = \kappa \frac{\eta}{0.03} \left(\frac{r_{min}^3}{\langle m \rangle} \right)^{\frac{1}{2}}. \quad (1.38)$$

To be actually regularized, two bodies have to have a mutual time step lower than dt_{min} and fulfill two conditions:

$$\mathbf{R}_r \cdot \mathbf{V}_r > 0.1\sqrt{G(m_1 + m_2)R_r} \quad (1.39)$$

$$\frac{|\Delta \mathbf{F}_r| \cdot R_r^2}{G(m_1 + m_2)} < 0.25. \quad (1.40)$$

\mathbf{R}_r and \mathbf{V}_r being the relative velocities and positions of the particles and $|\Delta \mathbf{F}_r|$ the differential force applied to them, or perturbation. These conditions mean the subsystem is dynamically decoupled from external influence, but not unperturbed. When they are satisfied, the subsystem is regularized: it is replaced by the center of mass in the global system, and computed separately, with a set of changed coordinates. These coordinates are tailored for binary motion and close approach, they are well behaved when $R_r \rightarrow 0$. The influence of perturbers is taken into account when necessary. When the perturbation ratio (left hand side of equation 1.40) drops below a certain value, the system is considered isolated and it is not computed anymore, its parameters being stored until the perturbation is strong enough to warrant integration.

Regularisation have been extended to 3 and 4 bodies in hierarchical subsystems. NBODY6 can handle the regularization of a small-n non-hierarchical subsystem following the chain algorithm, see [Mikkola & Aarseth \(1993\)](#).

1.6.4 Hermite integration scheme

On the appropriate time-scales, the accelerations of the particles in a nbody system vary smoothly. It is therefore possible to predict the future acceleration then to correct the prediction, achieving high order integration with limited computational cost. The Hermite integration scheme was first introduced by [Makino \(1991\)](#) and has since been implemented within NBODY6 ([Aarseth, 2003](#)).

The first step is to compute the acceleration and its derivative at $t = t_0$, for all particles i :

$$\mathbf{a}_{0,i} = - \sum_{i \neq j} Gm_j \frac{\mathbf{R}}{R^3} \quad (1.41)$$

$$\dot{\mathbf{a}}_{0,i} = - \sum_{i \neq j} Gm_j \left[\frac{\mathbf{V}}{R^3} + \frac{3\mathbf{R}(\mathbf{V} \cdot \mathbf{R})}{R^3} \right] \quad (1.42)$$

with $\mathbf{R} = \mathbf{r}_{0,i} - \mathbf{r}_{0,j}$ and $\mathbf{V} = \mathbf{v}_{0,i} - \mathbf{v}_{0,j}$. Using these quantities, it is now possible to predict the positions and velocities at t through a Taylor serie, again for all particles i :

$$\mathbf{r}_{p,i}(t) = \mathbf{r}_0 + \mathbf{v}_0(t - t_0) + \mathbf{a}_{0,i} \frac{(t - t_0)^2}{2!} + \dot{\mathbf{a}}_{0,i} \frac{(t - t_0)^3}{3!} \quad (1.43)$$

$$\mathbf{v}_{p,i}(t) = \mathbf{v}_0 + \mathbf{a}_{0,i}(t - t_0) + \dot{\mathbf{a}}_{0,i} \frac{(t - t_0)^2}{2!} \quad (1.44)$$

The predicted accelerations and their derivatives $\mathbf{a}_{p,i}(t)$, $\dot{\mathbf{a}}_{p,i}(t)$ are computed by injecting $\mathbf{r}_{p,i}(t)$ and $\mathbf{v}_{p,i}(t)$ into equations 1.41 and 1.42. The accelerations at t , of which predicted values have just been computed, can also be obtained through Taylor series:

$$\mathbf{a}_i(t) = \mathbf{a}_{0,i} + \dot{\mathbf{a}}_{0,i}(t - t_0) + \mathbf{a}_{0,i}^{(2)} \frac{(t - t_0)^2}{2!} + \mathbf{a}_{0,i}^{(3)} \frac{(t - t_0)^3}{3!} \quad (1.45)$$

$$\dot{\mathbf{a}}_i(t) = \dot{\mathbf{a}}_{0,i} + \mathbf{a}_{0,i}^{(2)}(t - t_0) + \mathbf{a}_{0,i}^{(3)} \frac{(t - t_0)^2}{2!} \quad (1.46)$$

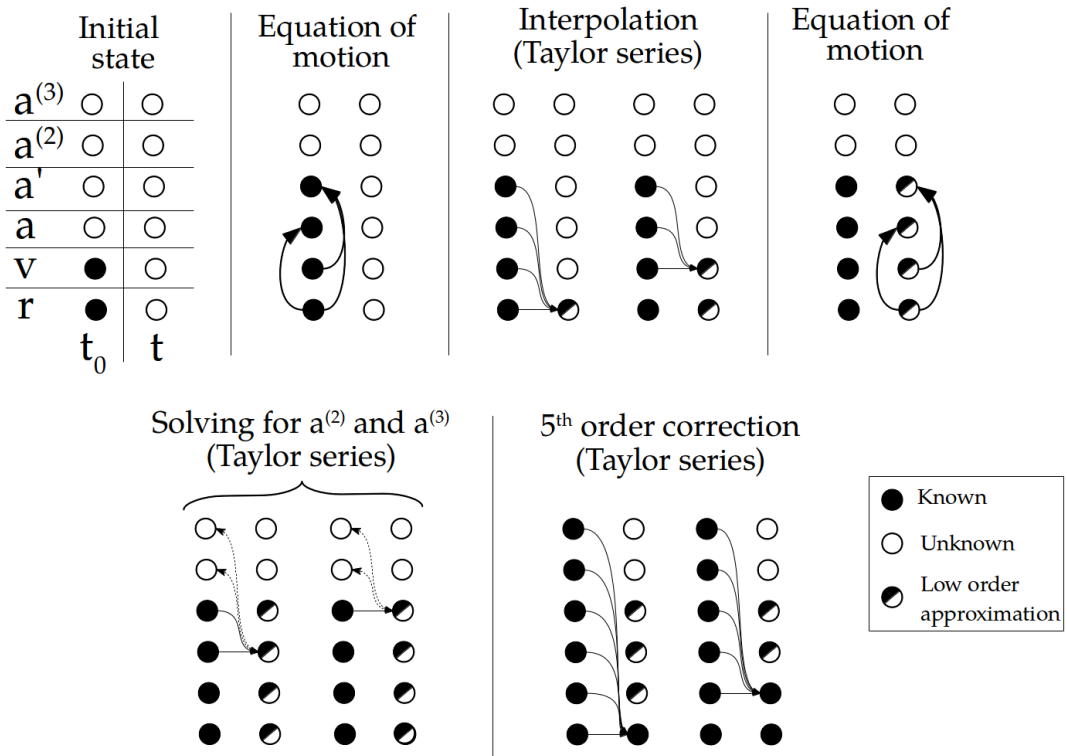


Figure 1.14: Summary of the Hermite scheme starting from known positions and velocities at t_0 to obtain 5th order values at t .

with $\mathbf{a}_{0,i}^{(2)}, \mathbf{a}_{0,i}^{(3)}$ the third and fourth derivative of the acceleration at $t = 0$. Note that these quantities are unknown for now. To take the derivatives of equation 1.42 would be too computationnaly expansive. Instead, $\mathbf{a}_{p,i}(t)$ and $\dot{\mathbf{a}}_{p,i}(t)$ are injected in the left hand side of equations 1.45 and 1.46 and solved for $\mathbf{a}_{0,i}^{(2)}$ and $\mathbf{a}_{0,i}^{(3)}$. This leads to the expressions:

$$\mathbf{a}_{0,i}^{(3)} = 12 \frac{\mathbf{a}_{0,i} - \mathbf{a}_{p,i}}{(t - t_0)^3} + 6 \frac{\dot{\mathbf{a}}_{0,i} - \dot{\mathbf{a}}_{p,i}}{(t - t_0)^3} \quad (1.47)$$

$$\mathbf{a}_{0,i}^{(2)} = -6 \frac{\mathbf{a}_{0,i} - \mathbf{a}_{p,i}}{(t - t_0)^2} - 2 \frac{2\dot{\mathbf{a}}_{0,i} + \dot{\mathbf{a}}_{p,i}}{t - t_0}. \quad (1.48)$$

The predicted values of positions and velocities are then corrected using the second and third order derivatives of acceleration, yeilding fifth order accurate values.

$$\mathbf{r}_{c,i}(t) = \mathbf{r}_{p,i}(t) + \mathbf{a}_{0,i}^{(2)} \frac{(t - t_0)^4}{4!} + \mathbf{a}_{0,i}^{(3)} \frac{(t - t_0)^5}{5!} \quad (1.49)$$

$$\mathbf{v}_{c,i}(t) = \mathbf{v}_{p,i}(t) + \mathbf{a}_{0,i}^{(2)} \frac{(t - t_0)^3}{3!} + \mathbf{a}_{0,i}^{(3)} \frac{(t - t_0)^4}{4!} \quad (1.50)$$

$$(1.51)$$

In a nutshell, the Hermite scheme is a way to obtain 5th order terms with limited cost. The steps are summarised in figure 1.14. First $r_0^{(2)}$ and $r_0^{(3)}$ are computed, then used to obtain predictions of $r_t^{(0)}$ and $r_t^{(1)}$, transformed with the equations of motions into predictions of $r_t^{(3)}$ and $r_t^{(4)}$. These last two can be expressed through Taylor series as functions of $r_0^{(3)}, r_0^{(4)}$ and $r_0^{(5)}$, which are solved for these last two terms. The predicted values of $r_t^{(0)}$ and $r_t^{(1)}$ are then corrected to the fifth order with $r_0^{(4)}$ and $r_0^{(5)}$.

The error for a single time step scales as $O(\Delta t^5)$. The Hermite scheme has shown itself very well suited for the block time step method, as the synchronization of particles limit the amount of prediction to be made, many positions at a given time being already known and computed with maximum accuracy.

1.6.5 Ahmad-Cohen neighbour scheme

For a given particle in an nbody system, the influence of direct neighbours changes on shorter timescales than the smooth potential from distant particles. The essence of the Ahmad-Cohen neighbour scheme is to decouple the two for computational efficiency ([Ahmad & Cohen, 1973](#)). The acceleration is splitted into two components:

$$\mathbf{a}_i = \mathbf{a}_{i,reg} + \mathbf{a}_{i,irr} \quad (1.52)$$

$\mathbf{a}_{i,irr}$ is the acceleration from particles inside a given "neighbour sphere" around particle i , while $\mathbf{a}_{i,reg}$ is the acceleration from all other, more distant, particles. Integration within the neighbours sphere, *irregular* integration, is decoupled from the global, *regular*, integration. Regular time steps, where complete force summation are performed over all particles with eq 1.41, are subdivided into irregular time steps, where regular acceleration is predicted and irregular acceleration is computed through a force summation on the $N_{i,nb}$ neighbours. The list of neighbours of i is updated every regular time step and contains the particles within a sphere of radius $R_{i,s}$ centered on i . Also added to the neighbour list are the particles within $2^{\frac{1}{3}}R_{i,s}$ that satisfy the condition

$$\mathbf{R} \cdot \mathbf{V} < 0.1 \frac{R_s^2}{\Delta T_{reg}} \quad (1.53)$$

with ΔT_{reg} the regular time step. This ensures that fast approaching particles are selected before they enter the actual neighbour sphere. $R_{i,s}$ is determined through local number density contrast and optimisation of the resulting $N_{i,nb}$.

When $N_{nb} \ll N$ for most particles, there is a great performance improvement, without loss of accuracy.

CHAPTER 2

The Hubble-Lemaître fragmented model: analytical approach

2.1 How to build a Hubble-Lemaître model

2.1.1 Initial state

The first step to obtain a HL-fragmented model is to build an uniform sphere model. The N stars, depending on the required membership, have to be distributed randomly in space inside a certain radius, producing an uniform density. This can be achieved by sampling separately the distance to the center and the angular position of each star, in a method analog as used in [Aarseth, Hénon & Wielen \(1974\)](#) for a Plummer model. The distance to the center should be sampled from the function:

$$f_R(X) = R_0 X^2 \quad (2.1)$$

With R_0 the bouding radius and X a random variable following a uniform probability law between 0 and 1. A direct uniform law for the radius would overpopulate the outer regions. The angles ϕ and θ , respectively azimuthal and polar angle in the physics convention, should be sampled from:

$$f_\phi(X_1) = 2\pi X_1 \quad (2.2)$$

$$f_\theta(X_2) = \arccos(X_2) \quad (2.3)$$

With X_1 following a uniform probability law between 0 and 1 and X_2 between -1 and 1. The cartesian coordinates are then found:

$$x = R \sin \theta \cos \phi \quad (2.4)$$

$$y = R \sin \theta \sin \phi \quad (2.5)$$

$$z = R \cos \theta \quad (2.6)$$

$$\quad \quad \quad (2.7)$$

The N particles are then homogeneously distributed in space in a sphere of radius R_0 . The next step is to attribute velocities. Unlike other models like the Plummer model, the velocities are here straightforward. We use the well known velocity field of neighbouring galaxies: velocities are radial from the Milky Way, larger with increasing distances, taking the form:

$$\mathbf{v} = H_0 \mathbf{r}, \quad (2.8)$$

with H_0 being an equivalent of the well-known Hubble parameter. For historical accuracy, I added the name of Georges Lemaître when I named my model. It has now been shown that the astronomical observations of redshifted galaxies and its interpretation as the consequence of an expanding universe predated Hubble's paper ([Hubble, 1929](#)). Georges Lemaître had published his conclusion on an expanding universe two years earlier ([Lemaître, 1927](#)). The account of this can be found in [Kragh & Smith \(2003\)](#); [van den Bergh \(2011\)](#) and [Freeman et al. \(2015\)](#).

An appropriate H_0 to obtain a fragmented subvirial model has to be inferior to 1.4 (see next section). The model obtained from this is then evolved through a nbody integrator, which in my case is NBODY6.

2.1.2 Fragmentation

The cluster expands, driven by the initial Hubble-Lemaître velocity field. During this expansion, poissonian fluctuation in density from the uniform model starts to grow: the part of the cluster with more mass initially attract more stars, forming clumps, clumps merge, spontaneously building substructure. These clumps will be analyzed in another section. If H_0 is well chosen, the expansion stops at some point, the apex, at which the initial kinetic energy has been spent and converted to potential energy: the cluster is now larger, substructured and subvirial, about to collapse. The apex time t_a of the end of the expansion and the critical value of H_0 can be derived from Newton's second law applied to an expanding spherical shell of matter.

We start from a uniform sphere of radius R_0 , total mass M . We consider spherical shells as mass elements, situated at distance r from the origin. As previously said, they are attributed a radial velocity following (for the shell at $r = R_0$) $\vec{v}_0 = H_0 \vec{R}_0 = H_0 R_0 \vec{u}_r$. We want to follow the radial motion of the last shell of mass m , situated at R from the origin. Newton's second law gives:

$$m \frac{dv}{dt} = -\frac{GMm}{R^2} \quad (2.9)$$

By multiplying on both sides by v and integrating between a given time and $t = 0$, one finds:

$$v^2(t) - v_0^2 = 2GM \left(\frac{1}{R} - \frac{1}{R_0} \right) \quad (2.10)$$

Which becomes, by taking $\nu = v/v_0$, $x = R/R_0$ and defining:

$$E_* = \frac{2GM}{R_0 v_0^2} \quad (2.11)$$

which is a dimensionless measure of the total energy of the system:

$$\nu^2 = 1 + E_* \left(\frac{1}{x} - 1 \right). \quad (2.12)$$

The evolution of the system has 3 outcomes, depending on the value of E_* :

- $E_* < 1$ The velocity is always strictly positive as the system expands ($x- > \infty$). The system is unbound.
- $E_* = 1$ The velocity approaches zero as the system expands. The expansion "stops at an infinite radius". The system is marginally bound.
- $E_* > 1$ The velocity reaches zero for a finite radius, the system is bound and will collapses back on itself once the expansion stops.

Using Hénon units, $G = 1$ and $M = 1$, and we choose $R_0=1$. Which gives a critical value E_* to have a bound system: $E_* = \frac{2}{H_0^2} < 1$. This means to have a bound system, which stops expanding at some point, one must have $H_0 < \sqrt{2}$. We only consider in the following the case in which $E_* < 1$. We have the expression

$$\nu = \sqrt{1 + E_* \left(\frac{1}{x} - 1 \right)} \quad (2.13)$$

Taking the time derivative gives:

$$\frac{d\nu}{dt} = -\frac{E_*}{2x^2} \left[1 + E_* \left(\frac{1}{x} - 1 \right) \right]^{-\frac{1}{2}} \frac{dx}{dt} \quad (2.14)$$

Combining this with (2.9), one obtains:

$$\frac{dx}{dt} = H_0 \sqrt{1 + E_* \left(\frac{1}{x} - 1 \right)} \quad (2.15)$$

which can be rewritten, using $\tilde{H}_0 = H_0 \sqrt{E_* - 1}$ and $x_t = \frac{E_*}{E_* - 1}$

$$\frac{dx}{dt} = \tilde{H}_0 \sqrt{\frac{x_t}{x} - 1} \quad (2.16)$$

x_a being the extent of the maximum expansion as we assumed a bound system. The subscript a is for apex. If we choose the notation $u = \frac{x}{x_a}$:

$$\sqrt{\frac{u}{u-1}} \frac{du}{dt} = \frac{\tilde{H}_0}{x_a} \quad (2.17)$$

We know that x varies from 1 to x_a , thus u varies from $1/x_a$ to 1. We can then make the change of variable $u = \sin^2 \theta$ and separate the variables:

$$\sqrt{\frac{\sin^2 \theta}{1 - \sin^2 \theta}} 2 \sin \theta \cos \theta d\theta = \frac{\tilde{H}_0}{x_a} dt \quad (2.18)$$

which becomes after simplifications:

$$[1 - \cos(2\theta)] d\theta = \frac{\tilde{H}_0}{x_a} dt. \quad (2.19)$$

We now integrate the expression from $t = 0$ to t , the time at which the expansion stops and x reaches x_a (wich implies $u_a = 1$ and $\theta_a = \pi/2$):

$$\int_{\theta_0}^{\pi/2} [1 - \cos(2\theta)] d\theta = \int_0^t \frac{\tilde{H}_0}{x_a} dt \quad (2.20)$$

$$\frac{\pi}{2} - \theta_0 + \frac{\sin(2\theta_0)}{2} = \frac{\tilde{H}_0}{x_a} t \quad (2.21)$$

$$\pi - 2\theta_0 + \frac{2}{\sqrt{x_a}} \sqrt{1 - \frac{1}{x_a}} = 2 \frac{\tilde{H}_0}{x_a} t \quad (2.22)$$

which boils down to the expression of the time at which the expansion stops:

$$t_a = \frac{E_* \left(\frac{\pi}{2} - \theta_0 \right) + \sqrt{E_* - 1}}{H_0 (E_* - 1)^{-\frac{3}{2}}}. \quad (2.23)$$

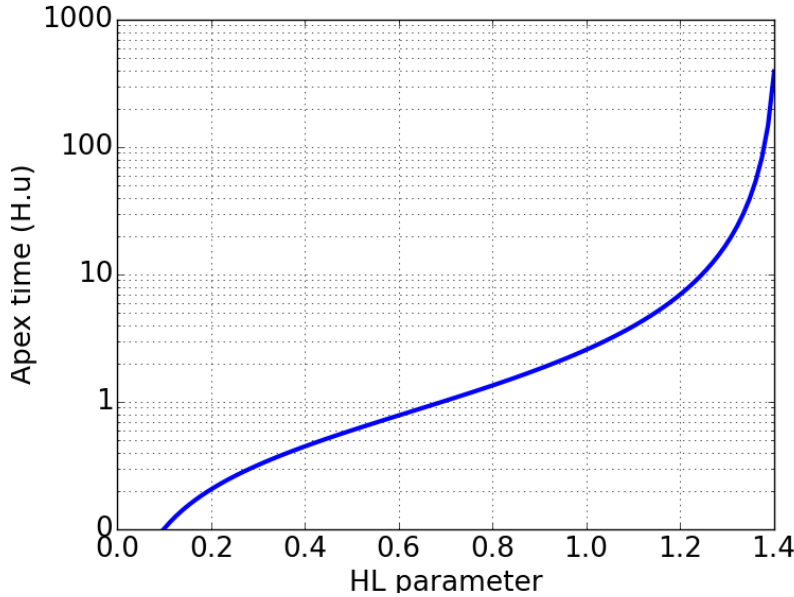


Figure 2.1: Theoretical values of the apex time, at which the system stops expanding, as a function of initial HL parameter, which tunes the strength of the initial expansion.

Recalling the quantities:

$$E_* = \frac{2GM}{R_0 v_0^2}; \quad x_a = \frac{E_*}{E_* - 1}; \quad \theta_0 = \sin^{-1} \left(\frac{1}{\sqrt{x_a}} \right) \quad (2.24)$$

See figure 2.1 for the value of t_a as a function of H_0

2.2 The growth of overdensities: analytical study

2.2.1 Working equations

During the expansion and in the mean-field approximation, the mass inside any shell of radius $r(t)$ is conserved as they move outwards. The position of a mass element is known in parametric form from a rescaling of its initial coordinates and we may write

$$\mathbf{r}(t) = a(t)\mathbf{x} \quad (2.25)$$

$$\mathbf{v}(t) = \dot{a}\mathbf{x} = H(t)\mathbf{r} \quad (2.26)$$

where \mathbf{x} is a co-moving coordinate of position, and $a(t)$ is a dimensionless function of time. The flow is homological and no shell-crossing takes place. It is convenient to introduce a dimensionless time τ such that

$$t = \frac{\tau}{H_0}. \quad (2.27)$$

We then have from equation (2.19):

$$\left[\frac{E_*}{E_* - 1} \right]^{\frac{3}{2}} [2\theta - \sin 2\theta] \Big|_{\theta_0}^\theta = 2\sqrt{E_*}\tau \quad (2.28)$$

Table 2.1: Summary of main variables.

E	Total system energy
E_*	Dimensionless total energy
W	Total potential energy
E_k	Total kinetic energy
\mathcal{M}	Total system mass
R_o	Initial bounding radius
H_0	Initial Hubble parameter
v_o	Initial velocity at bounding radius
H	Variable Hubble parameter
τ	Dimensionless time
x	Comoving spatial coordinate
$a(t)$	Rescaling function
θ	Calculation angle
$\nu(\tau)$	Dimensionless velocity $1 + E_*(1/a(\tau) - 1)$
ξ	Radial displacement from comoving
$\delta\rho, \delta M, \delta\rho$	Perturbed quantities
$\mu(\tau)$	Central point mass
η	Peculiar velocity $d\xi/dt$

with

$$a(t) \equiv \frac{\sin^2 \theta(\tau)}{\sin^2 \theta_o} \quad (2.29)$$

The dimensionless energy parameter E_* satisfies $E_* > 1$ for bound systems. The origin of time $\tau = 0$ coincides with the angle θ_o found from solving $\sin^2 \theta_o = (E_* - 1)/E_*$. The solution (2.28) provides the time-sequence for the position and velocity of any shell $0 < x < R_o$ as parametric functions of τ :

$$v(t) = H_0 x \sqrt{1 + E_* \left(\frac{1}{a(\tau)} - 1 \right)} = H_0 x \nu(\tau) \quad (2.30a)$$

$$H(t) = H_0 \frac{\nu(\tau)}{a(\tau)} \quad (2.30b)$$

$$\rho(t) = \frac{3\mathcal{M}}{4\pi R_o^3} \frac{1}{a^3(\tau)} . \quad (2.30c)$$

2.2.2 Linear density perturbation

An actual Hubble-Lemaître model will develop 3-dimensional clumps during the expansion, but to get an analytic view of this process, it is necessary to fall back on one dimension. This will shed light on the growth of clumps and help understand general trends in the system.

We follow radial density perturbations in the expanding uniform sphere described by equations (2.28) and (2.29), as the local density increase also gauges the rise in velocity dispersion. A simplified calculation for radial modes of perturbation in the linear approximation will be derived here, with the goal to determine when the clumps become mostly self-gravitating. A more detailed analysis can be found in the classic work by [Friedman & Schutz \(1978\)](#), [Peebles \(1980\)](#) and [Aarseth, Lin & Papaloizou \(1988\)](#).

We introduce a Lagrangian perturbation in the position of a shell of constant mass by substituting $\mathbf{x} \rightarrow \mathbf{x} + \boldsymbol{\xi}(\mathbf{x}, t)$ and we set $\boldsymbol{\xi} = \xi \mathbf{u}_r$ for a radial displacement. A linear treatment of the continuity equation yields an expression for the perturbed density. Starting from the well known equation

$$\frac{\partial \rho}{\partial t} + \nabla(\rho \mathbf{v}) = 0 \quad (2.31)$$

which transforms into

$$\delta\rho + \nabla(\rho \mathbf{v} \delta t) = 0. \quad (2.32)$$

We make use of the equivalence:

$$\frac{\partial}{\partial r} \equiv \frac{1}{a} \frac{\partial}{\partial x} \quad (2.33)$$

to obtain, considering $\mathbf{v} \delta t = \delta \mathbf{r} = a(\tau) \boldsymbol{\xi}$ and ignoring second order terms from $\delta\rho$:

$$\delta\rho = -\nabla \cdot (a\rho \boldsymbol{\xi}) = -\rho(\tau) \frac{1}{x^2} \frac{\partial}{\partial x} (x^2 \xi) \quad (2.34)$$

which leads to a perturbation in the mass integrated up to radius r

$$\delta M(< r) = \delta \left(\rho \frac{4}{3} \pi r^3 \right) \quad (2.35)$$

$$= -4\pi a^3(\tau) \rho x^2 \xi. \quad (2.36)$$

Poisson's equation in spherical symmetry gives the perturbed potential

$$\frac{1}{r^2} \frac{\partial}{\partial r} r^2 \frac{\partial}{\partial r} \delta\phi = \frac{1}{a^2} \frac{1}{x^2} \frac{\partial}{\partial x} x^2 \frac{\partial}{\partial x} \delta\phi = 4\pi G \delta\rho. \quad (2.37)$$

Substituting for $\delta\rho$ from (2.34) in (2.37), and using (2.33), we obtain:

$$\frac{\partial}{\partial x} \left(x^2 \frac{\partial \delta\phi}{\partial x} \right) = -4\pi a^2 G \rho_0 \frac{\partial}{\partial x} (x^2 \xi) \quad (2.38)$$

Integrating once, we obtain the general solution

$$a(\tau) \nabla \delta\phi = \frac{3G\mathcal{M}}{R_o^3} \left(-\xi + R_o^3 \frac{\mu(\tau)}{x^2} \right) \quad (2.39)$$

where μ stands for a central point mass. A point mass would form by shell crossing at the center of coordinates. In an expanding system, shell crossing at the center is unlikely. For that reason, we make $\mu = 0$ in the remainder of this paper.

The equations of motion at co-moving radius $x + \xi(x, t)$ can be expanded to first order in ξ ; identifying terms of the same order we obtain (with $\partial/\partial x = \nabla_x$)

$$a(\tau) \frac{d^2}{dt^2} \xi + 2\dot{a}(\tau) \frac{d}{dt} \xi = -\nabla \delta\phi - \xi \nabla_x \nabla \phi - \ddot{a}(\tau) \xi. \quad (2.40)$$

The second and third terms on the right-hand side cancel out exactly ; the first is known from (2.39). It is standard practice to demote this second-order dynamical equation to a set of first order equations ; for convenience we use the initial system radius R_o as unit of length, and we introduce starred (*) dimensionless variables. We then have $x = R_o x_*$, $\xi = R_o \xi_*$, and so on. After simplification using the dimensionless functions of τ defined in (2.27) and recalling that $\dot{a}(\tau) = H(\tau)$, the differential equations read

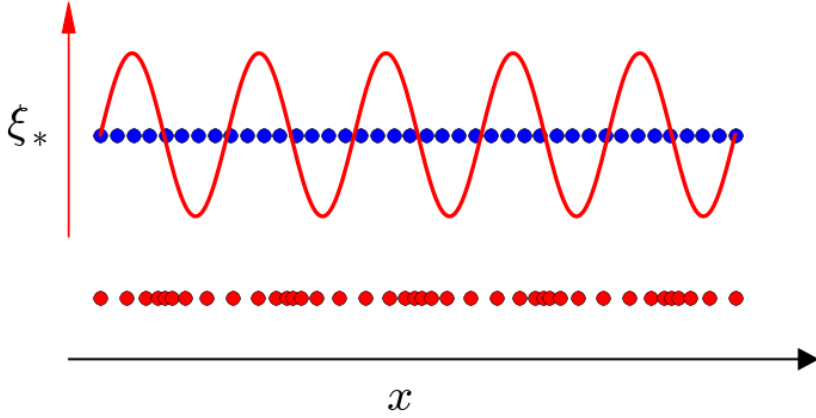


Figure 2.2: Schematic illustration of a sinewave density perturbation (red line) applied to an uniform distribution of matter (blue dots) and the resulting distribution (red dots). The mode displayed here has $m = 10$ and its amplitude was exaggerated.

$$\frac{d}{d\tau} \xi_* = \eta_*(\tau) \quad (2.41a)$$

$$\frac{d}{d\tau} \eta_* = \frac{3E_*}{a(\tau)^2} \xi_* - 2 \frac{H(\tau)}{a(\tau)} \eta_* \quad (2.41b)$$

where we have introduced the peculiar velocity $\eta \equiv d\xi/dt = H_0 R_o \eta_*$.

2.2.3 Consistent initial conditions

Initial conditions

Equations (2.41) can be numerically integrated with an explicit integration scheme once the initial values R_o, H_0, \mathcal{M} and $\xi_*(0)$ are specified and values of $a(\tau)$ are obtained from (2.29) and (2.28). All functions of the dimensionless time τ are set to unity except that $\eta_*(0) = 0$. The solution is shown on Fig 2.3a.

The Hubble parameter $H(\tau) \rightarrow 0$ when the system reaches a maximum radius $a(\tau)R_o$ ($\theta[\tau] = \pi/2$ in Eq. 2.29). Around that time, equation (2.41b) transforms so the Lagrangian displacement ξ_* grows exponentially, and the clumps become the densest. We investigate the growth of a density perturbation as a Fourier fragmentation mode before that. In the linear regime, such a mode is decoupled from all the others. We pick

$$\xi_*(x, 0) = \xi_*^{(o)} \sin(kx), \quad (2.42)$$

where the wavenumber k is such that $kR_o = m\pi$ and $\xi_*(R_o, 0) = \xi_*(R_o, \tau) = 0$ at all times. When deciding which wavenumber to choose, we must bear in mind the finite numerical resolution of the models that we will present later. The next subsection gives quantitative arguments that motivated our choices. The aspect of the perturbed system is shown as a rough schematic on Fig 2.2.

Fourier modes: resolution issues

An uniform distribution of N discrete mass elements cannot resolve infinitely small wavelengths, the lower limit depends on the mean separation $l_o \simeq R_o/N^{1/3}$ which gives a reference wavelength $\lambda/R_o = \lambda_* \geq N^{-1/3}$ for a resolved Fourier mode. Since $kR_o = m\pi$, this also implies that $m \leq 2N^{1/3}$.

The initial amplitude $\xi_*^{(o)}$ of the perturbation can be tailored to the actual Poissonian fluctuations in a uniform distribution of discrete elements. The radius bounding a shell of N mass elements distributed randomly will fluctuate freely between r , $r + \delta r$ due to stochasticity. The radius r of a uniform sphere being a power-law of mass M , we find:

$$\frac{\delta r}{r} = \frac{1}{3} \frac{\delta M}{M} = \frac{1}{3} \frac{\delta N}{N} = \frac{1}{3} N^{-\frac{1}{2}} \quad (2.43)$$

for identical mass elements. We then compute the number-averaged value $\langle \delta r/r \rangle$ by summing over all elements from 1 to N and dividing by $N - 1$ to find

$$\langle \frac{\delta r}{r} \rangle = \langle \xi_*^{(o)} \rangle = \frac{2}{3} \frac{\sqrt{N} - 1}{N - 1}. \quad (2.44)$$

Thus the mean amplitude (in units of R_o) is $\langle \xi_*^{(o)} \rangle \simeq 1/10$ for $N = 32$ which drops to $\langle \xi_*^{(o)} \rangle \simeq 6 \times 10^{-4}$ when $N = 10^6$. We checked that the mode with the shortest wavelength λ_* still resolved would have a displacement $\langle \xi_*^{(o)} \rangle$ initially smaller than $\lambda_*/2$ for any sensible value of N . This in turn implies that this mode may grow over time to reach an amplitude $\xi_*(x, \tau) \simeq \lambda_*/2$, which is the point when orbit-crossing between shells of constant mass must occur. In other words, at this point, the overdensity transitions from linear convergence of particles to collisional evolution (not covered by Eqs. 2.41). The time when shell-crossing occurs can be seen as the "birth" of a clump, whether this clumps undergoes consequent two-body relaxation effects depends on its characteristics, such as density and membership, and the remaining time before the end of expansion.

2.2.4 Segregation time-scale

We already noted that H_0^{-1} sets a time-scale for the expansion of the system. That time should be chosen so that it matches the hydrodynamical star formation phase of 0.5 – 1 Myr (Maschberger & Clarke, 2011; Bate, Tricco & Price, 2014). When $H(\tau) = 0$ and the expansion is over, the stars relax to a new equilibrium driven by star-star interactions. Therefore we need to address first the internal dynamics in clumps in time units of H_0^{-1} , before discussing the later phase of violent relaxation and consider the system as a whole. The definitions are the same, only the face values change between the two phases of evolution.

Let us consider a clump of membership N_λ initiated by a Fourier mode of wavelength λ . With its total density $\rho + \delta\rho$ given by Eq. (2.34), we may write

$$\rho_g = \frac{\rho_o}{a^3(\tau)} \left(1 + \frac{\delta\rho}{\rho} \right) \equiv \frac{\rho_o}{a^3(\tau)} \rho_*. \quad (2.45)$$

Combining this with Eqs. (1.5), (1.6) and (1.10) from the introduction, the mass-segregation timescale in the clump now reads:

$$t_{ms} = \frac{0.138}{6} \pi \left(\frac{3}{4\pi} \right)^{1/2} \frac{\langle m_* \rangle}{\max\{m_*\}} \frac{N_\lambda}{\ln 0.4N_\lambda} (G\rho_g)^{-\frac{1}{2}}. \quad (2.46)$$

Making use of the equality

$$\frac{4\pi}{3} G\rho_o = H_0^2 E_*, \quad (2.47)$$

the last three relations simplify to the expression of the new dimensionless mass-segregation timescale:

$$\tau_{ms} = H_0 t_{ms} = \frac{0.138}{6} \pi \frac{a_\lambda^{3/2}}{(\rho_* E_*)^{1/2}} \frac{\langle m_* \rangle}{\max\{m_*\}} \frac{N_\lambda}{\ln 0.4N_\lambda} \quad (2.48)$$

where a_λ refers to the expansion factor $a(\tau)$ evaluated at time τ when $\xi_* \simeq \lambda_*/2$. Note that our use of Eq. (2.34) to compute ρ_g means that the gravitational radius r_g does not have its usual definition based on the gravitational energy W of the system. Linking ρ_g to R_g in this way has the advantage that R_g is not derived from an implied mass profile, which is (by definition) not resolved here.

Clearly the segregation time depends strongly on the mass spectrum of individual clumps, on their membership N_λ , as well as the density contrast $\rho_*(\tau_\lambda)$. We find the density contrast from (2.42) and (2.34),

$$\frac{\delta\rho}{\rho}\Big|_{\tau=0} = -\frac{1}{x^2}\frac{\partial}{\partial x^2}x^2\xi = -\left(2\frac{\sin m\pi x_*}{m\pi x_*} + \cos m\pi x_*\right)m\pi\xi_*^{(o)}$$

which admits an upper-bound of $3m\pi\xi_*^{(o)}$. In the course of evolution, the initial amplitude of perturbation grows to $\xi_* = \lambda_*/2$ so that the density contrast peaks at

$$\rho_* = 1 + \frac{\delta\rho}{\rho} = 1 + 3m\pi\lambda_*/2 = 1 + 3\pi, \quad (2.49)$$

where the last substitution follows from the definition of the integer m . The mass M_λ in a shell bounded by $r, r + \lambda$, is known from the unperturbed density profile ; in terms of the total system mass \mathcal{M} , we find

$$\frac{M_\lambda}{\mathcal{M}} = (\overline{x_*^2} + \lambda_*^2/4)\lambda_* = (1 + \lambda_*^2/4)\lambda_*, \quad (2.50)$$

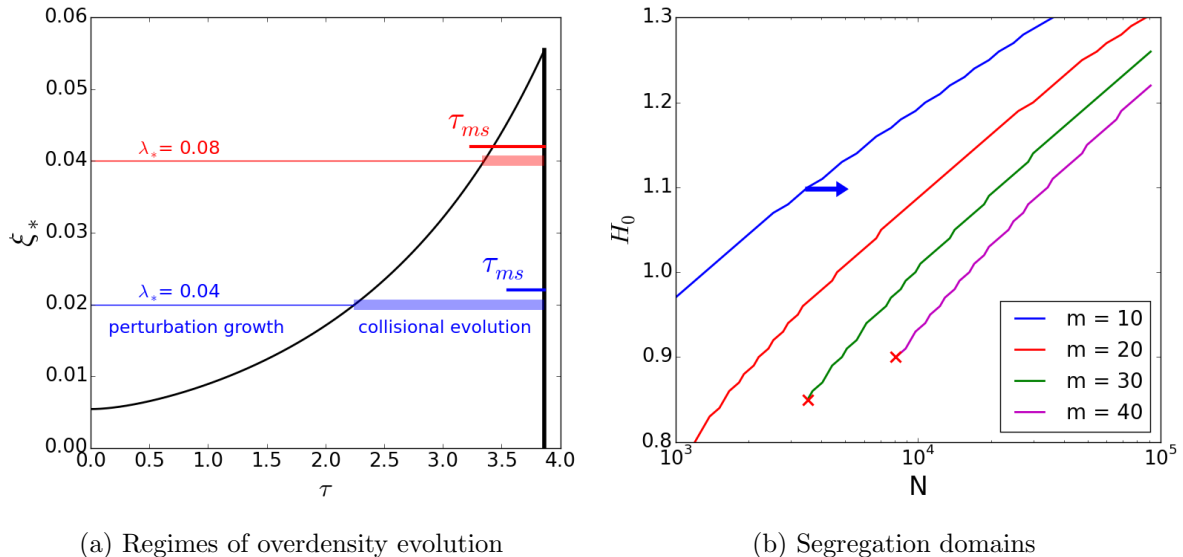
where we have replaced $3x_*^2$ by its space-averaged value in the last step. Eq. (2.50) provides an estimate of bound mass of a clump formed through the growth of a radial perturbation mode. If all the stars have equal mass, or, if the stellar mass function is symmetric with respect to the mean value $\langle m_* \rangle$, the ratio of the number N_λ of stars in the clump to the total number N is in the same proportion as $\frac{M_\lambda}{\mathcal{M}}$. We find an estimate for N_λ which reads

$$N_\lambda = N \left(1 + \frac{\lambda_*^2}{4}\right) \lambda_*. \quad (2.51)$$

We argued in §2.3.2 that a resolved mode should have $\lambda_* \geq N^{-1/3}$, which translates as:

$$N_\lambda > N^{2/3} \left(1 + \frac{N^{-2/3}}{4}\right). \quad (2.52)$$

This number inserted into Eq.(2.48) leads to a rough picture of the segregation process in clumps. The rate of mass segregation leans on the choice of initial value for the expansion phase, H_0 . In the limit when $H_0 = 0$, there is no expansion whatsoever, and the clumps form unsegregated (aside from random associations when attributing positions and velocities to the stars) during global infall. If by contrast, the expansion is vigorous, $a_\lambda \gg 1$, and the segregation timescale remains large. For $N \sim 10^4$, we compute from (2.52) $N_\lambda \gtrsim 464$: a clump with that many stars will mass-segregate rapidly only if its stellar mass function includes very massive stars. We note that one-dimensional (radial) modes would in fact split into several smaller fragments in a three-dimensional calculation.¹ We expect the clumps to form quickly and contain $N_\lambda \ll 464$ stars, so that the internal dynamics will drive mass segregation *before* the system expansion stops. Because this depends in the details on H_0 and other important parameters, we defer the analysis to §?? and N-body simulations.



(a) Regimes of overdensity evolution

(b) Segregation domains

Figure 2.3: (a): growth of perturbation ξ_* over dimensionless time τ until the end of expansion at $\tau = 3.84$. An overdensity seeded with a wavelength λ_* begins its collisional evolution when ξ_* reaches $\frac{\lambda_*}{2}$. These regimes are illustrated for $\lambda_* = 0.04$ and $\lambda_* = 0.08$. The overdensities have to evolve collisionally for at least τ_{ms} to mass-segregate. This time-scale is also shown for each case. The blue case evolves collisionally for several τ_{ms} and will end up mass-segregated, while the red case visibly don't have enough time to segregate. Modes of large wavelength tend to produce less mass-segregated clumps. (b) for a given number of nodes m , a model on the right of the corresponding line (arrow for $m = 10$) will have mass-segregated overdensities at the end of the expansion, while on the left, the collisional evolution is too short for segregation to set in. The red crosses show the minimum N below which the modes cannot be resolved.

2.2.5 Example with $N = 15000$

We now make use of all previous development to follow the evolution of a perturbation in a given system and assess its dynamical state.

To ease comparisons with N-body calculations cast in standard Hénon units, we set $\mathcal{M} = G = R_o = 1$ and use $H_0 = 1.0833.. \simeq 1$ so that the total binding energy $E = -1/4$. The Hubble expansion proceeds until a time $t = \tau/H_0 \simeq 3.87/H_0$, when $H = 0$ and the bounding radius R reaches $R = a(\tau)R_o \simeq 2.4R_o$. The evolution time up to that point coincides almost exactly with the *current* global system free-fall time of ≈ 4.1 time units. System-wide collapse to the barycentre will ensue on the same time-scale, but now this process will involve the merging / scattering of several high-density clumps.

The mass of individual stars follow a truncated [Salpeter \(1955\)](#) distribution function, where the distribution function $dN/dm \propto m_*^{-\alpha}$ with index $\alpha = 2.35$ for masses in the range $0.3M_\odot < m_* < 100M_\odot$ giving a mean value of $\simeq 1M_\odot$. We chose this form mainly for simplicity, and for ease of calculations.

Let us fix $E_* = 6/7$, with $H_0 = 1$ and set $N = 15000$ as reference². We compute a mean initial amplitude of perturbation $\xi_*^{(o)} \approx 0.005$ with a shortest-resolved wavelength $\lambda_* \approx 0.04$. Fig. 2.3a displays the solution from integrating Eqs. (2.41). The amplitude $\xi_*(\tau)$ grows monotonically and crosses the values $\lambda_*/2$ at $\tau \approx 2.3$: thereafter the perturbation enters a non-linear regime of evolution during which the internal dynamics may become collisional ($\Delta\tau > \delta\tau_{ms}$). A second case is depicted on Fig. 2.3a, where the wavelength $\lambda_* = 0.08$ and the perturbation reaches amplitude $\xi_* = \lambda_*/2$ at $\tau \approx 3.6$: there is then too little time left before the end of the Hubble expansion phase for a clump of stars to evolve collisionally ($\Delta\tau < \delta\tau_{ms}$).

The dynamical state of individual clumps is clearly a question of membership N_λ and mass spectrum as shown in (2.48). We have been arguing that most small-size clumps will show collisional internal evolution : a small cluster of stars would lose low-mass stars in the process and so have an increased ratio of average- to maximum stellar mass. It is not clear, then, whether this trend is strong enough to compensate for the (almost) linear dependence on membership.

¹ A full-grown radial mode forms a thin shell subject to fragmentation. See *e.g.* [Ehlerova et al. \(1997\)](#); [Wünsch et al. \(2010\)](#).

²The more accurate value is $H_0 = 1 + 1/12 = 1.0833$ but we rounded up to 1 to simplify the discussion

CHAPTER 3

Nbody application

3.1 Approaching the N-body simulations

After the previous analytical study, we present here the characteristics of numerically obtained Hubble-Lemaître fragmented models. The integration was performed with NBODY6, which treats the gravitational forces of stars with no softening of the potential. An example of the evolution of the system is shown on Fig 3.1.

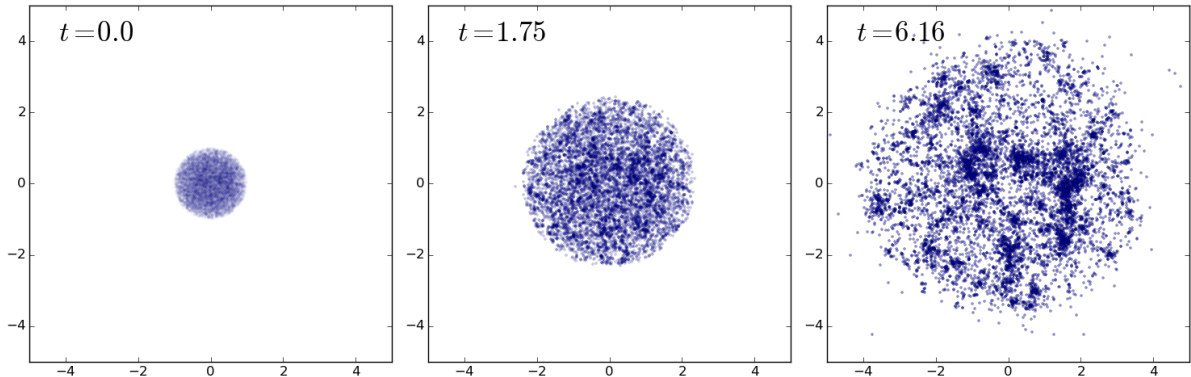


Figure 3.1: Progressive fragmentation through the Hubble expansion. The left panel shows the initial uniform sphere; the middle panel, an intermediate step, slightly fragmented with a slowed down expansion; the right panel is the final stage, when the expansion has stopped and the fragmentation is fully developed. $N=10000$ particles were used in this N-body model, with $H_0 = 1.0$. Time and coordinates are in Hénon units.

3.1.1 Presentation of the runs

We draw N stars from an Salpeter distribution function which we truncate by default to $100M_\odot$; in some calculations we will use a lower bound of $20M_\odot$, and in others we use identical masses. The code preserves the total energy and angular momentum to better than one part in 10^4 for integration over ~ 100 time units.

3.1.2 Clump finding algorithm

As seen on Fig 3.1, once expansion stops, the distribution is roughly spherical and visibly clumpy. By clump we mean here a local overdensity of stars. To characterize the model is to characterize these substructures. Such analysis requires to find and isolate clumps, using an efficient

clump-identification algorithm (or, *halo-finding* in cosmology). Several methods are commonly used such as the HOP algorithm (Eisenstein & Hut, 1998; Skory et al., 2010) which relies on attributing local densities to each particle and separating the clumps through density thresholds. The HOP algorithm is very robust on large cosmological data sets. However, our calculations have comparatively coarse statistics and noisy density fields. This issue, coupled with the large number of free parameters of the HOP algorithm, makes the method less appealing.

Instead we follow Maschberger et al. (2010) who adapted the minimum spanning tree (MST ; see e.g. Allison et al. 2009b; Olczak, Spurzem & Henning 2011) technique to the detection of clumps. A spanning tree is a set of edges connecting a group of particles but without closed loops ; the MST seeks to minimise the total length of the edges. One may then construct the MST for the whole system, and then delete all edges larger than a chosen cutting length, d_{cut} . The sub-sets that are still connected are labeled as clumps. This process is illustrated in Fig 3.2. In practice a minimum sub-set size N_d is also chosen so as to avoid many small-N subgroups : experience led us to choose $N_d = 12$ for the minimum number of stars per clump.

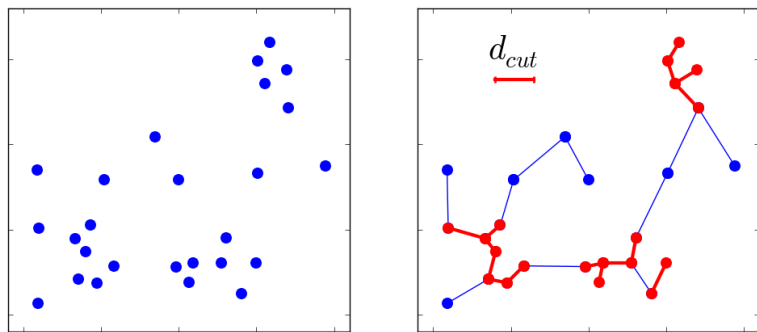


Figure 3.2: Illustration of a Minimum Spanning Tree and its use to isolate subgroups, using a cutting length d_{cut} .

With N_d fixed, the length d_{cut} is then the only free parameter left. There is some freedom in choosing an appropriate value. Maschberger et al. (2010) fixed the value of d_{cut} by visual inspection of clumps. We instead identified clumps in a fragmented system for a range of values for d_{cut} and settled for the value which optimised the number of identifications. This is shown on Fig. 3.3a for an $N = 80k$ fully-fragmented Hubble model. For small d_{cut} 's, the number of detected clumps at first increases rapidly. The rise is due to the length d_{cut} initially being small compared with the typical volume spawned by N_d or more nearest-neighbours. Beyond a certain value, a transition to another regime occurs, whereby the algorithm starts to connect previously separated clumps, counting them as one. The number of clumps thereafter begins to decrease. The value $d_{cut} \approx 0.024$ H.u optimises the outcome of the clump-search. This is a generic feature of the MST algorithm and we have adopted the same strategy throughout, adapting the value of d_{cut} to the number N of stars used.

Another method to find the critical cutting length was used by Gutermuth et al. (2009); Kirk & Myers (2011). In these works, the authors build the MST, then trace the cumulative distribution function of all edges in the tree. In a clumpy configuration, there are at least two regimes: the "intra-clump" regime, with the majority of small edges, and the "inter-clump" regime with longer, scarcer edges. The intersection of a fit to these regimes provide a good cutting length for clump detection. This procedure was applied to our system and gave the same result than the clump count, as shown on Fig ??.

On Fig. 3.4, a sub-set of the model is shown where we have identified stars that belong to clumps with filled symbols. The three panels on that figure are each for a different value of d_{cut} ,

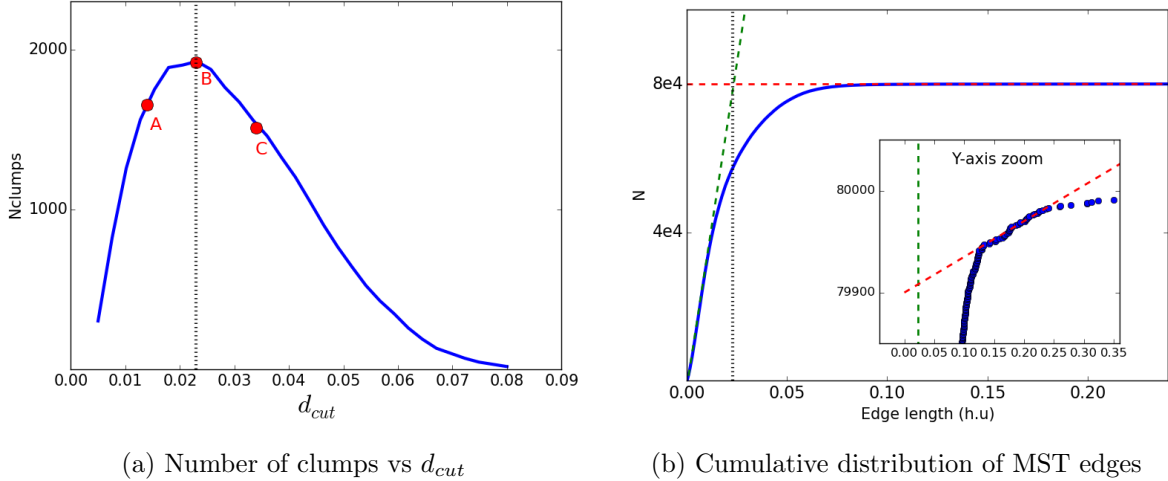


Figure 3.3: Two different methods to identify the critical d_{cut} for clump detection. Both methods give the same value. For this 80k model, the value is 0.024 in Hénon units. The ref linear fit on (b) was made on the linear portion with sufficient data points, discarding the very few further points departing from the tendency.

Table 3.1: Summary of fragmentation models and their characteristics. These simulations started from an uniform sphere and were stopped when the expansion halted, at $t=3$ H.u. . The third column shows the number of independent computations for each model.

Name	N	Sampling	Mass range
Rmh20	15000	30	[0.35- 20]
Rmh100	15000	30	[0.3 - 100]
Rmh1	15000	30	1.0

increasing from top to bottom. For the smallest value $d_{cut}=0.015$ H.u., clumps look somewhat truncated as we are still in the under-sampling regime and only their cores registered as clumps. The second, optimal, value $d_{cut}=0.025$ H.u produces visually well-isolated clumps. Finally, the third and largest value is so that clumps begin to merge together : this is shown by the unique clump identified in the bottom panel (filled blue squares).

3.2 Clump mass function

3.2.1 Influence of stellar mass function

We know the clumps are seeded by density fluctuations in the initial uniform sphere. These fluctuations are governed by pure Poisson noise in the case of identical stellar masses, but are modified and enhanced once stars follow a mass function themselves: a high-mass star surrounded by lighter ones will by itself introduce a localized strong density fluctuation.

We wish to quantify the relation of the clump- to the *stellar* mass function in the generated initial conditions. To this end, we ran a set of simulations where all the stars have the same mass, and two sets for which a Salpeter mass function with $\alpha = 2.35$ was truncated at different upper- and lower-bounds. A total of 15000 stars in a Hubble configuration were used, all let go with the same initial expansion rate $H_o = 1$. For the multi-mass models, the mass range was chosen as $[0.3, 100] M_\odot$ and $[0.35, 20] M_\odot$ so that the mean stellar mass = $1M_\odot$ as for the single-mass models. Thirty different runs were performed in each case and the outcome averaged for better statistics. These are referred to as Rmh1, Rmh100 and Rmh20 in Table 3.1.

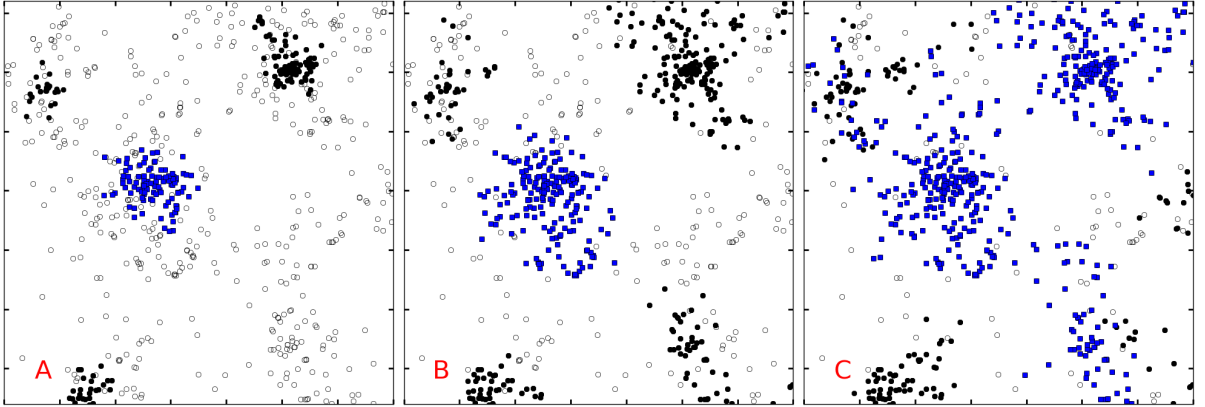


Figure 3.4: Example of detected clumps for three cutting length, 0.014 (top panel), 0.024 (middle panel), 0.034 (bottom panel), which were labeled A,B,C in Fig. 3.3a. A cube within a 80k particles fragmented model was extracted and projected. Empty circles are stars which do not belong to any clump, black circles are clump members, and blue squares are stars that are identified as a single large clump. Tick marks are spaced by 0.05 length units for a box size of 0.35 units.

On Fig. 3.5, we display the number of clumps as function of clump mass for the truncated Salpeter models as a red solid line, while the single stellar mass models are shown in green dash. A grey shade indicates one standard deviation where statistics allow (*i.e.*, large numbers), and we have used bins of constant logarithmic mass intervals. Fig. 3.5a shows Rmh20 models, and 3.5b shows Rmh100 models. With clump membership restricted to $N \geq 12$, the identical-mass model stays close to a power law (straight dotted line on the figure) of index ≈ -3 down to the lowest clump mass of $12M_\odot$. A spread in stellar masses leads to fewer low-mass clumps forming, which profits the more massive ones (we counted $\simeq 100$ clumps of $12M_\odot$ for the equal-mass case ; and ≈ 32 with a mass $\leq 12M_\odot$ for the other ones) . This transforms the clump mass function, from a near-power-law, to a bell-shaped distribution.

When very massive stars are included in the calculations, yet more massive clumps are formed (Fig. 3.5b). The formation of large sub-structures depletes the number of clumps around the peak value, and so the distribution becomes broader and shallower. The mean clump mass for the different cases read $18M_\odot$ (equal-mass), $30M_\odot$ (Salpeter $m_{max} = 20M_\odot$) and $42M_\odot$ (Salpeter $m_{max} = 100M_\odot$), a steady increase with the width of the stellar mass spectrum. On the other hand, the position of the peak of the distribution remains unchanged at (roughly) 20 to $21M_\odot$. The trend in total number of clumps detected is a slight decrease with the broadening of the stellar mass spectrum, from 166, down to 143 respectively for the $m_{max} = 20$ and $100M_\odot$ Salpeter models. We observe that the overall fraction of stars found in clumps (some ≈ 6500 out of 15000, or 43%) stays unchanged.

We argue that the shape of the clump mass spectrum provides indirect evidence for the role of massive stars predominantly as seeds for growth in our simulation, as opposed to the hierarchical build-up of clumps from very tiny sub-structures. There are two tell-tale signs to support this view : a) if high-mass clumps formed through the repeated and stochastic merger of smaller clumps, then the clump mass function should tend to a log-normal distribution, which is symmetric (in logarithmic scales) with respect to the peak value, whereas the distributions shown here lack this basic property ; and b) the ratio of maximum clump mass to mean mass may exceed 15 when the stellar truncation mass is set to $20 M_\odot$, and reaches only ~ 4 in the case when the upper mass is set to $100 M_\odot$. If small-ish clumps were merging at the same rate in both models, then this ratio should be comparable. Instead, very large clumps take too long to assemble and the merger rate drops with clump mass. Recall that all fragmentation calculations

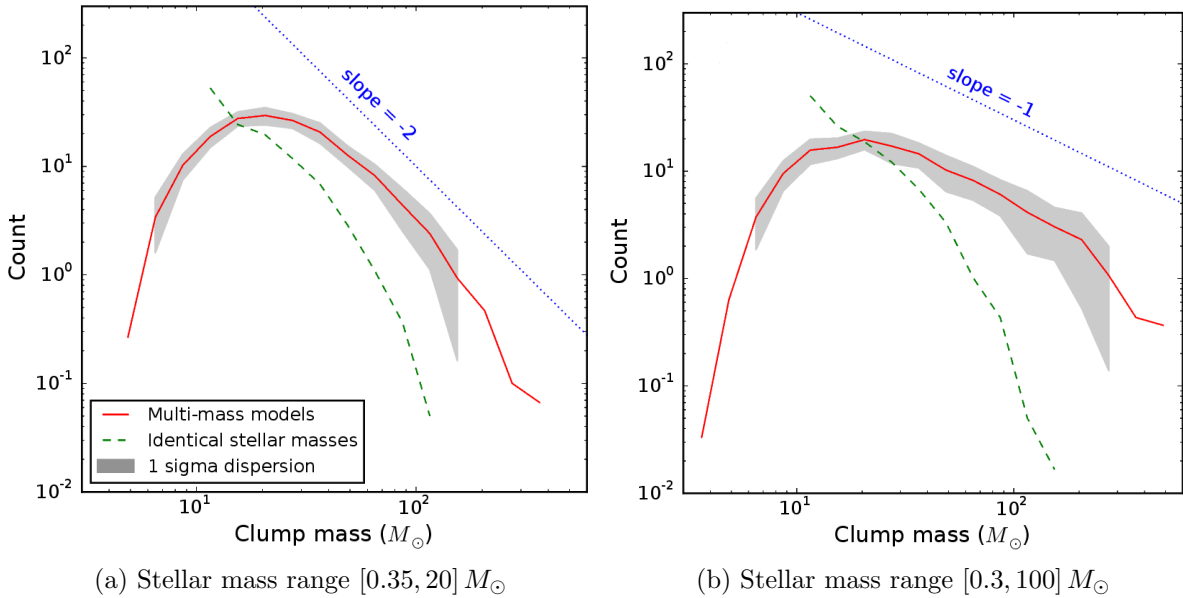


Figure 3.5: Mass function of the clumps identified with the MST algorithm. The calculations all had $N = 15000$ stars, and we have averaged over 30 realisations for each configuration. The results for three stellar mass functions are displayed : a model with equal-mass stars (green dashed line) ; a Salpeter distribution function truncated at $20M_{\odot}$ (solid red line, left) ; a Salpeter distribution function truncated at $100M_{\odot}$ (solid red line, right). (a) The clumps mass function for equal-mass models shows a trend with mass roughly in agreement with an M^{-3} power-law. By comparison, the results for an Salpeter stellar distribution function truncated at $20M_{\odot}$ has a bell-shaped profile, with a peak around $M = 20.5M_{\odot}$; only the tail-end shows marginal agreement with an $\propto M^{-2}$ power-law (dotted line on the figure) ; (b) another Salpeter distribution function but with the upper-mass truncation set at $100M_{\odot}$. The tail at large clump mass is now much flatter, with a slope $\approx M^{-1}$, (dotted line on the figure as well). The bins used had constant logarithmic mass intervals.

ran for the same total time.

To check whether massive stars act as seeds in the simulation, we borrow from black hole dynamics in galactic nuclei the notion of a *radius of influence*, which is the radius enclosing as much mass in the stars as the central black hole mass (see e.g. Merritt 2013). Here, the stars inside the influence radius are bound to the massive star at the centre. Thus if a massive star is a seed for a clump, and only the stars inside the influence radius remain bound to it, we should count as many clumps in the mass range $2m_*, 2m_* + 2dm_*$, as there are stars in the range $m_*, m_* + dm_*$. Because the maximum clump mass exceeds twice that of the most massive stars m_{max} , some degree of merging must take place. If we count all clumps starting from the truncation value m_{max} of the stellar mass function, then we should find as many clumps in the mass range above m_{max} , as there are stars in the interval $[m_{max}/2, m_{max}]$. We find for runs with $m_{max} = 20M_\odot$ some 93 clumps more massive than that, when there are $\simeq 100$ stars in the range $[10, 20]M_\odot$, essentially identical ; and some 11 clumps of $100M_\odot$ or more, when there are (on average) 9 stars in the mass range $[50, 100]M_\odot$. This calculation suggests that most massive stars act as seeds for the formation of large clumps in the generated initial conditions.

3.2.2 Influence of H and N

Now that we know how the stellar mass function affects the seeding of the clumps, we can look at the influence of H_0 and N on the subsequent fragmentation and clump growth. H_0 tunes the strength of the expansion, which tunes the duration of the fragmentation. A stronger initial expansion allows for more time for clumps to grow, so we expect more massive clumps with increasing H_0 . On the other hand, a higher N only sample more stars from the same stellar mass function, and the density fluctuations should not change in nature, just scale down with the average distance between stars, we do not expect N to significantly affect the fragmentation. To verify these, a set of simulation was performed to explore the mass function of clumps in the H_0 - N parameter space. The models have 5 different memberships that go as powers of 2 in thousands, with an increasing sampling to obtain acceptable statistics:

N	1000	2000	4000	8000	16000
Sampling	12	8	5	5	5

Each one of these models were performed with 5 different H_0 :

$$H_0 | 0.8 \quad 0.9 \quad 1.0 \quad 1.1 \quad 1.2$$

for a total of 175 different models ran up to the end of the expansion. The stars are taken from a Salpeter mass function with a $[0.3, 100]M_\odot$ mass range. Before going into the clump mass function analysis, we use this set of models to compare our analytical expectation of the apex time as a function of H_0 shown on Fig 2.1. For each model, we follow the evolution of the half-mass radius, then take the apex time as the maximum radius time, when the cluster stops expanding and starts collapsing.

We show on Fig 3.6 the expected analytical curve as a dashed line, then the numerically obtained apex times from out different H_0 and memberships, averaged over all similar runs. The 16k runs follow the analytical expectation within 5%, while lower membership models take more time than expected to stop expanding at high H_0 , overshooting by as much as 30% for $H_0 = 1.2$. Visual inspection of the runs showed that low memberships were more susceptible to have a clump "take over" during the expansion. As we will show in the present section, low- N clusters contains more massive clumps in relative mass than high- N models. When a massive enough clump form during the expansion, it offsets the effective center of the cluster and skews the half-mass radius (computed from the barycenter of the full system) to higher values, offsetting its fall from the collapse. To reduce unwanted "sur-fragmentation" effect, we use analytical apex times to select our fragmented configurations.

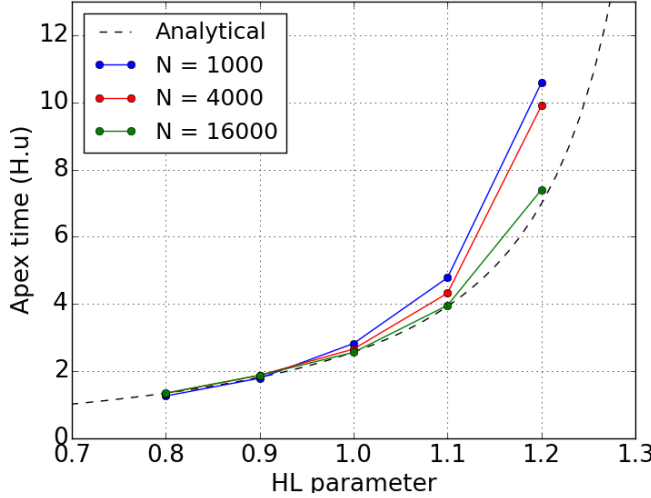


Figure 3.6: Clump mass function (real mass) for several H_0 and two memberships.

The clump-finding algorithm was ran on the fragmented models to obtain the clump mass function. The results are summarised on figures 3.7 and 3.8. As for the previous section, note that the number counts gets down to fractional values due to the averaging procedure.

The shape of the mass function is consistent with what was seen in previous section. Looking at the top panels of Fig 3.7, we see the mass function of clumps in *relative* mass, the percentage of total mass they contain. Clumps in small-N systems tends to contain a much larger portion of the total system mass than in large-N systems, which is even clearer in the normalized count sub-panels. In fact, for $H_0 = 0.8$, the peak of the mass function for $N=1k$ happens at 1.1% of total mass, while for $N=16k$, it happens at 0.07%. These values ratio gives ~ 16 , the membership ratio: the clumps relative masses appears inversely proportional to the model's membership.

This can be interpreted as a underlying common clump distribution in physical mass, regardless of the total membership of the model. Such hypothesis is confirmed by looking at the bottom panels of Fig 3.7, in which clump distribution are plotted in physical mass, once the masses of stars have been rescaled from Hénon units to match the stellar original mass function. Looking at the normalized count subpanels, it is clear that 1k and 16k models have the same clump distribution, when raw count subpanel show clumps are expectedly more numerous in high-N models. The difference between $H_0 = 0.8$ and 1.2 is not clear from the graph, but it seems a higher H_0 pushes the upper limit of the distribution to slightly higher masses.

To illustrate this last trend, we turn to Fig 3.8 where clump MF are shown for various H_0 and a common membership. For both $N=1k$ and $N=16k$, the distribution preserves its shape for various H_0 , and gets prolonged at higher clump masses for $N=16k$, as more mass is available to build clumps.

Thought the distribution does not undergo any dramatic change, a weak trend with H_0 is seen in both panels: as the strength of expansion increases, the distribution slightly decreases at low clump masses and slightly increases at higher clump masses, the pivot masses being $\sim 30 M_\odot$. We look at the 16k model and follow the cumulated mass inside all clumps, as well as the percentage of this mass in clumps below and above $30 M_\odot$, for different H_0 :

H_0	0.8	0.9	1.0	1.1	1.2
M_{tot}	3502	3478	3582	3683	3561
$< 30 M_\odot (\%)$	66	65	55	49	44
$> 30 M_\odot (\%)$	34	35	45	51	56

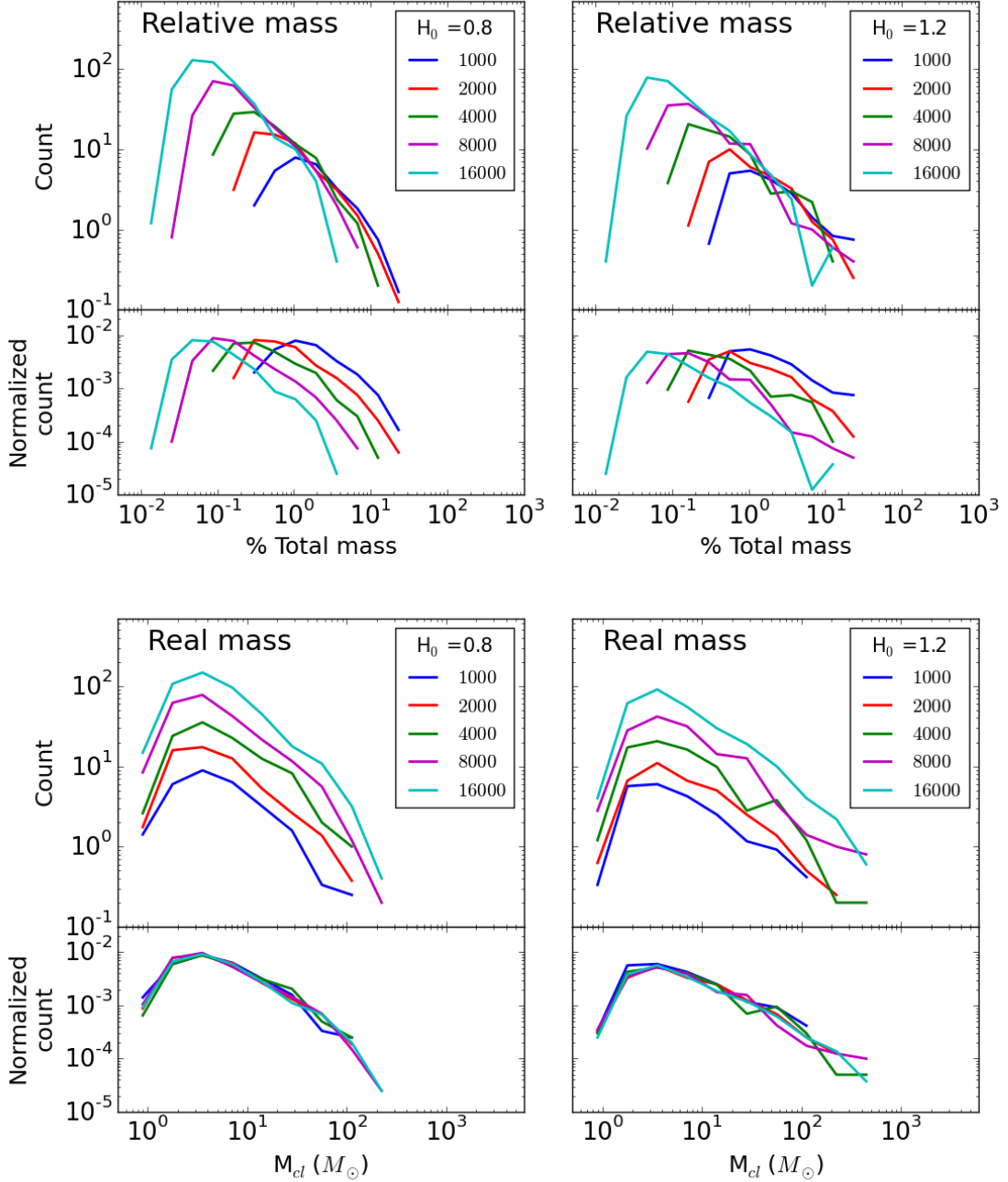


Figure 3.7: Clump mass function for several memberships and two H_0 . Masses in the top panels are in Hénon units, the x-axis was scaled with a factor 100 to get a percentage of the total mass of the system. Bottom panel masses are in physical units. In each panel, top sub-panel shows actual clump count in each bin (averaged over sampling), while bottom sub-panel normalize the count by the model membership.

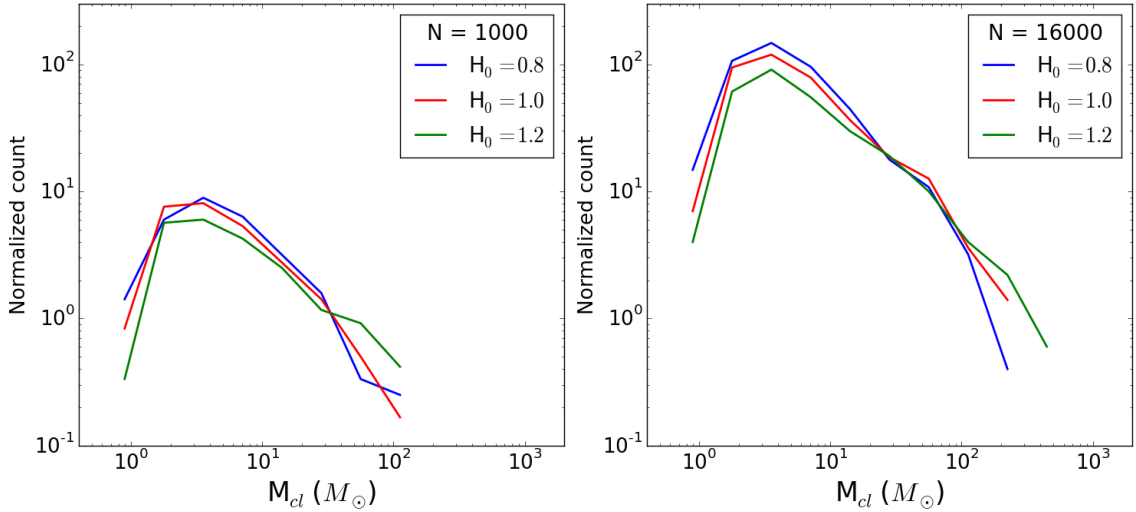


Figure 3.8: Clump mass function (real mass) for several H_0 and two memberships.

From this data, we get two facts about our fragmented models: the mass contained in clumps does not depend on H_0 (<2% dispersion) and there is a transfer of mass from small clumps to more massive ones as the expansion lasts longer.

To summarise: the general shape of the clump mass function is common to all membership and H_0 . In physical mass, the same clumps form in 1k and 16k models, almost regardless of the duration of the expansion. We note a mass transfer from small to high mass clumps when H_0 increases, that is consistent with a merging process: small clumps assemble or get accreted by large clumps. When the initial expansion is strong, the merging lasts longer and more mass is transferred. This is confirmed by visual inspection of the models, as we see clumps merging during the expansion.

3.3 Clump contents

In this section we compare the clump configurations derived from the Hubble-Lemaître expansion method with the distribution of proto-stars that form in hydrodynamical simulations. We first look at the velocity field inside and outside the clumps, then we investigate the stellar content of the clumps themselves and their mass segregation. We performed additional simulations to investigate higher memberships, summarized below:

Name	N	Sampling	Mass range
R40h20	40000	1	[0.35- 20]
R40h100	40000	1	[0.3 - 100]
R80h100	80000	1	[0.3 - 100]

3.3.1 The velocity field

There is no hydrodynamics in the approach that we have taken, nevertheless expansion under gravity alone is equivalent to the adiabatic expansion of gas : for that case, the first law of thermodynamics equates the drop in internal energy dU to minus the external work, $-pdV$. At constant mass, the change in gravitational energy dW is $-dE_k$, where E_k is the kinetic energy. With $W < 0$ but increasing over time, this implies that E_k drops in amplitude. In the case when the motion is strictly radial, $E_k = 0$ when $H = 0$ and all stars come to rest. We ask to

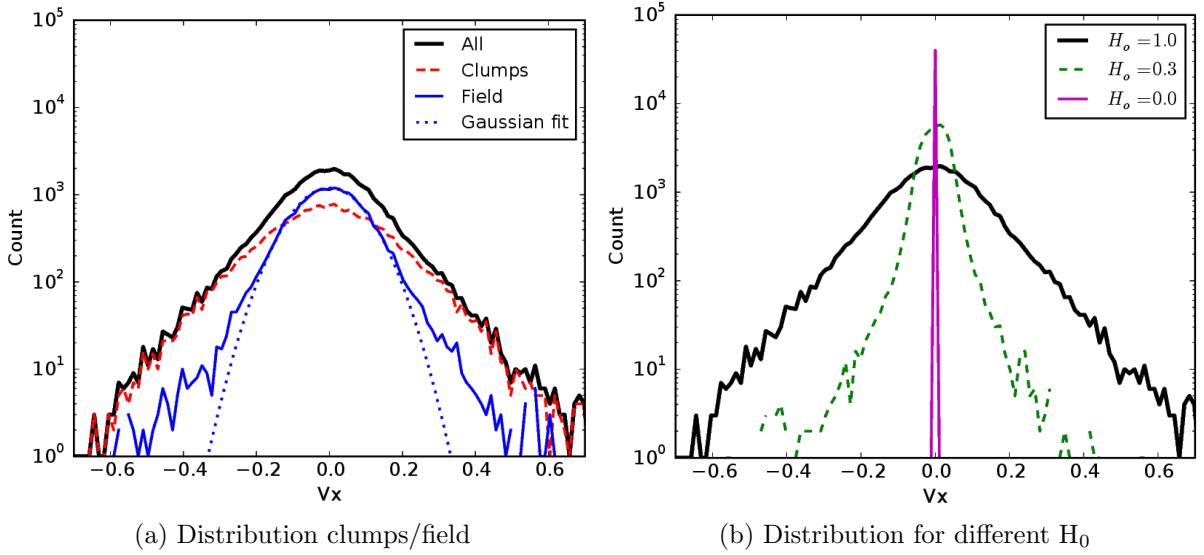


Figure 3.9: (a) Distribution of the one-dimensional velocity field for the whole cluster as the thick solid black line, in the simulation labelled as R40h20 at the apex time ($H = 0$). The red dashed distribution matches clump members and thin solid blue the field particles. (b) The distribution for three different values of H_0 : when $H_0 = 0$, the distribution is a Dirac- δ around $v = 0$. The central distribution broadens as H_0 increases to 0.3 and 1. Observe the exponential profiles at large $|v|$. Velocities are in $H.u$

what extent the growth of substructures and non-radial motion off-set the ‘adiabatic cooling’ brought on by expansion.

Fig. 3.9a graphs the x-axis one-dimensional velocity distribution for a 40k-particle model. The left-hand panel displays the overall distribution as well as the two sub-populations of clump members and out-of-clump *field* stars. We identified some 20944 stars in clumps (or $\approx 52\%$) at the end of expansion. The expectation that all stars have zero- or low-velocities is validated by the peak in the distribution around $v_x = 0$.

As sub-structures form and interact mutually, generating tangential as well as radial motion, the peak broadens but remains symmetric about the origin. The large velocities are brought by stars in clumps, which demonstrates that interactions within the substructures boost the internal velocity dispersion of the cluster as a whole. Field stars dominate the low-amplitude regime. Their velocity distribution is well-fitted with a Gaussian (shown as a dotted blue line), down to one-tenth the height of the central peak, or about 1% of all field stars.

To illustrate further the idea that large velocities are confined to clumps formed by fragmentation modes, we compare on Fig. 3.9b a set of models with different initial values of H_0 : 0, 0.3, and 1. Clearly when $H_0 = 0$, the velocities are identically zero and there is no fragmentation whatsoever (apart from root-N noise). The distribution is then a sharp peak centered on zero. For positive but low values of H_0 , the fragmentation modes do not develop much before the apex and the (non-radial) velocities remain small. The central peak has a much narrower dispersion, and the high-velocity wings are clipped. In this case, too, analysis of the weakly fragmented system shows that virtually all high-velocity stars are found in clumps. The velocity distribution for the case $H_0 = 1$ is added for comparison. The fact that the full range in velocities is reduced by a factor ~ 3 for the less fragmented model is also an indication of the shallower potential well of the clumps

The full population velocity distribution (solid black line) at first sight is very similar to those of Klessen & Burkert (2000, Fig. 5). In that figure, the authors show the velocity distribution of gas particles in a fragmenting system. Klessen & Burkert attribute the high-velocity tails to gas particles falling towards stellar clumps at supersonic speed. Supersonic motions imply that

gas particles trace ballistic trajectories, and hence behave like point mass particles.

A small fraction of field stars in our calculations also have large velocities. We suspected that these stars might have acquired their large velocity through in-fall toward a nearby stellar clump. We did not, however, find compelling evidence that would allow us to identify the origin of high velocities in field stars. Inspection of a sequence of snapshots failed to show that the velocity vectors were pointing at nearby stellar clumps: it is therefore not possible to make the same assertion as [Klessen & Burkert](#) and state that stellar clumps accrete field stars.

It is possible, on the other hand, that high velocities originate from past star-star interactions. However, we did not find clear trends in the few orbits that we studied which would confirm such an event. The question of mass accretion by stellar clumps might be best settled if we added gas to our simulations to boost the mass resolution, and analysed model data using mock CCD frames, as did [Klessen & Burkert](#). This was not attempted here.

We close this section with a remark about the velocity distributions seen on Fig. 3.9 and the internal state of the stellar clumps. Because small clumps would have time to evolve dynamically through star-star collisions and reach a state of near-equilibrium (see §2.2.4) we would expect clumps to develop a velocity field similar to Mitchie-King models of relaxed self-gravitating star clusters ([Binney & Tremaine, 2008](#)). The one-dimensional velocity distribution of Mitchie-King models plotted in a logarithmic scale approaches a flat-top when $|v_{1d}|$ is small, and cuts-off rapidly at large values : the distributions are concave at all velocities. This holds true for all models independently of their King parameter¹ W_0 .

The shape of the distributions displayed on Fig. 3.9, on the other hand, is convex as we shift, from small, to large $|v_{1d}|$. We deduce from this straightforward observation that the clumps that formed through fragmentation and subsequent mergers cannot be treated as fully in isolation and in dynamical equilibrium à la Mitchie-King. Fragmentation in hydrodynamical calculations often proceeds from filaments and knots (e.g., [Klessen & Burkert 2001](#); [Mac Low & Klessen 2004](#); [Maschberger et al. 2010](#); [Bate, Tricco & Price 2014](#)). The clumps that form in a fragmenting Hubble flow are also surrounded by filaments and other structures which perturb them.

3.3.2 The stellar mass function in clumps

To complete the analysis, we show on Fig. 3.10 the mass function of stars both in clumps and in the whole cluster. For brevity, we only show a model with a mass function truncated at $20M_\odot$, however our conclusions are not sensitive to the truncation value. The mass function of ≈ 6400 stars that were found in clumps (some 43%) is displayed as the red solid curve. The theoretical Salpeter distribution function for the same number of stars is shown in black dots, with grey shades giving the 1σ dispersion from multiple samplings. Finally, the green dashed curve shows the mass distribution of all 15 000 stars in the model. The lower panel is the same data normalised to the Salpeter data.

The uptake in massive stars for the whole population (green dashed line) of both clumps members and field stars is a statistical artefact and lie within the standard deviation of a Salpeter distribution with comparable sampling number.

The clump member population clearly deviates from a Salpeter distribution in two ways : first we note a deficit of low mass stars with respect to the field population (shown as the green dash) ; secondly, although a Salpeter mass function is more or less consistent with the population up to $M \approx 2M_\odot$ (black dotted line) the distribution shows a clear excess of massive stars. We find that practically all the stars more massive than $10M_\odot$ ended up in a clump (this is the point where the solid red curve joins the dash green one).

A linear regression fit of the clump members mass function gives a power-law index of -2.15 ± 0.02 , shallower than the Salpeter index of -2.35. Applying the same analysis to field stars, we find a steeper mass function of index -2.46 ± 0.02 . The difference of ≈ 0.3 between the

¹Notice how this holds only because of the choice of a logarithmic vertical axis.

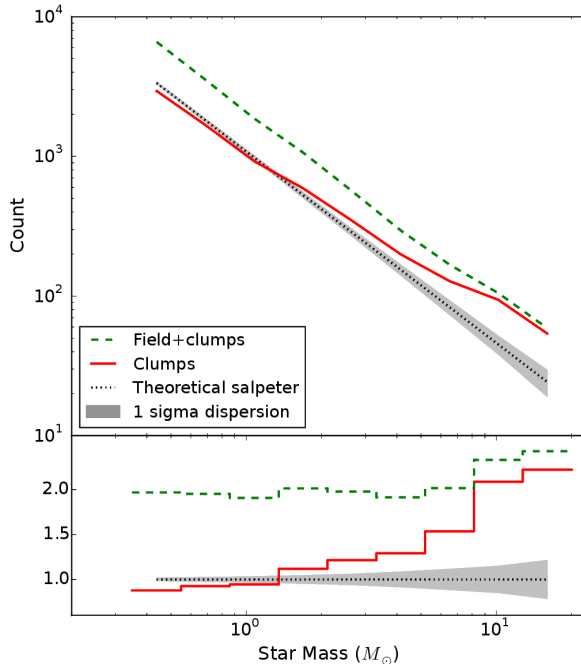


Figure 3.10: Top panel : Mass function of all stars belonging to a detected clump (solid red). The expectation drawn from a Salpeter distribution function for the same total number of stars in dotted black ; the grey shade are 1σ uncertainties. The green dashed line is the distribution for the full cluster. Bottom panel : same data normalised to the Salpeter expectation.

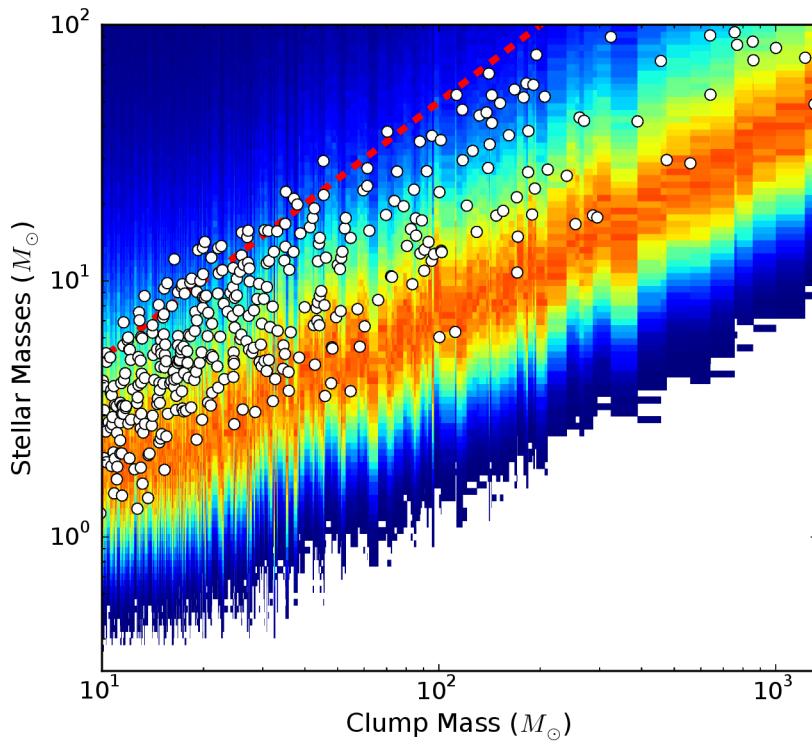
two populations is very similar to what is found in the Milky Way disc (see e.g. [Czekaj et al. 2014](#); [Rybicki & Just 2015](#); [Bastian, Covey & Meyer 2010](#))

[Bonnell, Vine & Bate \(2004\)](#) and [Maschberger et al. \(2010\)](#) showed from inspection of hydrodynamical simulations that massive stars play a key role in the assembling process of clumps, attracting already formed protostars to them. We find a similar general trend in Hubble-fragmented gas-free simulations: clumps develop around massive stars so that their stellar mass function is top-heavy.

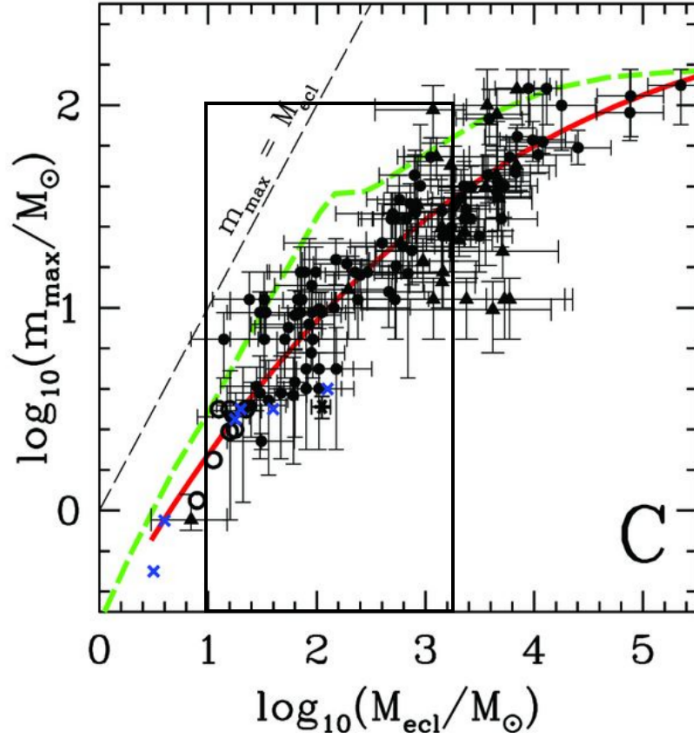
This excess can also be seen in the top panel of Fig. 3.11a in which for each of 440 clumps, we show as white dots the mass of their heaviest star as a function of the host clump's mass. These data were obtained from the R40h100 run. For comparison, we sampled a Salpeter mass function, drawing the same number of stars as found in each clump. We then identify the most massive star in the Salpeter sample ; the procedure was repeated 15000 times *for each clump* to obtain suitable statistics. The grey shades (color levels in the electronic version) shows the resulting distribution.

In a nutshell, Fig. 3.11a shows for each clump the likelihood that their most massive stars may be drawn from a Salpeter function, one could call the red, maximum likelihood zone the "Salpeter valley". Only clumps with a mass $> 10M_\odot$ are included to account for a possible bias when clump membership reaches below $N_d = 12$ stars. It can be seen on the figure that the scatter of white dots tends to lie systematically above the Salpeter valley. If we add the relation $m_{clump} = 2 \max\{m_\star\}$ (cf. section 3.2.1), we find some overlap with the data (see the red dashed line on Fig. 3.11a). This clearly illustrates the tendency for massive stars to act as seeds when the clump form, while the scatter is driven by the merger and accretion history of individual clumps.

The correlation displayed on Fig. 3.11a is in good agreement with observational data for young embedded clusters of the same mass range published by [Weidner, Kroupa & Pflamm-Altenburg 2013](#). We reproduced their figure on Fig. 3.11b with a black frame representing the



(a) Distribution clumps/field



(b) Distribution for different H_0

Figure 3.11: (a) Mass of the heavier star in each clump, shown as white dots, as a function of clump mass. The color map shows the likelihood for the maximum mass if all clump members were sampled from a Salpeter IMF ; the orange crest gives the maximum likelihood. The red dashed line shows the relation $m_{\text{clump}} = 2m_{\text{max}}$ (see. section 3.2.1). The data was taken from the R40h100 run. (b) is a similar distribution from [Weidner, Kroupa & Pflamm-Altenburg \(2013\)](#), built with data about young embedded star clusters from [Weidner, Kroupa & Bonnell \(2010\)](#). The black frame notes the range of masses displayed in (a).

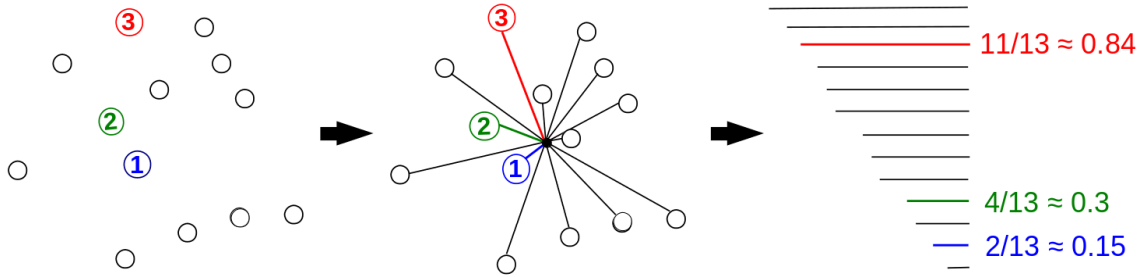


Figure 3.12: Illustration of the radial ranking method. Stars marked 1,2 and 3 are the first, second and third most massive stars in the clump. Distances to the geometrical center are computed then sorted. The position in the sorted list is converted to a number, the radial rank.

range shown on Fig. 3.11a.

Note how the *scatter* in the correlation brought on by the dynamical processes at play during the adiabatic fragmentation phase also compares well with the data. Thus the stellar clumps modelled here recover an important characteristic of observed embedded young clusters.

3.3.3 Mass segregation

In this section, we ask whether the clump assembling process at play in our simulations accounts for the mass segregation measured in star-forming cores in hydrodynamical simulations. The measure of mass segregation of Olczak, Spurzem & Henning (2011) based on the MST, while efficient, will give noisy results for very small- N clumps. Instead, we follow Maschberger et al. (2010) and rank clump members according to their distance to the geometric centre of a clump, which is calculated by number-averaging (so this centre is not the clump barycentre). We then sort the bodies by mass and tabulate the radial rank of the three most massive ones. This process is illustrated on Fig 3.12.

The great advantage of this approach is that it is independent of geometry and absolute size once the ranking is normalised to the clump membership N_c . One issue arises with the binning of the rank, since small values of N_c give large intervals by construction, and conversely for populous clumps : we found a good compromise by setting the width of each bin to $1/20$ since the mean clump mass $\sim 20M_\odot$ implies $N_c \sim 20$ on average. The procedure is repeated over all clumps identified in the run (typically on the order of ~ 200). The diagnostic for an un-biased sampling is a profile with radius that remains the same regardless of the mass selected ; if, furthermore, the stars are (on the mean) un-segregated in radius, then the profiles will be flat.

Fig. 3.13 graphs the distribution of rank of the three most massive stars in all the clumps from R40h100 fragmented state. The salient features are that 1) none of the distributions are flat, all three peaking significantly at small ranks ; and 2) there is a clear trend for the most massive star also to be the most segregated. Precisely this result had to be expected from the internal dynamics of small clumps (cf. section 2.2.4). Our Fig. 3.13 should be compared with Fig. 13 of Maschberger et al. (2010): the authors also found radial rank distribution to peak at small values for massive stars, showing a level of mass-segregation in their clumps.

It is striking that the measure of mass segregation attained here for a gas-free configuration is a good match to a full hydrodynamical setup. By implication the segregation proceeds more vigorously once the proto-stellar cores have condensed and behave essentially like point sources. The initial configuration that we have adopted relies only on density fluctuations to seed clumps, however once again we find evidence that massive stars begin and remain the centre of gravitational focus for clump formation. That is not so when clumps are setup using a fractal approach

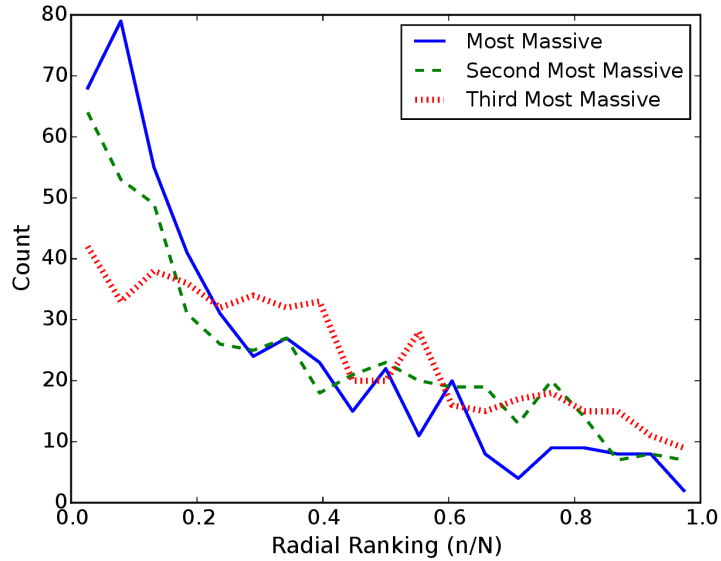


Figure 3.13: Histograms of radial ranking of first, second and third most massive star in each clump for a model with $N = 40\,000$ stars (R40h100).

(Goodwin & Whitworth, 2004; Allison et al., 2009a). There is then no segregation initially, and it all develops at or shortly prior to the global system evolution towards equilibrium (the collapsing violent relaxation phase).

3.4 Concluding remarks

In the next section we follow through with the final stage of evolution towards equilibrium and compare the final configuration with those of Allison et al. (2009a) and the recent study by Caputo, de Vries & Portegies Zwart (2014).

CHAPTER 4

Collapse and dynamical evolution

4.1 The simulations

4.1.1 Description of the models

The Hubble-Lemaître fragmented system is subvirial by construction. The configuration we took as a reference is the apex of the expansion: the kinetic energy initially injected in the expansion has been converted into potential energy through expansion or converted to transversal motion by two-body interaction. If the model is left to evolve further, it collapses, violently relaxing to reach a quasi-equilibrium state, resembling a Plummer or King model.

In the present chapter, simulations will use the fully fragmented state of Hubble models as initial conditions for the subsequent dynamical evolution. Observational clues point to collapsing and violently relaxing clusters. For example, [Cottaar et al. \(2015\)](#) find IC348, a young (2-6 Myr) cluster, to be both survirial and with a convergent velocity field, consistent with infalling motion. Our models undergo dry collapse with no gas, while real objects such as IC348 still contain residual gas. The scenario of our simulations is an idealized situation: clearly if there was residual gas between the clumps and it was evacuated through stellar feedback, both the clump merger rate and the depth of the potential achieved during relaxation would be affected. As a limiting case, rapid gas removal may lead to total dissolution (see for instance [Moeckel et al. 2012](#) and [Fujii & Portegies Zwart 2016](#)). In the current situation, all clumps will merge.

The numerical integration were done once more with the Nbody6 integrator with the same computational units. For comparison purposes, we also performed simulations of cold uniform sphere, a configuration which has been extensively used in the past (e.g.,[Theis & Spurzem 1999](#); [Boily, Athanassoula & Kroupa 2002](#); [Barnes, Lanzel & Williams 2009](#); [Caputo, de Vries & Portegies Zwart 2014](#); [Benhaiem & Sylos Labini 2015](#)) and one that minimises the level of fragmentation and mass segregation in the on-set of collapse. Table 4.1 lists the simulations performed. We focus here on models with a mass function from $0.35M_{\odot}$ to $20M_{\odot}$ and 15000 stars, a compromise value for rich open clusters that should allow us to identify clearly collisional

Table 4.1: Summary of collapse simulations and their characteristics. These simulations started from a subvirial state: cold uniform sphere or fully fragmented Hubble model; each were evolved up to $t = 40$ H.u

Name	N	Mass range	Model
Rh100	15000	[0.3 - 100]	Hubble
Rh20	15000	[0.35- 20]	Hubble
Ru100	15000	[0.3 - 100]	Uniform
Ru20	15000	[0.35- 20]	Uniform

effects and trends with time, and ease comparison with the recent study by Caputo, de Vries & Portegies Zwart (2014) where most calculations are performed with that sampling. We let both Hubble-fragmented- and uniform sphere evolve up to 40 H.u.

4.1.2 Scaling to physical units

Before discussing the results, it is useful to translate the units of computation to physical scales. This is important if we want to discuss the state of the systems using one and the same physical time, such that the hypothesis of no stellar evolution holds good. To do so, we compute the free-fall time of an uniform sphere (a good approximation for fragmented model as well) both in physical units and Hénon units, which provide a conversion factor. We first have to choose an initial physical length scale for the system by setting $R_h = 1$ pc. With a total system mass of $M = 15 \times 10^3 M_\odot$, this gives a half-mass volume density

$$\rho_h = \frac{M/2}{\frac{4}{3}\pi r_h^3} \simeq 10^3 M_\odot/pc^3, \quad (4.1)$$

well within values typically inferred from observations.

The free-fall time of an uniform sphere, obtained from conservation of energy and integration, is expressed:

$$t_{ff} = \sqrt{\frac{3\pi}{32G\rho_0}} \quad (4.2)$$

Computing $\rho_{h,\text{Hénon}} \simeq 0.13$, we can now compute both values of the free-fall time:

$$t_{ff} \simeq 1.5 t_{\text{Hénon}} \quad (4.3)$$

$$\simeq 0.25 \text{ Myr} \quad (4.4)$$

Which gives:

$$1 t_{\text{Hénon}} \equiv 0.16 \text{ Myr} = 1.6 \times 10^5 \text{ yr} \quad (4.5)$$

Thus by running up to 40 H.u we ensure that the systems evolve for at least 15 crossing times and $\sim 5 \times 10^6$ years, about the lifetime of a $50M_\odot$ star.¹

We now want to evaluate the crossing and relaxation timescales in such a system, as they were defined in the introduction (1.2.2), and how they relate to the total duration of the simulation. We could attempt to derive a crossing time for the initial, subvirial state but it would not be representative of the evolution of the system. Instead, the more useful crossing time has to be computed from the equilibrium state achieved. Using the virial theorem and conservation of energy, we can derive dynamical timescales for the equilibrium system. From the definition, the crossing times is defined:

$$t_{cr,eq} = \frac{2R_{h,eq}}{\sigma_{1d,eq}} \quad (4.6)$$

From here on, initial values are noted with the subscript 0 and equilibrium values by the absence of subscript. To obtain both R_h and σ_{1d} we start from the total energy of the system. At $t=0$, velocities are null, all energy is potential energy. It can be computed by integrating from the center to R_0 . We obtain

$$E_0 = -\frac{3}{5} \frac{GM^2}{R_0}. \quad (4.7)$$

From virial theorem and conservation of energy, we get the following equations at equilibrium

$$\begin{cases} 2E_k + E_p = 0 \\ E_k + E_p = E_0 \end{cases} \implies \begin{cases} E_k = -E_0 = \frac{3}{5} \frac{GM^2}{R_0} \\ E_p = 2E_0 = -\frac{6}{5} \frac{GM^2}{R_0} \end{cases} \quad (4.8)$$

¹For our models with more massive stars, up to $100M_\odot$, these represent only $\sim 5\%$ of the total mass and their removal would not significantly alter the dynamics of the system.

which can be combined with

$$E_k = \frac{1}{2}M\sigma_{3d}^2 = \frac{1}{2}M(3\sigma_{1d})^2 = \frac{9}{2}M\sigma_{1d}^2 \quad (4.9)$$

to get

$$\sigma_{1d} = \sqrt{\frac{2GM}{15R_0}}. \quad (4.10)$$

As for the half-mass radius at equilibrium, its value is dependant on how concentrated the system is and is not easy to derive. Instead, we replace in Eq. (4.6) the half-mass radius by the virial radius R_v , defined as:

$$E_p = -\frac{GM^2}{2R_v} \quad (4.11)$$

which value should not depart significantly from the half-mass radius and provides an useful approximation. Combining Eq. (4.8) and Eq. (4.11) it comes

$$R_v = \frac{5}{12}R_0. \quad (4.12)$$

We can now write a good approximation of the crossing time in the relaxed, equilibrium system

$$t_{cr} \simeq 2.28 \frac{R_0^{3/2}}{\sqrt{GM}} \quad (4.13)$$

$$\simeq 2.28 t_{\text{H\'enon}} \quad (4.14)$$

$$\simeq 0.35 \text{ Myr} \quad (4.15)$$

With $N = 15000$ we find from (1.6) a two-body relaxation timescale

$$t_{rel} \simeq 270 t_{\text{H\'enon}} \quad (4.16)$$

$$\simeq 42 \text{ Myr} \quad (4.17)$$

and from (1.10), considering a mass range of $m_{max}/\langle m \rangle = 20$, we find a mass-segregation timescale

$$t_{ms} \simeq 14 t_{\text{H\'enon}} \quad (4.18)$$

$$\simeq 2 \text{ Myr} \quad (4.19)$$

Our simulations last for far less than a relaxation time, but we can expect to see some mass segregation set in in our models.

4.1.3 Removal of the ejected stars

The previous section considered there was no mass loss during the collapse and relaxation that leads to the equilibrium system. However, a look at the simulations shows this assumption does not hold. A part of the stars are ejected from the system after the collapse, when the system bounces. These stars are not part of the equilibrium system as they have no influence on the central dynamics.

To understand better the evolution of the central, bound system only, we need to isolate and subtract the ejected stars. The obvious way to do this would be to compute the stars mechanical energy and to remove all stars with positive energy. Though this works for a majority of the

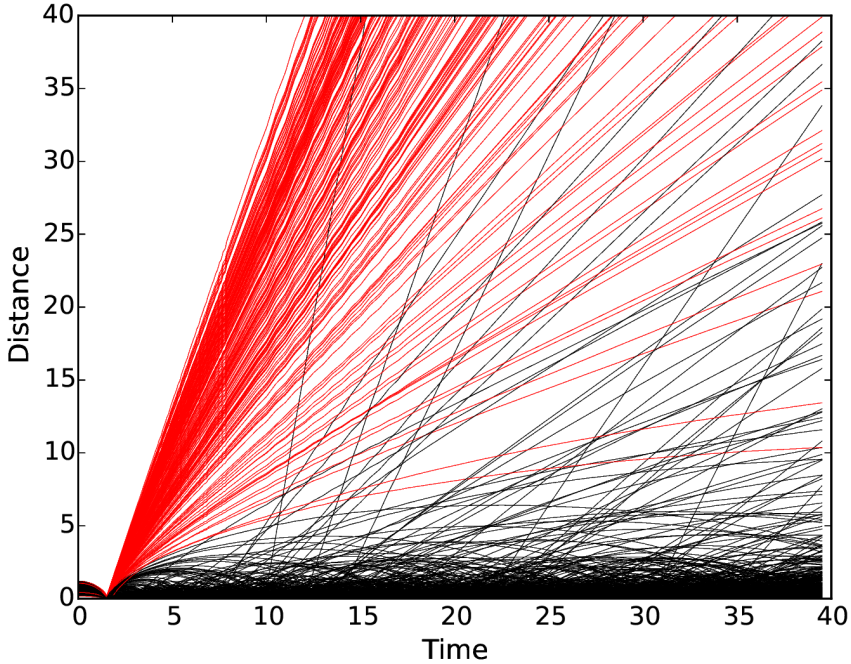


Figure 4.1: Distance to origin for 750 stars from run Ru20 (see Table 4.1). Red lines show the trajectory of stars that are considered ejected according to our criterion.

Table 4.2: Number of initially ejected stars in two collapse calculations

Run	Ejected stars	Ejected mass
Ru20	4227	27%
Rh20	1932	12%

ejected stars, a subset of them has a marginally negative energy. These register as bound when they are essentially out of the system (far beyond the original system radius).

To collect a maximum number of ejected stars efficiently, we spotted the time when the potential energy is maximum, when the collapse occurs. We then identified all stars whose distance to the center increased monotonically from there onwards. The full selection criteria is therefore :

$$v_r(t) > 0, \forall t > t_{ff} \quad \text{or} \quad E_\star > 0, \forall t > t_{ff} \quad (4.20)$$

This allows a more complete selection of the ejecta. On Fig. 4.1 we graph $|\mathbf{r}|$ as a function of time for a subset of escapers (shown as red curves) for the uniform collapse model Ru20. The black curves are trajectories for bound stars given for comparison. Some of these bound stars are later ejected from the system due to two-body interactions, as seen on the figure.

4.2 Collapse and virialisation

The constant diffusion of kinetic energy by two-body interaction means that no stellar system ever reaches a steady equilibrium. However we can contrast the time-evolution of two configurations and draw conclusions about their observable properties.

With this in mind we turn to Fig. ?? in which we show the evolution of the half-mass radius for the cold uniform model (labeled Ru20 ; thick red curve), and the Hubble model (labeled Rh20 ; thin blue curve). Both systems have the same bounding radius initially, contract to a

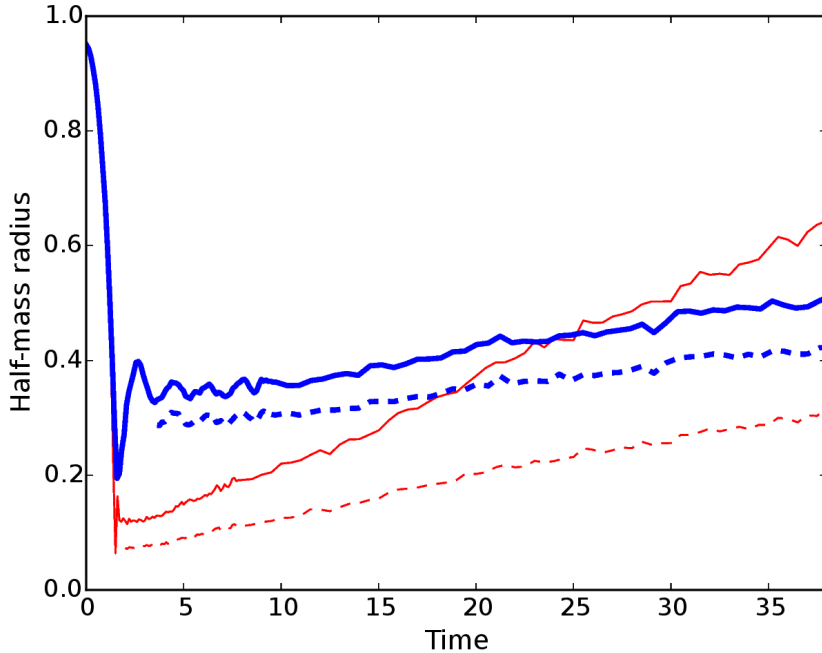


Figure 4.2: Half-mass radius as function of time for two systems undergoing collapse : a uniform-density sphere (thin red solid curve) and a clumpy Hubble model (thick blue solid curve). Half-mass radii are in H.u, as well as the time axis, where $t_{Henon} = 1\text{unit} = 0.270 \times 10^5$ years. Dashed lines are the half-mass radii of the same systems for the same systems but including only the bound stars.

small radius when $t \simeq 1.4$ units and then rebound at time $t \simeq 2$ units. When all the stars are included in the calculation for r_h , we find that the radius increases at near-constant speed after the collapse. That trend does not appear to be slowing down which indicates that a fraction of the stars are escaping. The first batch of escapers is driven by the violent relaxation, however the trend continues beyond $t = 14$ units, corresponding to $t > t_{ms}$ which implies two-body scattering and effective energy exchange between the stars. Note how the uniform model has a much deeper collapse and rebounds much more violently, shedding a fraction twice as large of its stars (Table 4.2). The half-mass radius R_h increases steadily in both models, from the bounce at $t \approx 2$, until the end of the simulation (values in H.u):

$$\begin{aligned} R_h \text{ Uniform} &\quad 0.11 \rightarrow 0.63 \quad (\times 5); \\ R_h \text{ Hubble} &\quad 0.34 \rightarrow 0.49 \quad (\times 1.4). \end{aligned}$$

Clearly the gentler collapse of the fragmented model has led to a more extended post-collapse configuration and reduced two-body evolution. Observe how the uniform model Ru20 is ejecting more stars than the Hubble model : if we repeat the calculation for the Hubble run Rh20 but now include only the bound stars, the curve of R_h obtained and shown as dash is shifted down but keeps essentially the same slope ≈ 0.004 . By contrast, the calculation for the bound stars of run Ru20 yields a much shallower slope than for the whole system: the slope drops from 0.015 to about 0.007. Irrespective of how the half-mass radius is calculated, the conclusion remains the same and agrees overall with the remark by Caputo, de Vries & Portegies Zwart (2014) that boosting the kinetic energy of the collapsing initial configuration softens the collapse ; this was shown in a different context by Theis & Spurzem (1999) and confirms these older findings. Here, the fragmented model has finite kinetic energy due to the clumps' internal motion. The important new feature brought by the fragmented initial conditions is that the *mass profile* of the virialised configuration evolves much less over time in comparison.

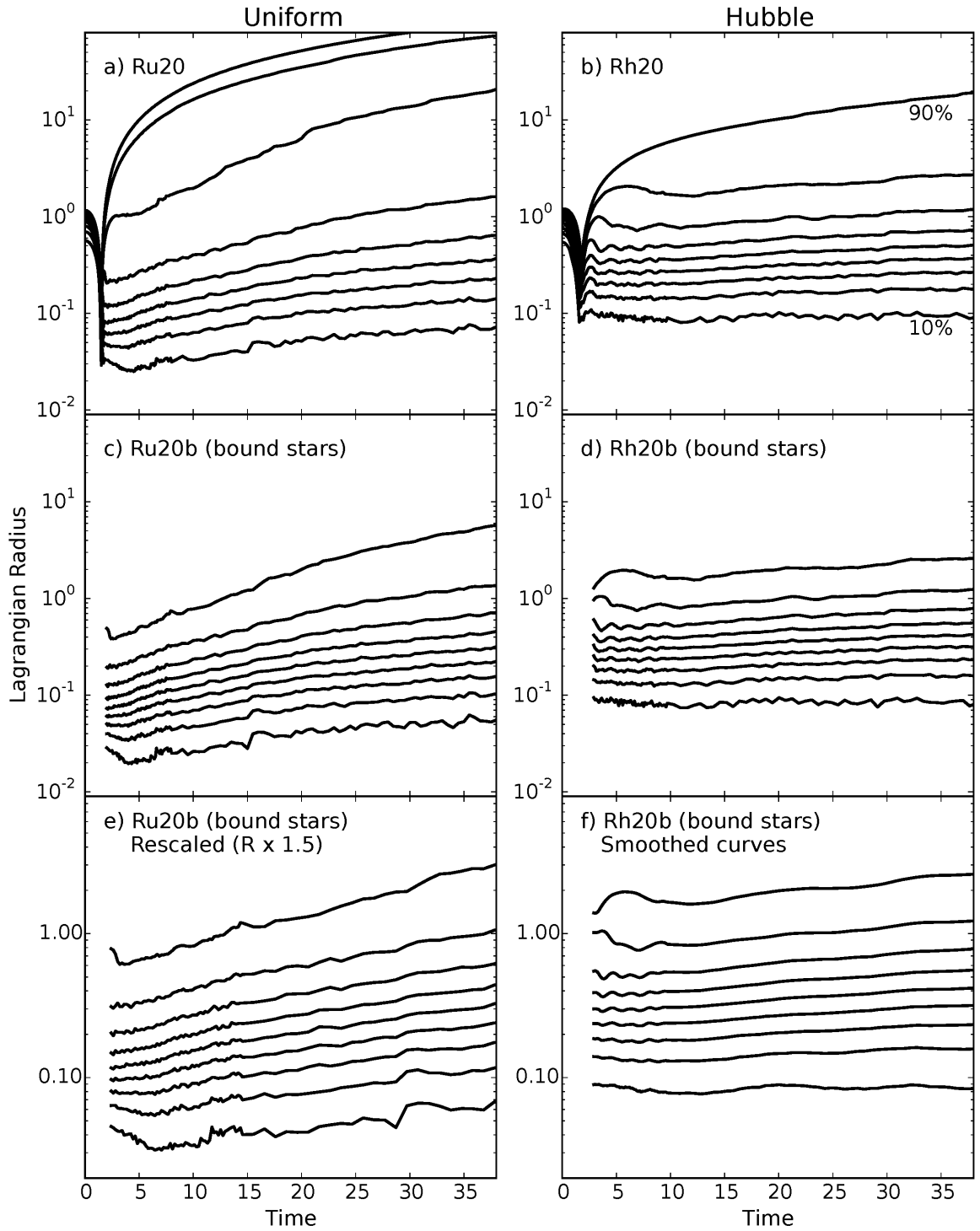


Figure 4.3: The ten-percentile mass radii (10% to 90%) as function of time. Radii and time axis are in H.u, with $t_{\text{H}\acute{\text{e}}\text{n}\text{o}n} = 1\text{unit} = 0.16\text{Myr}$. Left panels show the Uniform model and right panels show the Hubble fragmented models. Panels a and b show the evolution of the whole systems, while panels c and d shows the same radii computed for the bound stars only. Panel e shows the Uniform bound model (Ru20b) for which radius and time were rescaled to compensate the difference of initial kinetic energy (see text for details). Panel f shows the same information as panel d with smoothed data. 10% and 90% radii are labelled in the top right panel.

At the bounce, the half-mass radius of the Hubble model is ≈ 4 times larger than that of the initially uniform sphere at rest (Fig. 4.2). The half-mass radii overlap at time $t \approx 15 H.u.$ (solid curves) or $t \approx 50 H.u.$ (dashed curves). Is the same trend applicable to all Lagrangian radii? To answer this question we plot on Fig. 4.3 the ten-percentile mass radii for the two models. The results are displayed for the two situations including all the stars (top row) or bound stars only (middle row).

It is striking that the curves show very little evolution at all mass fractions for the case of the Hubble model (see right-hand panels on the figure), whereas all mass shells either contract or expand in time for the uniform one. We have noted how this model should undergo two-body relaxation on a timescale of $t \approx 270 H.u$ while the innermost 10% mass shell shows an indication of *core-collapse* at $t \simeq 5 H.u..$ This is due to the presence of a mass spectrum, the time-scale for core-collapse should be closer to the mass-segregation timescale, $t \simeq 14 H.u..$ The remaining difference can be attributed to the smaller total mass and the various assumptions made in section 4.1.2.

We note here that the two sets of curves reach very similar values at the end of the calculations ($t = 40 H.u.$). A key difference between the two models, therefore, is that the final configuration of the Hubble model is almost identical to what it was at the bounce ; the same simply does not hold in the case of a uniform-density collapse. Furthermore, the Hubble calculation shows no hint of two-body relaxation or core-collapse.

[Caputo, de Vries & Portegies Zwart \(2014\)](#) and [Theis & Spurzem \(1999\)](#) noted how a finite amount of kinetic energy in the *initial* configuration alters the depth of the bounce during collapse. The ratio of half-mass radius at the bounce, to its initial value, is then

$$\frac{R_h}{R_{h,0}} \simeq Q_0 + N^{-1/3} \quad (4.21)$$

where Q_0 is the virial ratio of the initial configuration (see [Caputo, de Vries & Portegies Zwart, 2014](#), Fig.5). We computed the kinetic energy of the Hubble configuration and found that the internal motion of the clumps means that $Q_0(\text{Hubble}) \simeq 0.02$ for a Salpeter mass function with upper truncation value of $20M_\odot$. With $N = 15k$ stars, the ratio $R_h/R_{h,0} \simeq 0.041$ when $Q_0 = 0$ shifts to $R_h/R_{h,0} \simeq 0.061$ when $Q_0 = 0.02$, or a factor close to $3/2$. To account for the difference in kinetic energy of the initial configurations, we may therefore rescale the uniform model such that positions are $\times 3/2$ and the time unit is $\times (3/2)^{3/2} \simeq 1.84$.

The new configuration would evolve in time in exactly the same way after mapping positions and time to their rescaled values. The result is shown as the bottom row on Fig. 4.3. Note that we have blown up the vertical axis to ease comparison between uniform and Hubble models with bound stars only included. The rescaled uniform model is now slightly more extended than before, but overall the final two configurations (at $t = 40 H.u.$) are as close as before rescaling. This demonstrates that the outcome of the uniform collapse and its comparison with the Hubble model is not sensitive to a small amount of initial kinetic energy. We note that while the ratio Q_0 is a free parameter in many setups for collapse calculations, that parameter is fixed internally in the Hubble approach.

4.3 Global mass segregation

To investigate the state of mass segregation in our models, we follow the analysis of [Caputo, de Vries & Portegies Zwart \(2014\)](#). The masses are sorted by decreasing values, then subdivided into ten equal-mass bins. This means that the first bin contains the most massive stars. The number of stars in each bin increases as we shift to the following bins, since their mean mass decreases, and so on until we have binned all the stars. The half-mass radius R_h computed for each bin is then plotted as function of time. In this way the mass segregation unfolds over time:

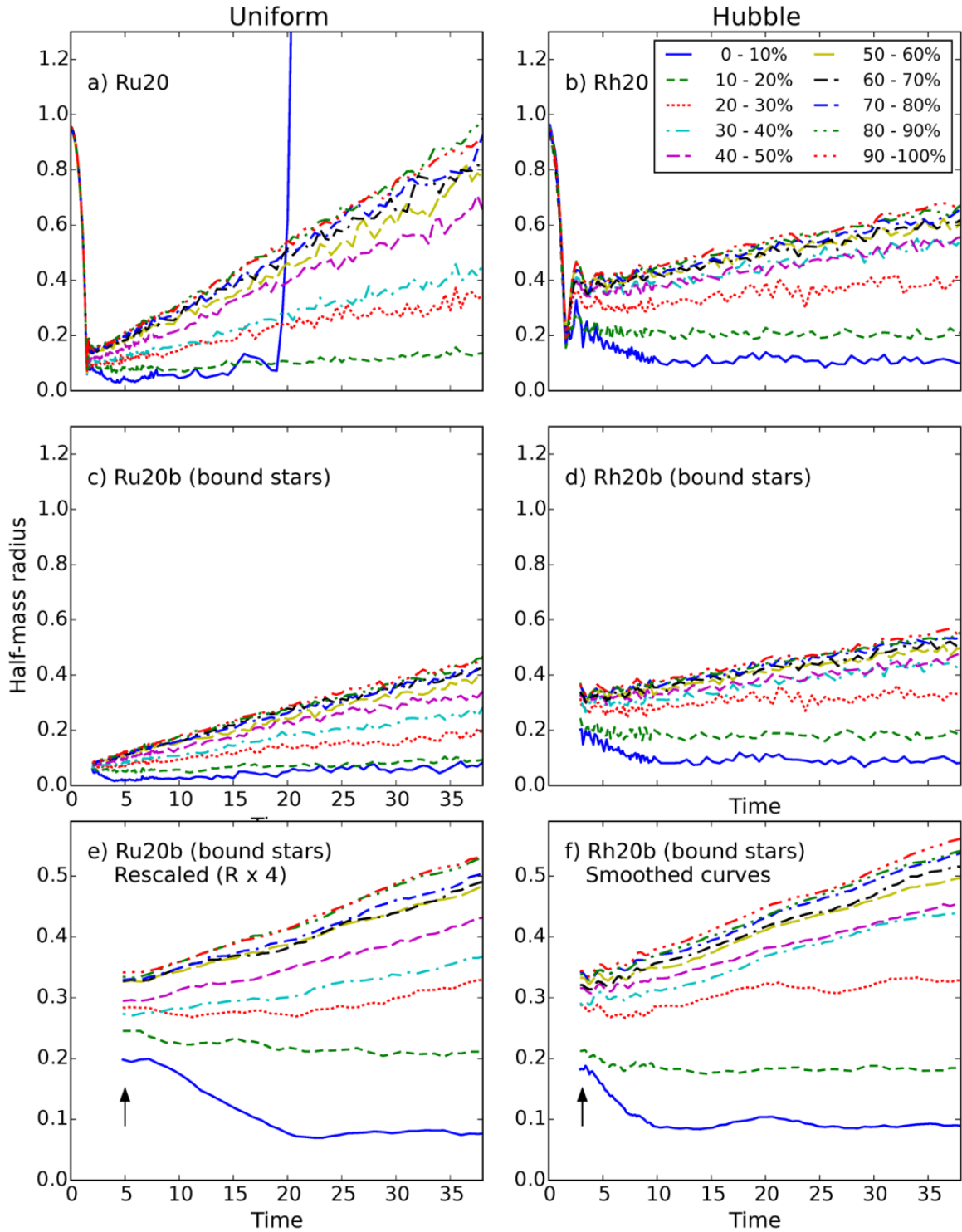


Figure 4.4: Half-mass radii of stars selected by mass as function of time. Each bin identified with 0-10%, 10-20% .. 90-100%, contains ten percent of the total system mass. The stars where sorted by mass in decreasing order, and used to fill each ten-percentile mass bin in order. Hence the first ten-percentile contains the most massive stars, the next ten-percentile the second group of massive stars, and so on until the 90-percentile bin which contains the least massive stars in the model and is the most populated. Half-mass radius and time are in H.u, with $t_{\text{Henon}} = 1 \text{ unit} = 0.16 \text{ Myr}$. Left panels show the evolution of the Uniform model (Ru20, Ru20b) and right panels do the same for the Hubble model (Rh20, Rh20b). The organization of panels follows the same layout than figure 4.3 with a different factor for the rescaling of the uniform system.

if the stars were not segregated by mass, all radii R_h would overlap. If two sub-populations share the same spatial distribution, their respective R_h will overlap.

Figure 4.4 graphs the results for initially uniform-density- and fragmented Hubble models. The layout of the figure is the same as for Fig. 4.3. The violent relaxation phase leads to mass loss for both models and the much more rapid expansion of the half-mass radii of low-mass stars is an indication that most escapers have a lower value of mass.

Fig. 4.4(c) and (d) graphs R_h for the bound stars of each sub-population. Clearly the initially uniform-density model is more compact early on, but note how the heavy stars sink rapidly to the centre, more so than for the case of the Hubble model. The spread of half-mass radii increases with time for both models, however two-body relaxation in the uniform-collapse calculation is much stronger, so that by the end of the simulations the half-mass radii of the low-mass stars of the respective models are essentially identical.

Since the low-mass stars carry the bulk of the mass, that means that the two models achieve the same or similar mean surface density by the end of the run. At that time, the heavy stars in the uniform-collapse calculation are clearly more concentrated than in the Hubble run (compare the radii out to $\sim 40\%$ most massive stars). A direct consequence of this is that the *color* gradients of the core region of a cluster are much reduced when the assembly history proceeds hierarchically, in comparison with the monolithic collapse. It will be interesting and possibly important in future to compare such models with actual data for young clusters.

Another interesting remark is that the kinematics of the stars within the *system* half-mass radius is much different between the two models. For the Hubble calculation, the system half-mass radius, ≈ 0.43 H.u., at $t = 40$ (cf. Fig. 4.4d) coincides with the half-mass radius of the $30 - 40\%$ bin stellar sub-population. All bins up to that range show little or no time-evolution, around the end of the run, which we interpret as efficient retention of these stars by the relaxed cluster. In the case of the uniform-collapse run, the system half-mass radius reaches ≈ 0.33 H.u., which is significantly larger than the radius for the $30 - 40\%$ stellar sub-population. For that model, only the bins $0 - 10\%$ and $10 - 20\%$ are flat, and all the others increase almost linearly with time. Thus a fair fraction of bright stars deep in the cluster show systematic *outward streaming* motion, along with low-mass ones. This brings up the possibility to measure this signature motion through relatively bright stars, originating well inside the cluster half-mass radius. Recall that only post-bounce bound stars were selected to compute R_h on Fig. 4.4(c) and (d); the expansion is therefore not driven by chance events (e.g., Fig. 4.4a), but rather through two-body relaxation. On the down side the bright tracers would be short-lived, and this may prove a strong constraint for observational detection.

Given the early dynamical evolution associated with substructured stellar clusters, some observed dense objects may yet be out of equilibrium (see §??). We wish to investigate the out-of-equilibrium state of our models just after the collapse. To ease the comparison between the two systems, the same rescaling procedure as for Fig ?? was applied to the uniform model, only this time the scaling was chosen so that the two clusters have comparable densities after the bounce. Lengths were multiplied by 4; the time-axis is then scaled up by a factor $(4)^{3/2} = 8$. The result can be seen in panel (e); panel (f) shows a smoothed and zoomed in Hubble model for comparison.

We compare the values of the different half-mass radii of the various population before the dynamical mass segregation sets in. This process is clearly visible as the drop of the half-mass radius of the most massive stars during the evolution. We are interested in the segregation which originates from the collapse and is present before this dynamical evolution. Table 4.3 sums up the values of the half-mass radii taken at $t \sim 5$ for both models, both corresponding to the same unevolved post-collapse state (see arrows on panels e and f on Fig 4.4). With on the order of ~ 100 stars per bin or more, one estimates roughly a ten-percent standard deviation from random sampling. To measure the *relative* segregation between populations, the table also lists the ratios of each half-mass radius to the one for the most massive stars.

Table 4.3: Values of half-mass radii and their ratio to that of the most massive stars. The mass categories are labelled X%-X+10%, with the percent symbol omitted for brevity. The results are for the rescaled bound uniform model (rescaled Ru20b) and the bound Hubble model (Rh20b), after the collapse, and before dynamical mass segregation sets in.

Uniform (%)	0-10	10-20	20-30	30-40	40-50	50-60	60-70	70-80	80-90	90-100
Radius	0.20	0.245	0.282	0.273	0.294	0.325	0.326	0.328	0.335	0.340
Ratio	1	1.23	1.41	1.37	1.47	1.63	1.63	1.64	1.68	1.70
Hubble (%)	0-10	10-20	20-30	30-40	40-50	50-60	60-70	70-80	80-90	90-100
Radius	0.18	0.21	0.286	0.293	0.316	0.321	0.333	0.338	0.342	0.344
Ratio	1	1.16	1.58	1.63	1.76	1.78	1.85	1.88	1.90	1.91

Both models appear mass segregated (since these ratios are significantly greater than unity). The Hubble model is more segregated, on the whole, albeit in a different way compared to the uniform model. The segregation in that one is more regular and spreads over more mass bins. In the Hubble model, the segregation is much enhanced for the first two mass bins. Such differences in the degree and nature of segregation can be explained by the clumps structure before the collapse. We showed in section 3.3.3 the clumps were mass segregated with the most massive members being preferentially located at their center. The low membership and mass of most clumps implies that segregation mostly affects the very top of the stellar mass function. This segregation, predominant among massive stars, is then found in the resulting centrally concentrated system, after the collapse, and visible on Fig. 4.4.

The inheritance of mass segregation was studied by [McMillan, Vesperini & Portegies Zwart \(2007\)](#) for the case of merging Plummer spheres. [Allison et al. \(2010\)](#) furthermore showed that mass segregation in the system as a whole is enhanced for more filamentary fractal initial condition (lower dimension, D ; see their Fig. 5). Here our results confirm this observation. Mass segregation is a sensitive function of the initial clumpiness of the system and has immediate bearing on the dynamics of the virialised configuration, since all massive stars are more concentrated in the core.

CHAPTER 5

Detecting and injecting binaries

In this chapter, we introduce a new algorithm to detect and record binary system in nbody simulations. With this tool, we analyse the spontaneous binary population arising in the Hubble-Lemaître systems and we describe a binary injection method to complete this population to match the observations.

5.1 A new binary detection algorithm

5.1.1 Density comparison

The study of binary populations in nbody simulations requires an algorithm to detect binary systems and compute their characteristics. The simplest approach is to compute all star-star energies and consider bound pairs as binaries. This records a lot of ephemeral interactions, as n-body dynamics cause transient bound systems. An additional criteria is needed to assess the stability and robustness of a pair as a binary.

We introduce a new algorithm based on the idea of a density threshold: binaries must be denser than their direct environment. Before describing the algorithm, we wish to emphasize the importance of neighbour searches in this kind of study. Be it to obtain bound pairs or to study said pair direct environment, the quick retrieval of neighbours is crucial to an effective algorithm.

The method described here relies on the KD-tree algorithm (Press et al., 2007). While brute-force neighbour searches scale as $\propto N$, as all stars in the system have to be checked as potential neighbours, a KD tree, once built, performs neighbour searches with algorithmic complexity $\propto \log(N)$. The tree is built by sorting particles along one dimension, splitting them at the median, then sorting each branch along another dimension, splitting them again, and so on, cycling over dimensions. A two-dimensionnal example is show on Fig 5.1.

First, binary candidates are identified as negative energy pairs. The semi-major axis of the system is derived from the star motions, then a "binary density" is computed, with a the binary's semi-major axis :

$$\rho_{binary} = \frac{m_1 + m_2}{4\pi a^3/3}. \quad (5.1)$$

This is then compared to the local neighbour density, defined as the cumulated mass of a fixed number N_{nb} of neighbours to the pair over the spherical volume reaching to the last neighbour.

$$\rho_{local} = \frac{\sum_{i=0}^{N_{nb}} m_i}{4\pi r_{N_{nb}}^3/3}. \quad (5.2)$$

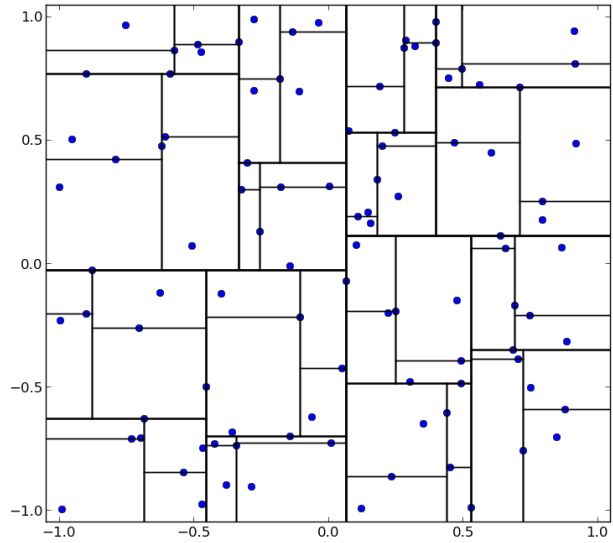


Figure 5.1: Illustration of a kd-tree for a random two-dimensional distribution (blue dots).

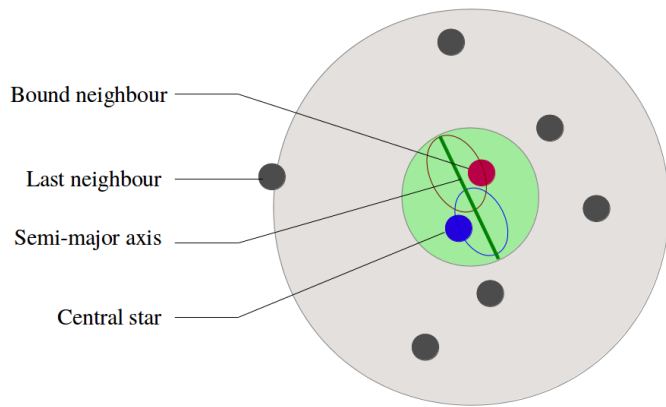


Figure 5.2: Illustration of the density threshold method. The central blue stars and the red bound neighbour describe a two-body orbit shown on the figure while the green bar indicates the major-axis of the system. This defines the binary density, green sphere, while the local density is defined with the grey stars, the other neighbours. Here, N_{nb} was set to 7.

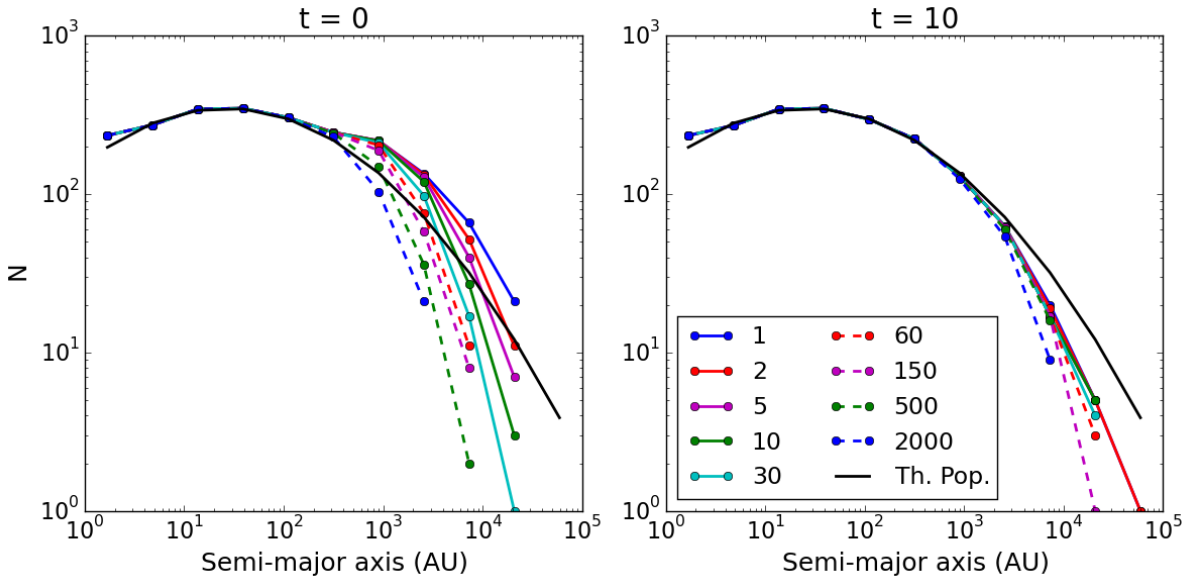


Figure 5.3: Semi-major axis histograms for various values of the density ratio D at $t=0$ and 10 H.u for a $10k$ star King model and a binary fraction $f_b = 0.3$. The injected log-normal population is shown as a black solid line.

If the density ratio exceeds a threshold D ,

$$\frac{\rho_{\text{binary}}}{\rho_{\text{local}}} > D, \quad (5.3)$$

the pair is registered as a binary. Other authors, eg [Parker et al. \(2009\)](#); [Lomax et al. \(2015\)](#), have used close hybrids of the criteria that we have implemented.

Stars can be found to be part of several binaries at once, which happens more often for massive stars as they clear more easily the density threshold. When that happens, the algorithm selects from such connected systems only the pairs exhibiting the lowest (most negative) binding energy.

This method has two free parameters: N_{nb} and D . N_{nb} can be set from 6 to 10 neighbours without a substantial impact on the detection. The density ratio is a more critical parameter, as if it is chosen too low, a lot of ephemeral binaries are found, while a high value picks only the closest binaries, ignoring wider, yet stable, systems.

5.1.2 Choosing a density ratio

We wish to find a good compromise value for the critical density ratio D that maximizes the number of detected stable binaries without collecting too much transient system. To do so, we explore the results brought by different values of D in a nbody system containing binaries.

We create a virialized King model with $N = 10000$ stars and a binary fraction of 0.3. This means there are 2300 binaries and 5400 single stars:

$$f_b = \frac{N_b}{N_s + N_b} = \frac{N_b}{N - N_b} \implies N_b = \frac{f_b}{1 + f_b} N = 2300. \quad (5.4)$$

The binaries follow the [Raghavan et al. \(2010\)](#) log-normal distribution introduced in 1.5.4. We let the system run for 10 H.u, or 12 crossing times, and write a snapshot every 0.1 H.u.

The binary detection is ran over all snapshots once per density ratio in the following list:

D	2000	500	150	60	30	10	5	2	1
---	------	-----	-----	----	----	----	---	---	---

We show on Fig 5.3 the semi-major axis distribution retrieved for various D for $t=0$ and $t=10$, with the theoretical injected population as a solid black line.

Looking at the left panel, for $t=0$, we see all density ratios return the same population for $a < 1000$ AU, while for higher separation, there are large variations. $D = 2000$ does not detect semi-major axis larger than 3000 AU, while $D = 1$ detects ~ 30 systems with $a > 10^4$ AU. After 12 crossing times, on right panels, we see the tight detected population didn't change, while all wide populations converged. The highest ratios did not undergo much change, while low ratios saw a large depletion of the population they initially returned.

We can say that a very high ratio only detect binaries that are guaranteed to resist the dynamical processing and survive, while low ratios detect more fragile systems. How ephemeral are these latter binaries ? To evaluate the different population detected by different ratios, we show on Fig 5.4 the detailed evolution of the wide, $a > 1000$ AU population. The large upper panel show all wide binaries evolution (time on y-axis) for $D = 2000$, arranged on the x-axis by time of first detection. Each pixel column represents a binary. The smaller sub panels show, for each density ratio, the history of the binaries this ratio detected that the previous, greater ratio did not. A binary that is detected with $D = 2000$ will also be detected for $D = 500$ and any other lower value. Fig 5.4 shows what kind of binaries lowering the ratio progressively brings to the detected population. The color codes the logarithm of the semi-major axis in AU, white means the binary is not detected.

The $D = 2000$ population is mainly made of stable, relatively tight binaries. About half the binaries are detected at $t=0$, while the others dynamically form in the system. Some are destroyed, other widened through interactions as their color bars transitions to a lighter color, sometimes after a "flickering" phase, when the detection goes on and off over successive snapshots. This is due to the binary entering a dynamical interaction with a third star or other binary, making the neighbour density undergoing spikes. This interaction leaves the binary with a weaker bound, thus higher binding energy.

Looking at the populations brought by lower ratios, we see they are progressively wider and more transient/flickering as the ratio lowers, which is to be expected. $D = 1$ only brings very ephemeral pairs, often not lasting more than a single snapshot. All ratios bring their share of transient binaries, but $D = 10$ is the last to capture relevant, relatively long-lived pairs.

Extreme values of density ratios bring a large difference in the detection of large binaries, but a moderate value like $D = 10$ appears the best compromise to capture the substance of a binary population.

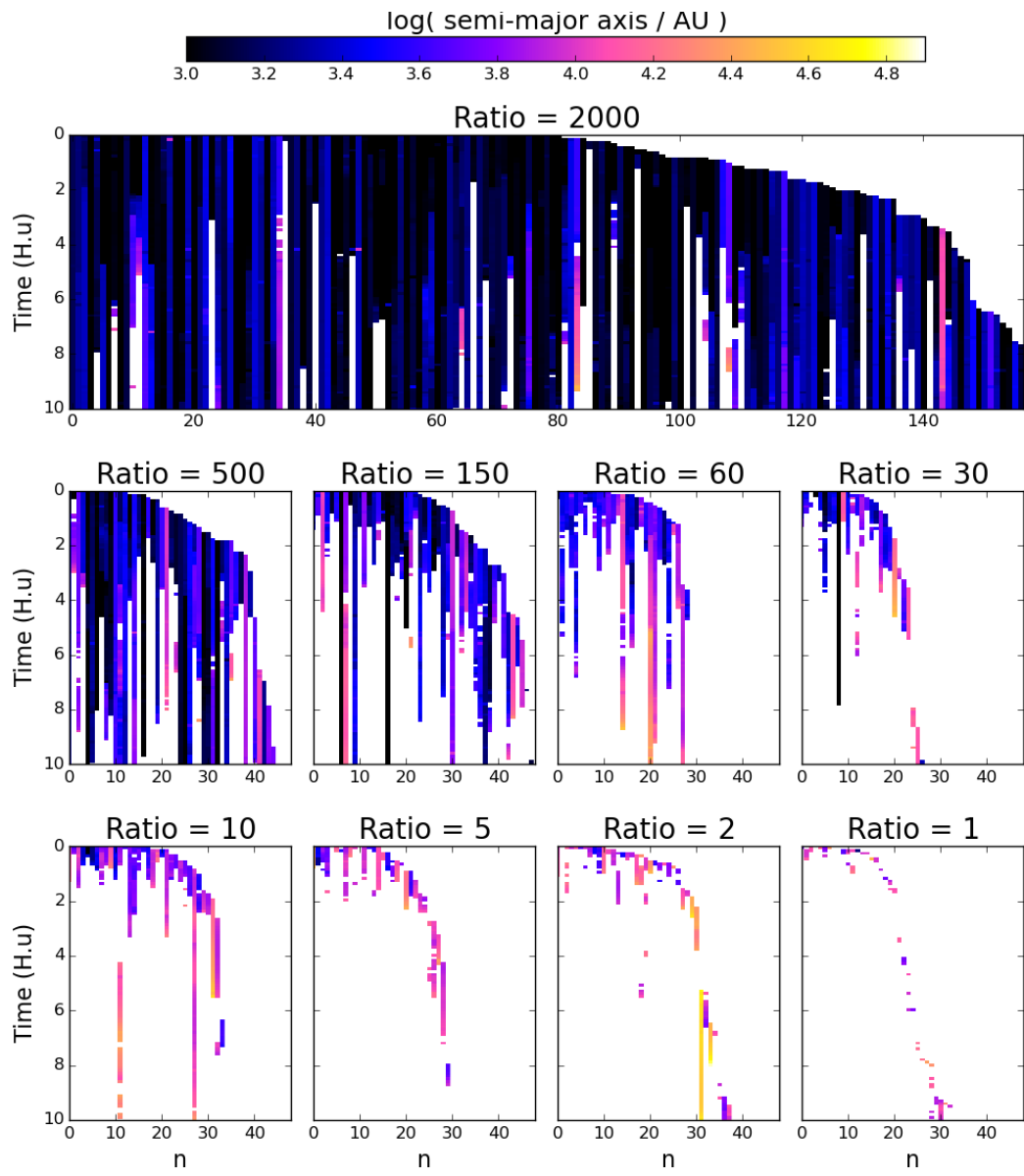


Figure 5.4: Visualization of the wide ($a > 1000$ AU) binary population in a King model over time. Large upper panel show the evolution of all binaries detected for a density ratio $D = 2000$, ordered by time of first detection. Each lower sub-panel show the new binaries detected with the new, lower, value of D compared to the previous one.

Bibliography

Bibliography

- Aarseth S. J., 1972, in BAAS, Vol. 4, Bulletin of the American Astronomical Society, p. 417
- Aarseth S. J., 2003, Gravitational N-Body Simulations. p. 430
- Aarseth S. J., 2012, MNRAS, 422, 841
- Aarseth S. J., Hénon M., Wielen R., 1974, A&A, 37, 183
- Aarseth S. J., Hoyle F., 1964, Astrophysica Norvegica, 9, 313
- Aarseth S. J., Lin D. N. C., Papaloizou J. C. B., 1988, ApJ, 324, 288
- Aarseth S. J., Zare K., 1974, Celestial Mechanics, 10, 185
- Adams F. C., 2000, ApJ, 542, 964
- Ahmad A., Cohen L., 1973, Journal of Computational Physics, 12, 389
- Allison R. J., Goodwin S. P., Parker R. J., de Grijs R., Portegies Zwart S. F., Kouwenhoven M. B. N., 2009a, ApJ, 700, L99
- Allison R. J., Goodwin S. P., Parker R. J., Portegies Zwart S. F., de Grijs R., 2010, MNRAS, 407, 1098
- Allison R. J., Goodwin S. P., Parker R. J., Portegies Zwart S. F., de Grijs R., Kouwenhoven M. B. N., 2009b, MNRAS, 395, 1449
- Andersen M., Zinnecker H., Moneti A., McCaughrean M. J., Brandl B., Brandner W., Meylan G., Hunter D., 2009, ApJ, 707, 1347
- Anderson J., Piotto G., King I. R., Bedin L. R., Guhathakurta P., 2009, ApJ, 697, L58
- André P. et al., 2010, A&A, 518, L102
- Bacon D., Sigurdsson S., Davies M. B., 1996, MNRAS, 281, 830
- Barker P., Dear P., Christianson J. R., Westman R. S., 2014, Metascience, 23, 203
- Barnes E. I., Lanzel P. A., Williams L. L. R., 2009, ApJ, 704, 372
- Barnes J., Hut P., 1986, Nature, 324, 446
- Barrow-Green J., 1997, Poincaré and the Three Body Problem, History of mathematics No. vol. 2. American Mathematical Society
- Bastian N., Covey K. R., Meyer M. R., 2010, ARA&A, 48, 339
- Bastian N., Goodwin S. P., 2006, MNRAS, 369, L9

-
- Bate M. R., 2009, MNRAS, 392, 590
- Bate M. R., 2012, MNRAS, 419, 3115
- Bate M. R., Bonnell I. A., Bromm V., 2003, MNRAS, 339, 577
- Bate M. R., Burkert A., 1997, MNRAS, 288, 1060
- Bate M. R., Tricco T. S., Price D. J., 2014, MNRAS, 437, 77
- Bédorf J., Portegies Zwart S., 2012, European Physical Journal Special Topics, 210, 201
- Belorizky D., 1930, Bulletin Astronomique, 6, 417
- Benhaiem D., Sylos Labini F., 2015, MNRAS, 448, 2634
- Binney J., Tremaine S., 2008, Galactic Dynamics (2nd ed.). Princeton Univ. Press, Princeton, NJ
- Boily C. M., Athanassoula E., Kroupa P., 2002, MNRAS, 332, 971
- Boily C. M., Kroupa P., 2003a, MNRAS, 338, 665
- Boily C. M., Kroupa P., 2003b, MNRAS, 338, 673
- Boily C. M., Nakasato N., Spurzem R., Tsuchiya T., 2004, ApJ, 614, 26
- Bonnell I. A., Bate M. R., Vine S. G., 2003, MNRAS, 343, 413
- Bonnell I. A., Smith R. J., Clark P. C., Bate M. R., 2011, MNRAS, 410, 2339
- Bonnell I. A., Vine S. G., Bate M. R., 2004, MNRAS, 349, 735
- Bressert E. et al., 2010, MNRAS, 409, L54
- Cambrésy L., 1999, A&A, 345, 965
- Caputo D. P., de Vries N., Portegies Zwart S., 2014, MNRAS, 445, 674
- Clagett M., 1959, The science of mechanics in the Middle Ages, University of Wisconsin publications in medieval science. University of Wisconsin Press
- Clarke C., 2012, in Astronomical Society of the Pacific Conference Series, Vol. 453, Advances in Computational Astrophysics: Methods, Tools, and Outcome, Capuzzo-Dolcetta R., Limongi M., Tornambè A., eds., p. 3
- Cohen I. B., Anne Whitman J. B., 1999, The Principia: Mathematical Principles of Natural Philosophy, 1st edn. University of California Press
- Cottaar M. et al., 2015, ApJ, 807, 27
- Czekaj M. A., Robin A. C., Figueras F., Luri X., Haywood M., 2014, A&A, 564, A102
- Dale J. E., Bonnell I., 2011, MNRAS, 414, 321
- Dale J. E., Ngoumou J., Ercolano B., Bonnell I. A., 2013, MNRAS, 436, 3430
- Davies B., Figer D. F., Kudritzki R.-P., Trombley C., Kouveliotou C., Wachter S., 2009, ApJ, 707, 844
- De Angelis A., Santo C. E., 2015, Journal of Astronomical History and Heritage, 18, 241

-
- de Wit W. J., Testi L., Palla F., Zinnecker H., 2005, A&A, 437, 247
- Dias W. S., Alessi B. S., Moitinho A., Lépine J. R. D., 2002, A&A, 389, 871
- Doppler C., 1842, ber das farbige Licht der Doppelsterne und einiger anderer Gestirne des Himmels. Verlag der Knigl. Bhm.
- D'Souza R., Rix H.-W., 2013, MNRAS, 429, 1887
- Duquennoy A., Mayor M., 1991, A&A, 248, 485
- Ebisuzaki T., Ito T., Makino J., Sugimoto D., 1990, Astronomical Herald, 83, 224
- Eddington A. S., 1916, MNRAS, 76, 572
- Ehlerova S., Palous J., Theis C., Hensler G., 1997, A&A, 328, 121
- Eisenstein D. J., Hut P., 1998, ApJ, 498, 137
- Elmegreen B. G., Falgarone E., 1996, ApJ, 471, 816
- Elsen E., Houston M., Vishal V., Darve E., Hanrahan P., V. P., 2006, "n-body simulation on gpus."
- Evans, II N. J. et al., 2009, ApJS, 181, 321
- Farias J. P., Smith R., Fellhauer M., Goodwin S., Candlish G. N., Blaña M., Dominguez R., 2015, MNRAS, 450, 2451
- Field G. B., Goldsmith D. W., Habing H. J., 1969, in BAAS, Vol. 1, Bulletin of the American Astronomical Society, p. 240
- Fischer D. A., Marcy G. W., 1992, ApJ, 396, 178
- Fleck J.-J., Boily C. M., Lançon A., Deiters S., 2006, MNRAS, 369, 1392
- Foster J. B. et al., 2015, ApJ, 799, 136
- Freeman K. C., Block D., Elmegreen B. G., Woolway M., 2015, Lessons from the local group : a conference in honour of David Block and Bruce Elmegreen. Springer
- Friedman J. L., Schutz B. F., 1978, ApJ, 221, 937
- Frisch U., Bec J., Villone B., 2001, Physica D Nonlinear Phenomena, 152, 620
- Fujii M. S., 2015, PASJ, 67, 59
- Fujii M. S., Portegies Zwart S., 2016, ApJ, 817, 4
- Galileo G., 1610, Sidereus nuncius. Thomas Baglioni
- Garcia M., Herrero A., Castro N., Corral L., Rosenberg A., 2010, A&A, 523, A23
- Geller A. M., de Grijs R., Li C., Hurley J. R., 2013, ApJ, 779, 30
- Goodwin S. P., Bastian N., 2006, MNRAS, 373, 752
- Goodwin S. P., Whitworth A. P., 2004, A&A, 413, 929
- Goodwin S. P., Whitworth A. P., Ward-Thompson D., 2004, A&A, 423, 169

-
- Gutermuth R. A., Megeath S. T., Myers P. C., Allen L. E., Pipher J. L., Fazio G. G., 2009, ApJS, 184, 18
- Gutermuth R. A., Pipher J. L., Megeath S. T., Myers P. C., Allen L. E., Allen T. S., 2011, ApJ, 739, 84
- Harris W. E., 1996, VizieR Online Data Catalog, 7195
- Hartmann L., 2002, ApJ, 578, 914
- Hayashi C., 1961, PASJ, 13
- Heggie D., Hut P., 2003, The Gravitational Million-Body Problem: A Multidisciplinary Approach to Star Cluster Dynamics
- Heggie D. C., Aarseth S. J., 1992, MNRAS, 257, 513
- Hillenbrand L. A., Hartmann L. W., 1998, ApJ, 492, 540
- Hills J. G., 1980, ApJ, 235, 986
- Holmberg E., 1941, ApJ, 94, 385
- Houghton H. E., 1942, Monthly Notes of the Astronomical Society of South Africa, 1, 107
- Hubber D. A., Whitworth A. P., 2005, A&A, 437, 113
- Hubble E., 1929, Contributions from the Mount Wilson Observatory, vol. 3, pp.23-28, 3, 23
- Ito T., Ebisuzaki T., Makino J., Sugimoto D., 1991, PASJ, 43, 547
- Jeans J. H., 1916, MNRAS, 76, 567
- Kandori R. et al., 2005, AJ, 130, 2166
- King I. R., 1981, QJRAS, 22, 227
- Kirk H., Myers P. C., 2011, ApJ, 727, 64
- Klessen R. S., Burkert A., 2000, ApJS, 128, 287
- Klessen R. S., Burkert A., 2001, ApJ, 549, 386
- Knigge C., Leigh N., Sills A., 2009, Nature, 457, 288
- Kouwenhoven M. B. N., Brown A. G. A., Portegies Zwart S. F., Kaper L., 2007, A&A, 474, 77
- Kouwenhoven M. B. N., Goodwin S. P., Parker R. J., Davies M. B., Malmberg D., Kroupa P., 2010, MNRAS, 404, 1835
- Kragh H., Smith R. W., 2003, History of Science, 41, 141
- Kramer E., 1982, The Nature and Growth of Modern Mathematics, Princeton paperbacks. Princeton University Press
- Krause M. G. H., Charbonnel C., Bastian N., Diehl R., 2016, A&A, 587, A53
- Kroupa P., Burkert A., 2001, ApJ, 555, 945
- Kruijssen J. M. D., Maschberger T., Moeckel N., Clarke C. J., Bastian N., Bonnell I. A., 2012, MNRAS, 419, 841

-
- Kuhn M. A., Feigelson E. D., Getman K. V., Sills A., Bate M. R., Borissova J., 2015, ApJ, 812, 131
- Kuhn M. A., Getman K. V., Feigelson E. D., 2015, ApJ, 802, 60
- Kustaanheimo P., Stiefel E., 1965, J. Reine Angew. Math, 218, 204
- Lada C. J., Lada E. A., 2003, ARA&A, 41, 57
- Lada C. J., Margulis M., Dearborn D., 1984, ApJ, 285, 141
- Larson R. B., 1969, MNRAS, 145, 271
- Lemaître G., 1927, Annales de la Société Scientifique de Bruxelles, 47, 49
- Lomax O., Whitworth A. P., Hubber D. A., Stamatellos D., Walch S., 2015, MNRAS, 447, 1550
- Mac Low M.-M., Klessen R. S., 2004, Reviews of Modern Physics, 76, 125
- Makino J., 1991, ApJ, 369, 200
- Marks M., Kroupa P., 2012, A&A, 543, A8
- Maschberger T., Clarke C. J., 2011, MNRAS, 416, 541
- Maschberger T., Clarke C. J., Bonnell I. A., Kroupa P., 2010, MNRAS, 404, 1061
- Maury J., 1992, Newton: Understanding the Cosmos, New horizons in history series. Thames and Hudson
- McKee C. F., Ostriker E. C., 2007, ARA&A, 45, 565
- McMillan S. L. W., Vesperini E., Portegies Zwart S. F., 2007, ApJ, 655, L45
- Merritt D., 2013, Dynamics and Evolution of Galactic Nuclei. Princeton Univ. Press, Princeton, NJ
- Meylan G., Heggie D. C., 1997, A&A Rev., 8, 1
- Mikkola S., Aarseth S. J., 1993, Celestial Mechanics and Dynamical Astronomy, 57, 439
- Miller G. E., Scalo J. M., 1979, ApJS, 41, 513
- Moeckel N., Bate M. R., 2010, MNRAS, 404, 721
- Moeckel N., Clarke C. J., 2011, MNRAS, 415, 1179
- Moeckel N., Holland C., Clarke C. J., Bonnell I. A., 2012, MNRAS, 425, 450
- Myers A. T., Klein R. I., Krumholz M. R., McKee C. F., 2014, MNRAS, 439, 3420
- Newton S. I., 1687, Philosophiae Naturalis Principia Mathematica, Vol. 1
- Nitadori K., Aarseth S. J., 2012, MNRAS, 424, 545
- Nyland L., Harris M., Prins J., 2004, "the rapid evaluation of potential fields using programmable graphics hardware."
- Offner S. S. R., Hansen C. E., Krumholz M. R., 2009, ApJ, 704, L124
- Olczak C., Spurzem R., Henning T., 2011, A&A, 532, A119

-
- Parker R. J., Goodwin S. P., Allison R. J., 2011, MNRAS, 418, 2565
- Parker R. J., Goodwin S. P., Kroupa P., Kouwenhoven M. B. N., 2009, MNRAS, 397, 1577
- Parker R. J., Meyer M. R., 2014, MNRAS, 442, 3722
- Parker R. J., Wright N. J., 2016, MNRAS, 457, 3430
- Pavese F., 2015, ArXiv e-prints
- Peebles P. J. E., 1980, The large-scale structure of the universe. Princeton Univ. Press, Princeton, NJ
- Pelupessy F. I., Portegies Zwart S., 2012, MNRAS, 420, 1503
- Poincaré H., 1906, Bulletin de la société astronomique de France, 20, 153
- Portegies Zwart S. F., Belleman R. G., Geldof P. M., 2007, New A, 12, 641
- Portegies Zwart S. F., McMillan S. L. W., Gieles M., 2010, ARA&A, 48, 431
- Press W. H., Teukolsky S. A., Vetterling W. T., Flannery B. P., 2007, Numerical Recipes 3rd Edition: The Art of Scientific Computing, 3rd edn. Cambridge University Press, New York, NY, USA
- Raghavan D. et al., 2010, ApJS, 190, 1
- Ramasubramanian K., 1998, Bulletin of the Astronomical Society of India, 26, 11
- Reipurth B., 2008, Handbook of Star Forming Regions
- Renaud F., Gieles M., Boily C. M., 2011, MNRAS, 418, 759
- Rubenstein E. P., Bailyn C. D., 1997, ApJ, 474, 701
- Rybicki J., Just A., 2015, MNRAS, 447, 3880
- Salpeter E. E., 1955, ApJ, 121, 161
- Scalo J., Vázquez-Semadeni E., Chappell D., Passot T., 1998, ApJ, 504, 835
- Schneider S., Elmegreen B. G., 1979, ApJS, 41, 87
- Skory S., Turk M. J., Norman M. L., Coil A. L., 2010, ApJS, 191, 43
- Springel V. et al., 2005, Nature, 435, 629
- Strömgren E., 1909, Astronomische Nachrichten, 182, 181
- Sundman K. F., 1912, Acta Mathematica, 36, 105
- Tailo M. et al., 2015, Nature, 523, 318
- Terlevich E., 1980, in IAU Symposium, Vol. 85, Star Clusters, Hesser J. E., ed., p. 165
- Teyssier R., 2002, A&A, 385, 337
- Theis C., Spurzem R., 1999, A&A, 341, 361
- Turner J. A., Chapman S. J., Bhattal A. S., Disney M. J., Pongracic H., Whitworth A. P., 1995, MNRAS, 277, 705

-
- Tutukov A. V., 1978, A&A, 70, 57
- van Albada T. S., 1968a, Bull. Astron. Inst. Netherlands, 20, 57
- van Albada T. S., 1968b, Bull. Astron. Inst. Netherlands, 20, 40
- van den Bergh S., 2011, JRASC, 105, 197
- von Hoerner S., 1960, ZAp, 50, 184
- von Hoerner S., 1963, ZAp, 57
- von Hoerner S., 2001, in Astronomical Society of the Pacific Conference Series, Vol. 228, Dynamics of Star Clusters and the Milky Way, Deiters S., Fuchs B., Just A., Spurzem R., Wielen R., eds., p. 11
- Wang L. et al., 2016, MNRAS, 458, 1450
- Weidner C., Kroupa P., Bonnell I. A. D., 2010, MNRAS, 401, 275
- Weidner C., Kroupa P., Pfleiderer-Altenburg J., 2013, MNRAS, 434, 84
- Whitmore B. C. et al., 2010, AJ, 140, 75
- Wright N. J., Parker R. J., Goodwin S. P., Drake J. J., 2014, MNRAS, 438, 639
- Wünsch R., Dale J. E., Palouš J., Whitworth A. P., 2010, MNRAS, 407, 1963
- Yoccoz J. C., 2010, La Lettre du Collège de France, 28, 38

List of Figures

1	(a): depiction of the Ptolemaic geocentric system, the equant is not shown. (b): Copernicus illustration of his own heliocentric system, from <i>De revolutionibus</i>	2
2	(a) and (b): drawings by the hand of Galileo of his astronomical observations.	3
3	(a) a supposedly descendant from Newton's apple tree in Cambridge. The drawing in (b) illustrates the common mechanics of cannonballs and satellites.	4
4	The observer and the theorist, a century apart.	6
5	The Siemens 2002, seen here on (a) at the computer museum in Kiel, could perform 2000 operations a second. The Hydra cluster, on (b), at the Max Planck Computing & Data Facility in Garching is made of 83,000 cores and 676 GPUs for a total of 10^{15} operations per seconds, a billion millions.	8
6	The evolution of the number of particles in N-body simulations. Solid line shows the Moore law. The figure was taken from Bédorf & Portegies Zwart (2012).	9
1.1	Examples of various types of cluster. White bars at the lower left of each pictures show 1 parsec length scale. The dust present in the young Pleiades open cluster scatters starlight, producing this blue haze. The globular cluster ω Centauri contains one million stars and is the largest known star cluster in the Milky Way. <i>Credits: NASA, ESA, AURA/Caltech; ESO/INAF-VST/OmegaCAM</i>	12
1.2	Examples of various types of cluster. White bars show 1pc. The young massive cluster R136 is surrounded by its primordial nebula while the embedded cluster NGC 1333 is still inside it. (b) is a composite of visible and infra-red light. <i>Credits: NASA, ESA, F. Paresce; T. Rector(U. Alaska Anchorage), H. Schweiker</i>	13
1.3	Radius-Mass Diagram for Milky Way clusters. Blue dots are open clusters, red dots Globular clusters and purple squares show Young Massive Clusters. Dashed lines show constant density within half-mass radius $\rho_h = 3M/8\pi r_{hm}^3$ and dotted lines show constant half-mass relaxation time. The plot was taken from the review Portegies Zwart, McMillan & Gieles (2010).	14
1.4	Comparison of King and Plummer models density as a function of radius, for similar core radiiuses.	17
1.5	Visible light and infrared view of a part of the Orion star forming complex. Horsehead nebula is visible on the right, as well as the very bright star Alnitak, part of the Orion belt. NGC 2071 and 2068 are visible on the left. Pink infrared coloring shows radiation from very bright young massive stars forming in the cloud. Colder filaments are visible all around. White bar on lower right of visible shows 1 parsec. <i>Credits: Digitized Sky Survey; ESA/Herschel/PACS</i>	19

1.6	Stages of stellar birth. (a) is just cold molecular gas and contains no central source yet. (b) is more advanced, though hidden in visible light, its central protostar shines in infrared. The protostar in (c) is actively accreting its disk and produces jets. (d) is a pre main-sequence star, free from its envelope and surrounded by primordial gas. (e) is the mature stellar stage: the main sequence. <i>Credits: Kandori et al. (2005); NASA/JPL-Caltech/Evans,N; Burrows,C/HST-NASA; ESA/Hubble & NASA; DSS</i>	20
1.7	(a): observational data from the Monoceros R2 star forming region. Protostars are shown as red points and gas density (traced through extinction) is shown in greyscale. The figure was extracted from Gutermuth et al. (2011). (b): hydrodynamical simulation of a star forming region yellow points are star-like sink particles and red levels show gas density. The figure was extracted from Bonnell et al. (2011).	21
1.8	(a): hydrodynamical simulation of wind-induced gas expulsion around a small cluster, the figure was extracted from Dale et al. (2013). (b) virial parameter of stellar clumps in a star forming hydrodynamical simulation, ignoring the potential of the gas to predict their post-expulsion fate. The solid line is the cumulated distribution of clumps over all snapshots; the shaded histogram shows the final distribution. The figure was extracted from Kruijssen et al. (2012).	21
1.9	Representation of four methods to generate substructures. (a) is extracted from Kruijssen et al. (2012), constructed with data from Bonnell, Bate & Vine (2003), (b) is extracted from Fujii (2015). (c) and (d) were generated for this work.	24
1.10	(a) Hubble observation of the binary star Albireo, fifth brightest star in the Cygnus constellation. Albireo A, the red star, is a close binary system itself (not represented on (b) for simplicity). The pair has a period of 213 years and a semi-major axis $a \simeq 66$ AU.	26
1.11	(a) shows the observed distribution of period and semi-major axis observed in the field. Different hatchings show different observation techniques: horizontal lines show unobserved companions detected by the proper-motion acceleration of components, positively sloped lines show spectroscopic binaries, negatively sloped lines visual binaries, cross hatching show objects found with both, and vertical lines are objects with common proper motions. (b) was compiled from several surveys, detailed in Fig 4.? (to come later). Both figures were extracted from Raghavan et al. (2010).	27
1.12	(a): total binary fraction over time in a subvirial fractal system. Corresponding models for the solid, dashed, dot-dashed and dotted are respectively 100% initial binary fraction with log-normal distribution, 100% fraction with Kroupa distribution, field-like fraction with log-normal distribution and field and 75% fraction with log-normal distribution. (b): 100% initial binary fraction with an initial log-normal distribution (open histogram) and the evolved distribution after 1Myr (hashed histogram). Solid red and dashed blue lines are fits for, respectively, the G-dwarf and M-dwarf populations. Both figures were extracted from Parker, Goodwin & Allison (2011).	29
1.13	Illustration of block time steps on 4 particles. Particles get their positions updated for each arrow symbol, common time steps are shown as vertical dotted lines. Figure from NB6++ User Manual.	31
1.14	Summary of the Hermite scheme starting from known positions and velocities at t_0 to obtain 5th order values at t .	33
2.1	Theoretical values of the apex time, at which the system stops expanding, as a function of initial HL parameter, which tunes the strength of the initial expansion.	40

2.2	Schematic illustration of a sinewave density perturbation (red line) applied to an uniform distribution of matter (blue dots) and the resulting distribution (red dots). The mode displayed here has $m = 10$ and its amplitude was exaggerated.	43
2.3	(a): growth of perturbation ξ_* over dimensionless time τ until the end of expansion at $\tau = 3.84$. An overdensity seeded with a wavelength λ_* begins its collisional evolution when ξ_* reaches $\frac{\lambda_*}{2}$. These regimes are illustrated for $\lambda_* = 0.04$ and $\lambda_* = 0.08$. The overdensities have to evolve collisionally for at least τ_{ms} to mass-segregate. This time-scale is also shown for each case. The blue case evolve collisionally for several τ_{ms} and will end up mass-segregated, while the red case visibly don't have have time to segregate. Modes of large wavelength tend to produce less mass-segregated clumps. (b) for a given number of nodes m , a model on the right of the corresponding line (arrow for $m = 10$) will have mass-segregated overdensities at the end of the expansion, will on the left, the collisional evolution is too short for segregation to sets in. The red crosses show the minimum N below which the modes cannot be resolved.	46
3.1	Progressive fragmentation through the Hubble expansion. The left panel shows the initial uniform sphere; the middle panel, an intermediate step, slightly fragmented with a slowed down expansion; the right panel is the final stage, when the expansion has stopped and the fragmentation is fully developed. N=10000 particles were used in this N-body model, with $H_0 = 1.0$. Time and coordinates are in Hénon units.	49
3.2	Illustration of a Minimum Spanning Tree and its use to isolate subgroups, using a cutting length d_{cut} .	50
3.3	Two different methods to identify the critical d_{cut} for clump detection. Both methods give the same value. For this 80k model, the value is 0.024 in Hénon units. The ref linear fit on (b) was made on the linear portion with sufficient data points, discarding the very few further points departing from the tendency.	51
3.4	Example of detected clumps for three cutting length, 0.014 (top panel), 0.024 (middle panel), 0.034 (bottom panel), which were labeled A,B,C in Fig. 3.3a. A cube within a 80k particles fragmented model was extracted and projected. Empty circles are stars which do not belong to any clump, black circles are clump members, and blue squares are stars that are identified as a single large clump. Tick marks are spaced by 0.05 length units for a box size of 0.35 units.	58
3.5	Mass function of the clumps identified with the MST algorithm. The calculations all had $N = 15000$ stars, and we have averaged over 30 realisations for each configuration. The results for three stellar mass functions are displayed : a model with equal-mass stars (green dashed line) ; a Salpeter distribution function truncated at $20M_\odot$ (solid red line, left) ; a Salpeter distribution function truncated at $100M_\odot$ (solid red line, right). (a) The clumps mass function for equal-mass models shows a trend with mass roughly in agreement with an M^{-3} power-law. By comparison, the results for an Salpeter stellar distribution function truncated at $20M_\odot$ has a bell-shaped profile, with a peak around $M = 20.5M_\odot$; only the tail-end shows marginal agreement with an $\propto M^{-2}$ power-law (dotted line on the figure) ; (b) another Salpeter distribution function but with the upper-mass truncation set at $100M_\odot$. The tail at large clump mass is now much flatter, with a slope $\approx M^{-1}$, (dotted line on the figure as well). The bins used had constant logarithmic mass intervals.	59
3.6	Clump mass function (real mass) for several H_0 and two memberships.	59

3.7	Clump mass function for several memberships and two H_0 . Masses in the top panels are in Hénon units, the x-axis was scaled with a factor 100 to get a percentage of the total mass of the system. Bottom panel masses are in physical units. In each panel, top sub-panel shows actual clump count in each bin (averaged over sampling), while bottom sub-panel normalize the count by the model membership.	60
3.8	Clump mass function (real mass) for several H_0 and two memberships.	61
3.9	(a) Distribution of the one-dimensional velocity field for the whole cluster as the thick solid black line, in the simulation labelled as R40h20 at the apex time ($H=0$). The red dashed distribution matches clump members and thin solid blue the field particles. (b) The distribution for three different values of H_0 : when $H_0 = 0$, the distribution is a Dirac- δ around $v = 0$. The central distribution broadens as H_0 increases to 0.3 and 1. Observe the exponential profiles at large $ v $. Velocities are in H.u	61
3.10	Top panel : Mass function of all stars belonging to a detected clump (solid red). The expectation drawn from a Salpeter distribution function for the same total number of stars in dotted black ; the grey shade are 1σ uncertainties. The green dashed line is the distribution for the full cluster. Bottom panel : same data normalised to the Salpeter expectation.	61
3.11	(a) Mass of the heavier star in each clump, shown as white dots, as a function of clump mass. The color map shows the likelihood for the maximum mass if all clump members were sampled from a Salpeter IMF ; the orange crest gives the maximum likelihood. The red dashed line shows the relation $m_{clump} = 2m_{max}$ (see. section 3.2.1). The data was taken from the R40h100 run. (b) is a similar distribution from Weidner, Kroupa & Pflamm-Altenburg (2013), built with data about young embedded star clusters from Weidner, Kroupa & Bonnell (2010). The black frame notes the range of masses displayed in (a).	62
3.12	Illustration of the radial ranking method. Stars marked 1,2 and 3 are the first, second and third most massive stars in the clump. Distances to the geometrical center are computed then sorted. The position in the sorted list is converted to a number, the radial rank.	62
3.13	Histograms of radial ranking of first, second and third most massive star in each clump for a model with $N = 40\,000$ stars (R40h100).	62
4.1	Distance to origin for 750 stars from run Ru20 (see Table 4.1). Red lines show the trajectory of stars that are considered ejected according to our criterion. . . .	66
4.2	Half-mass radius as function of time for two systems undergoing collapse : a uniform-density sphere (thin red solid curve) and a clumpy Hubble model (thick blue solid curve). Half-mass radii are in H.u, as well as the time axis, where $t_{\text{Hénon}} = 1\text{unit} = 0.270 \times 10^5$ years. Dashed lines are the half-mass radii of the same systems for the same systems but including only the bound stars.	66
4.3	The ten-percentile mass radii (10% to 90%) as function of time. Radii and time axis are in H.u, with $t_{\text{Hénon}} = 1\text{unit} = 0.16\text{Myr}$. Left panels show the Uniform model and right panels show the Hubble fragmented models. Panels a and b show the evolution of the whole systems, while panels c and d shows the same radii computed for the bound stars only. Panel e shows the Uniform bound model (Ru20b) for which radius and time were rescaled to compensate the difference of initial kinetic energy (see text for details). Panel f shows the same information as panel d with smoothed data. 10% and 90% radii are labelled in the top right panel.	67

4.4	Half-mass radii of stars selected by mass as function of time. Each bin identified with 0-10%, 10-20% .. 90-100%, contains ten percent of the total system mass. The stars where sorted by mass in decreasing order, and used to fill each ten-percent mass bin in order. Hence the first ten-percentile contains the most massive stars, the next ten-percentile the second group of massive stars, and so on until the 90-percent bin which contains the least massive stars in the model and is the most populated. Half-mass radius and time are in H.u, with $t_{\text{Henon}} = 1 \text{ unit} = 0.16 \text{ Myr}$. Left panels show the evolution of the Uniform model (Ru20, Ru20b) and right panels do the same for the Hubble model (Rh20, Rh20b). The organization of panels follows the same layout than figure 4.3 with a different factor for the rescaling of the uniform system.	68
5.1	Illustration of a kd-tree for a random two-dimensional distribution (blue dots).	71
5.2	Illustration of the density threshold method. The central blue stars and the red bound neighbour describe a two-body orbit shown on the figure while the green bar indicates the major-axis of the system. This defines the binary density, green sphere, while the local density is defined with the grey stars, the other neighbours. Here, N_{nb} was set to 7.	72
5.3	Semi-major axis histograms for various value of the density ratio D at $t=0$ and 10 H.u for a 10k star King model and a binary fraction $f_b = 0.3$. The injected log-normal population is shown as a black solid line.	72
5.4	Visualization of the wide ($a > 1000 \text{ AU}$) binary population in a King model over time. Large upper panel show the evolution of all binaries detected for a density ratio $D = 2000$, ordered by time of first detection. Each lower sub-panel show the new binaries detected with the new, lower, value of D compared to the previous one.	73

List of Tables

2.1	Summary of main variables.	41
3.1	Summary of fragmentation models and their characteristics. These simulations started from an uniform sphere and were stopped when the expansion halted, at $t=3$ H.u . The third column shows the number of independent computations for each model.	51
4.1	Summary of collapse simulations and their characteristics. These simulations started from a subvirial state: cold uniform sphere or fully fragmented Hubble model; each were evolved up to $t = 40$ H.u	63
4.2	Number of initially ejected stars in two collapse calculations	66
4.3	Values of half-mass radii and their ratio to that of the most massive stars. The mass categories are labelled X%-X+10%, with the percent symbol ommitted for brevity. The results are for the rescaled bound uniform model (rescaled Ru20b) and the bound Hubble model (Rh20b), after the collapse, and before dynamical mass segregation sets in.	69